**University of Liège**

Aerospace and Mechanical Engineering Department Spatial Instrumentation and Experimentation

Centre Spatial de Liège

# Conception and Design of New Space Instrumentation for the Study of Massive Stars in the UV

*Advisor*
Prof. Pierre Rochus

*co-Advisor*
Prof. Gregor Rauw

Thesis submitted in fulfilment of the requirements for the degree of Doctor in Engineering Sciences

by

**Richard Desselle, Ir.**

Liège, year 2018

**Author's contact details**

Richard DESSELLE

Centre Spatial de Liège
University of Liège

Liège Science Park
Avenue du Pré-Aily
4031 Angleur, Belgium

e-mail: rdesselle@ulg.ac.be
phone: +32 43 82 46 67

**Members of the Examination Committee**

Prof. Gaëtan KERSCHEN (President of the Committee)
University of Liège (Liège, Belgium)
email: G.Kerschen@uliege.be

Prof. Pierre ROCHUS (Advisor)
University of Liège - Centre Spatial de Liège (Liège, Belgium)
e-mail: prochus@uliege.be

Prof. Gregor RAUW (Co-advisor)
University of Liège (Liège, Belgium)
e-mail: G.Rauw@uliege.be

Dr. Coralie NEINER
Observatoire de Paris (Paris, France)
e-mail: Coralie.Neiner@obspm.fr

Prof. Stefanos FASOULAS
University of Stuttgart (Stuttgart, Germany)
e-mail: fasoulas@irs.uni-stuttgart.de

Dr. Pierre ROYER
KU Leuven (Leuven, Belgium)
e-mail: pierre@ster.kuleuven.be

Prof. Yaël NAZE
University of Liège (Liège, Belgium)
e-mail: ynaze@uliege.be

# Abstract

In astrophysics, the UV domain is rich in important information that can be exploited by a multitude of groups of scientists, working on a variety of subjects. Because of the Earth's atmosphere, it is not possible to observe this spectral domain from the ground and therefore space observatories are needed to provide the scientific data. Motivated by the study of the properties of massive stars in the UV, this thesis is devoted to the design of new space instrumentation dedicated to this scientific purpose.

In the first part, the conception of an in-flight calibration unit is investigated to answer the needs of a large instrument proposed to ESA calls for medium-sized missions. The technologies available are identified and presented before being accommodated to the current instrument.

The second part is dedicated to UV instrumentation on-board very small satellites that are based on the Cubesat standard. After presenting the standard and previous Cubesat missions, feasibility studies of two instruments are conducted. The first instrument is a near-UV telescope designed to be integrated in a 3U Cubesat. The optical design, the entire satellite and a mission analysis are discussed. Based on all the previous points, a photometric budget is carried out to demonstrate the efficiency of the system. The second instrument is a near-UV low-resolution spectropolarimeter which is presented as a potential technology demonstrator in relation with the above-described medium-sized mission.

Conclusions and perspectives are presented and discussed in the third part of this thesis.

**Keywords**: Space, System engineering, Telescope, Calibration, Cubesat

# Acknowledgments

Before all else, I would like to express my sincere gratitude to my advisor and co-advisor Prof. Pierre Rochus and Prof. Gregor Rauw for their guidance throughout this thesis. Especially, I thank Prof. Gregor Rauw for his advice, his time and his inputs without which I could not go through the end.

Besides my advisors, I would like to thank the rest of my thesis committee, Prof. Yaël Nazé, Prof. Serge Habraken and Yvan Stockman who provided regular feedback about my work.

I am also pleased to acknowledge Prof. Gaëtan Kerschen from the University of Liège, Dr. Coralie Neiner from the Observatoire de Paris, Prof. Stefanos Fasoulas from the University of Stuttgart and Dr. Pierre Royer from the KU Leuven for accepting to participate in the examination committee of this thesis.

For the friendly working atmosphere, I wish to thank all my friends and colleagues from the Centre Spatial de Liège (CSL). In particular, I would like to thank Christian Kintziger who was also involved in the Action de Recherche Concertée (ARC) and with whom I had the chance to work during these fours years. I wish also to thank Jérôme Jacobs with whom I shared an office since my arrival at the CSL and with whom I had so many interesting discussions. I wish also to thank Etienne Renotte who was involved in the preparation of Arago and who has spent so many missions with me in Paris.

This research was funded through an ARC grant for Concerted Research Actions, financed by the French Community of Belgium (Wallonia-Brussels Federation).

Last but not least, I would like to thank my family and friends for their continuous support and encouragements. Especially, all of this would not have been possible without the support and the love of my wife Justine.

# Contents

**Contents** **11**

**List of Acronyms** **16**

**Introduction** **19**
Context . . . . . 19
Subjects Overview . . . . . 20

**I Preparation of an On-board Calibration Unit Concept for a Major Space Mission** **22**

**1 On-board Calibration Principles** **23**
1.1 Calibration of Scientific Space Instruments . . . . . 23
1.1.1 Principles . . . . . 23
1.1.2 CSL Heritage . . . . . 24
1.1.2.1 OLCI . . . . . 24
1.1.2.2 UVN . . . . . 26
1.2 Calibration Elements . . . . . 27
1.2.1 Celestial Standards . . . . . 27
1.2.2 White Light Sources . . . . . 28
1.2.3 Hollow Cathode Lamps . . . . . 30

**2 Application to the Arago Mission for the M4 and M5 Calls from ESA** **31**
2.1 Mission Presentation . . . . . 31
2.1.1 Scientific Objectives . . . . . 31
2.1.2 UV and Visible Spectropolarimetry . . . . . 32
2.1.3 Circular and Linear Spectropolarimetry . . . . . 32
2.1.4 Instrument . . . . . 32
2.2 Perimeter of Belgian Activities . . . . . 33
2.3 Calibration Requirements . . . . . 33
2.3.1 Offset . . . . . 33
2.3.2 Dark . . . . . 34
2.3.3 Flat Field . . . . . 34
2.3.3.1 Pixel Response Non Uniformity . . . . . 34
2.3.3.2 Blaze Function and Cross-order Profiles . . . . . 34

2.3.3.3 Linearity . . . 34
2.3.4 Relative Spectral Response Function . . . 35
2.3.5 Wavelength Calibration . . . 35
2.3.6 Calibration of Polarization . . . 35
2.3.7 Intra-pixel Response Non Uniformity . . . 36
2.4 Calibration Unit Preliminary Design . . . 37
2.4.1 Block Diagram . . . 37
2.4.2 Calibration Light Sources . . . 37
2.4.2.1 Flat Field Sources . . . 37
2.4.2.2 Wavelength Calibration Source . . . 39
2.4.3 Mechanical Parts . . . 40
2.4.3.1 Calibration Unit Box . . . 40
2.4.3.2 Injection Point Box . . . 42
2.4.4 Power Supply Considerations . . . 43

**II Very Small Missions Feasibility Studies 45**

**3 Cubesats Missions 46**
3.1 Cubesat Standard . . . 46
3.1.1 Overview . . . 46
3.1.2 Interests for Cubesats . . . 47
3.2 Cubesats in Astronomy and Astrophysics . . . 48
3.2.1 BRITE . . . 48
3.2.2 CXBN-2 . . . 50
3.2.2.1 ASTERIA . . . 51
3.2.3 PicSaT . . . 53
3.2.3.1 HaloSat: a mission under development . . . 54
3.2.4 Perspectives . . . 54

**4 Feasibility Study of a UV Photometer On-board a 3U Cubesat 55**
4.1 Proposed Instrument and Mission . . . 55
4.2 Optical Design . . . 57
4.2.1 Basic Considerations and Constraints . . . 57
4.2.1.1 Volume Constraints . . . 57
4.2.1.2 Field of View . . . 57
4.2.1.3 Effective Focal Length . . . 59
4.2.1.4 Number of Pixels and Focal Plane Size . . . 60
4.2.1.5 Filter . . . 61
4.2.1.6 Conic Constants and Radii . . . 61
4.2.2 Design Characteristics . . . 62
4.2.2.1 Geometry . . . 62
4.2.2.2 Spot Diagram . . . 63
4.2.2.3 Modulation Transfer Function (MTF) . . . 66
4.2.2.4 Baffling System . . . 69
4.2.2.5 Stray Light Analysis . . . 72
4.3 System Overview . . . 76

4.3.1 Solar Panels Configuration . . . 76
4.3.1.1 Table Configuration . . . 76
4.3.1.2 Cross Configuration . . . 77
4.3.1.3 Sky Visibility . . . 78
4.3.1.4 Comparison of the Configurations . . . 81
4.3.2 Detector Choice and Characteristics . . . 82
4.3.2.1 Back-Thinned CCD . . . 82
4.3.2.2 CMOS . . . 83
4.3.2.3 Microchannel Plates (MCP) . . . 84
4.3.2.4 Conclusion . . . 86
4.3.3 Data Storage and Transfer . . . 87
4.3.4 Attitude Considerations . . . 89
4.3.4.1 Pointing . . . 89
4.3.4.2 Jitter Noise . . . 90
4.4 Thermal Environment and Analysis . . . 92
4.4.1 Orbit Definition . . . 92
4.4.1.1 Launch Constraints . . . 92
4.4.1.2 Orbit Propagation . . . 93
4.4.2 Thermal Considerations . . . 95
4.4.2.1 External Thermal Loads . . . 95
4.4.2.2 Internal Thermal Loads: Power Budget . . . 96
4.4.2.3 Thermal Model . . . 100
4.4.2.4 Results for the Worst Thermal Cases . . . 101
4.5 Photometric Budget . . . 106
4.5.1 Basic Equations . . . 106
4.5.2 Modelling . . . 108
4.5.3 Interstellar Absorption $A_V$ . . . 109
4.5.4 Observation Strategy . . . 110
4.5.4.1 Total Efficiency of the Telescope . . . 110
4.5.4.2 Signal to Noise Ratio (SNR) . . . 111
4.5.4.3 Saturation Issues . . . 114

**5 Feasibility Study of a Low-Resolution UV Spectropolarimeter on-board a Cubesat 117**
5.1 Proposed Instrument and Mission . . . 117
5.2 Optical Design . . . 119
5.2.1 Polarimeter . . . 119
5.2.1.1 Fundamentals . . . 119
5.2.1.2 Polarimeter Design . . . 120
5.2.1.3 Mueller Matrix Calculation . . . 121
5.2.1.4 Material Selection . . . 122
5.2.1.5 Simulations . . . 123
5.2.2 Telescope . . . 126
5.2.3 Spectrometer . . . 126
5.3 Achievable Performances . . . 127
5.3.1 Field of View . . . 127

5.3.2 Signal to Noise Ratio . . . 128
5.4 Proposed Cubesat Platform . . . 131

**III Conclusions and Perspectives 133**

**6 Conclusions and Perspectives 134**
6.1 PART I: Preparation of an On-board Calibration Unit Concept for a Major Space Mission . . . 134
6.1.1 On-board Calibration Principles . . . 134
6.1.2 Application to the Arago Mission for the M4 and M5 Calls from ESA . . . 134
6.2 PART II: Very Small Missions Feasibility Studies . . . 135
6.2.1 Cubesats Missions . . . 135
6.2.2 Feasibility Study of a UV Photometer On-board a 3U Cubesat 135
6.2.3 Feasibility Study of a Low-Resolution UV Spectropolarimeter on-board a Cubesat . . . 137
6.3 General Conclusion . . . 138

**Bibliography 139**

**Appendices 147**

**A Polarimetry Basic Principles 148**
A.1 Stokes Parameters . . . 148
A.2 Mueller Matrices . . . 149
A.3 Jones Matrices . . . 150

**B Orbital Considerations 151**
B.1 Orbital Parameters . . . 151
B.2 $\beta$ Angle and Eclipse Duration . . . 152
B.3 Sun-Synchronous Orbit . . . 155

**C Published Article 157**

# List of Acronyms

| | |
|---|---|
| **AC** | Alternative Current |
| **ACS** | Advanced Camera for Surveys |
| **ADCS** | Attitude Determination and Control System |
| **ARC** | Action de Recherche Concertée |
| **ASTA** | Astrophysique Stellaire Théorique et Astérosismologie |
| **ASTERIA** | Arcsecond Space Telescope Enabling Research in Astrophysics |
| **BOL** | Beginning Of Life |
| **BRITE** | BRIght Target Explorer |
| **CAD** | Computer-Aided Design |
| **CCD** | Charge Coupled Device |
| **CMOS** | Complementary Metal Oxide Semi-conductor |
| **CoG** | Center of Gravity |
| **COS** | Cosmic Origins Spectrograph |
| **COTS** | Component Off-The-Shelf |
| **CSL** | Centre Spatial de Liège |
| **CXBN** | Cosmic X-ray Background Nanosatellite |
| **CZT** | Cadmium Zinc Telluride |
| **ECI** | Earth-Centered Inertial |
| **EGSE** | Electrical Ground Support Equipment |
| **EIT** | Extreme ultraviolet Imaging Telescope |
| **EM** | Electromagnetic |
| **EOL** | End Of Life |
| **ESA** | European Space Agency |
| **FEM** | Finite Element Model |
| **FOC** | Faint Object Camera |
| **FoV** | Field of View |
| **FF** | Flat Field |
| **FUSE** | Far Ultraviolet Spectroscopic Explorer |
| **GAPHE** | Groupe d'Astrophysique des Hautes Energies |
| **GMM** | Geometrical Mathematical Model |
| **HCL** | Hollow Cathode Lamp |
| **HST** | Hubble Space Telescope |
| **IMCCE** | Institut de Mécanique Céleste et de Calcul des Ephémérides |

| | |
|---|---|
| **IPRNU** | Intra-Pixel Response Non Uniformity |
| **IR** | Infrared |
| **IUE** | International Ultraviolet Explorer |
| **ISS** | International Space Station |
| **JPL** | Jet Propulsion Laboratory |
| **KUL** | Katholieke Universiteit Leuven |
| **LEO** | Low Earth Orbit |
| **LESIA** | Laboratoire d'études spatiales et d'instrumentation en astrophysique |
| **LoS** | Line-of-Sight |
| **LWA** | Lamp Wheel Assembly |
| **LUVOIR** | Large UV/Optical/Infrared Surveyor |
| **MCP** | Microchannel Plate |
| **MTF** | Modulation Transfer Function |
| **NIR** | Near-Infrared |
| **NASA** | National Aeronautics and Space Administration |
| **OBC** | On-Board Computer |
| **OLCI** | Ocean and Land Colour Instrument |
| **P-POD** | Poly Picosatellite Orbital Deployer |
| **PCB** | Printed Circuit Board |
| **PRNU** | Pixel Response Non Uniformity |
| **PSF** | Point Spread Function |
| **QE** | Quantum Efficiency |
| **QTH** | Quartz Tungsten Halogen |
| **RAAN** | Right Ascension of the Ascending Node |
| **RMS** | Root Mean Square |
| **RSRF** | Relative Spectral Response Function |
| **SED** | Spectral Energy Distribution |
| **SL** | Stray Light |
| **SNR** | Signal to Noise Ratio |
| **SSO** | Sun-Synchronous Orbit (SSO) |
| **STK** | Satellite Tool Kit |
| **SWIR** | Short-Wave Infrared |
| **TMM** | Thermal Mathematical Model |
| **TRL** | Technology Readiness Level |
| **UTC** | Universal Time Coordinated |
| **UV** | Ultraviolet |
| **UVN** | Ultraviolet Visible Near-infrared |
| **WLS** | White Light Source |
| **WP** | Work-Package |
| **WR** | Wolf-Rayet |

# Introduction

## Context

### Genesis of the Project

The project associated to this PhD thesis is part of an *Action de Recherche Concertée* (ARC) which is dedicated to the study of **Massive Stars**. This ARC brings together the following research entities from the University of Liège: the *Groupe d'Astrophysique des Hautes Energies* (GAPHE), the *Astrophysique Stellaire Théorique et Astérosismologie* (ASTA) team and the *Centre Spatial de Liège* (CSL).

The main aspects of space research treated within this ARC are: the fundamental understanding of massive stars which is the main concern of the GAPHE and ASTA teams and the instrumental design for observing these stars (under the responsibility of the CSL). The association of all these entities is fully complementary in order to carry out the overall ARC project.

### Study of Massive Stars in the UV

Massive stars are very hot and luminous stars which have a tremendous impact on their surroundings via their powerful stellar winds and huge UV luminosities. The combination of these winds, the strong ionizing radiation fields as well as the death of these stars in gigantic supernova explosions make massive stars major players for the evolution of the Universe.

The ARC is divided in seven work-packages (WP), four of them corresponding to PhD theses dedicated to specific aspects of the study of massive stars. The four topics covered by PhD theses are listed below. The WP concerned by the present manuscript corresponds to the #4.

- **WP #1**: Study of chemical abundances of fast rotating OB stars;
- **WP #2**: Study of fundamental parameters of massive stars in binaries;
- **WP #3**: Development of a near-IR spectrometer;

- **WP #4**: Development of new space instrumentation in the ultraviolet (UV).

Since the termination of the International Ultraviolet Explorer (IUE) mission in 1996 and the end of the Far Ultraviolet Spectroscopic Explorer (FUSE) in 2007, the UV domain suffers from a lack of dedicated instrumentation. The Hubble Space Telescope nevertheless allows to observe in the UV thanks to the STIS and COS spectrographs, but they share the available observing time with other instruments working in the visible and near-IR domain. Looking towards the next few years, whilst several IR space observatories are under construction or in the planning (JWST [1] or SPICA [2] for examples), there is currently no mid- to far-UV mission at a similar level of preparation. Yet, the UV domain has a large diagnostic power, especially for the study of bright massive stars as they have their spectral energy distribution peaking in the UV.

In this WP, it is proposed to investigate two aspects of space missions. First, the working groups are involved in the Arago consortium, aiming at proposing a spaceborne UV/Optical spectropolarimeter in response to the ESA calls for medium-sized missions. Second, it is proposed to conduct feasibility studies of Cubesats with small UV telescopes and associated instruments.

# Subjects Overview

## Preparation of an On-board Calibration Unit Concept for a Major Space Mission

In order to fully understand observed signals and translate them into scientific data, an accurate knowledge of the observing instrument is required. The calibration of the instrument is thus an important part of the design process of a mission [3].

The methods for the calibration of on-board space telescopes are divided into three categories [3]:

i. Pre-flight calibration which is performed at system or sub-systems levels in the laboratory;

ii. Calibration in orbit using celestial standards;

iii. Calibration by use of a *transfer standard* that is carried into and operated in orbit as part of the scientific payload.

In the context of the preparation of the Arago mission, all these aspects have to be considered and more specifically the third one because it is the most complex. Indeed, the proposed instrument is a high-resolution spectropolarimeter working both in the UV and in the optical domains. This kind of instrument is very complex and

needs a very deep knowledge of its intrinsic properties to analyse the data.

The first part of the manuscript will be dedicated to the presentation of the on-board calibration tools and how they could be used to design a calibration unit that fills the needs of an instrument such as the one of Arago. The Arago instrument and mission have been proposed in response to two medium size mission calls from ESA, i.e. M4 and M5. Although the proposal was so far unsuccessful, the work presented here will serve either in a future re-submission of the project to ESA or could be used for the integration of a similar instrument into a larger UV satellite (Pollux on LUVOIR [4], for example) to be proposed to NASA.

## Very Small Missions Feasibility Studies

Since the creation of the Cubesat standard in 1999 and its first launch in 2003 [5][6], a huge number of Cubesat missions have been elaborated, launched and operated successfully. Even though miniaturizing processes are often challenging, these small satellites are now considered as an important support for education at University level and also for scientists all over the world for observation from space. The feasible scientific observations with such small satellites are diverse, from Earth and atmosphere observation with QuakeSat [7] or SwissCube-1 [8] to visible photometry of bright stars with the BRITE constellation [9]. It shows that, even though Cubesats will not entirely replace large spacecrafts and missions, there are a wide range of scientific fields where they can enable innovative focused research [10]. Moreover, Cubesats can serve as demonstrators for new technologies planned on future larger satellites.

The second part of this manuscript is thus dedicated to feasibility studies of scientific Cubesats embarking UV telescopes designed for the observation of massive stars. The first Cubesat envisages a 3U design containing a reflective UV telescope that is able to acquire time series of bright massive stars in the UV domain between 250 and 350 nm. The second Cubesat should embark a UV telescope and a low-resolution static spectropolarimeter that could be used as a technology demonstrator for future missions.

# Part I

# Preparation of an On-board Calibration Unit Concept for a Major Space Mission

# Chapter 1

# On-board Calibration Principles

## 1.1 Calibration of Scientific Space Instruments

### 1.1.1 Principles

Every space optical instrument has to be calibrated in order to know how it responds to a light source and therefore analyse and interpret the observations collected. For a telescope-spectrometer system, for example, many parameters have to be monitored such as the overall transmittance/reflectance of the optical elements, their wavelength response and the sensitivity of every pixel of the sensor that registers the end signal. It has to be stressed though that there exists no unique recipe to calibrate an instrument. The type of calibration data that are needed depends on the nature of the instrumentation and its usage, and frequently even changes over the lifetime of the instrument.

The first step is the pre-flight calibration which is done in laboratory and at every required level (systems or sub-systems). This pre-flight calibration is usually performed inside vacuum chambers where the in-flight conditions of operation are simulated (pressure, temperature) and the targets (stars, Sun, Earth) are reproduced using light sources. For traditional missions, this calibration is a part of the qualification test campaign that serves to validate the mission/instrument design and performance.

The second and last step is the in-flight calibration which is done during the space operations. In general, it is necessary to be able to repeat the calibration performed pre-flight to monitor all the parameters of the instrument which could change over the lifetime of the mission. Indeed, the sensor is aging and its pixel responses will change, the coatings of the mirrors could be contaminated or damaged by large levels of radiation, and so on. Recreating the pre-flight calibration during the mission is quite a challenge because of the complexity of current instruments and the precision that is required. As already mentioned in the Introduction Section, two methods are available for the in-flight calibration:

- Use of celestial standards: it is possible to observe very well-known and constant targets that will allow calibrating the whole optical path of the instrument, telescope included. However, these standards are usually observed from the ground. The differences between conditions during ground observation and in-orbit operations could be a concern. In this context, the UV domain is special as it is not observable from the ground and then the usual standards could be used for UV instruments only by extrapolation of the results in other wavelength ranges by use of theoretical models [3].

- Use of in-flight calibration light sources that are integrated to the payload. The disadvantage is that with this method it is not possible to calibrate the whole optical path because generally these light sources are located inside the instrument and are not illuminating the entrance of the telescope because of technical constraints and the fact that it is impossible to artificially create a point source illuminating the telescope from an infinite distance.

### 1.1.2 CSL Heritage

CSL has a long heritage in space instruments design and testing for many missions from ESA and NASA. CSL has designed and tested the in-flight calibration module for many instruments, and this section presents two of them which are the most recent ones. The common point of these calibration modules is that they are using a wheel mechanism for switching between the different calibration modes and/or observation. These kinds of systems are often complex and considered as possible single points of failure in many cases because if they fail, either the calibration no longer works and the performance degrades or the instrument can no longer be used at all. Therefore the development and the qualification of these components are very critical.

#### 1.1.2.1 OLCI

The Ocean and Land Colour Instrument (OLCI) is an instrument on-board the Sentinel-3 satellite from ESA [11]. Sentinel-3 is part of the Sentinel fleet of satellites which belongs to the Copernicus programme for Earth observation. The main focus of Sentinel-3 is the observation of oceans through the measurement of temperature, colour and height of the sea surface as well as the thickness of sea ice. These measurements allow to monitor changes in sea level, marine pollution and biological productivity. Sentinel-3 is also designed for land observation [11].

OLCI fulfils the objectives of ocean colour determination, as well as some land-cover objectives by simultaneously observing the Earth in 21 spectral bands from the visible at 390 nm to the SWIR (short-wave infrared) at 1040 nm. The instrument is composed of five identical cameras which are pointed towards the Earth. It also hosts a calibration assembly which is made of a positioning mechanism and the associated reference diffusers that re-calibrate the cameras in-flight [12]. Figure 1.1 presents the calibration assembly as it was integrated in the clean room of CSL.

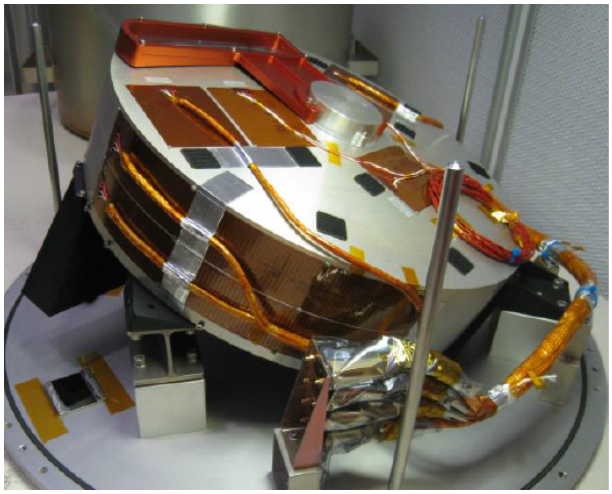

Figure 1.1: Picture of the calibration assembly of the OLCI instrument integrated in the CSL clean room [12].

The diffusers of the calibration assembly work in reflection and allow to perform a photometric and a spectral calibration of the cameras. While the instrument is in its calibration mode, the assembly is oriented to observe the Sun and the diffusers reflect the incoming light to the cameras. There is a total of three diffusers positioned on a rotating wheel assembly: the first diffuser is used as white reference for photometric calibration, the second is redundant to the first one and the last diffuser is used for wavelength calibration. The mechanism also has two other positions used during actual Earth observation (calibration is "off": no diffuser in the optical path) and for dark calibration (there is a shutter that blocks the calibration light from reaching the cameras). Figure 1.2 presents the wheel assembly with its various components.

The example of the OLCI calibration unit is related to the first in-flight calibration technique, i.e. the use of celestial standards. In this case, the standard is the Sun and its light is transformed by the different diffusers, that are very well characterized before flight, to perform specific calibrations (photometric or spectroscopic). The diffusers have to be characterized in laboratory with calibrated standard lamps. Moreover, the degradation of their properties with time has also to be monitored with accelerated ageing tests during which the diffusers are submitted to a large amount of radiation during a relatively short period to simulate the integrated dose of radiation of the entire mission.

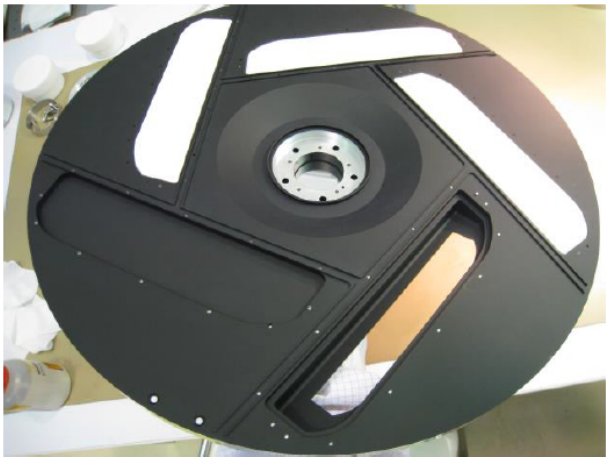

Figure 1.2: Rotating filter wheel assembly of the calibration unit of OLCI. The three diffusers, the shutter and the free window for Earth observation are clearly visible in the picture [12].

#### 1.1.2.2 UVN

The Ultraviolet Visible Near-infrared (UVN) is an instrument that will be on-board the Sentinel-4 satellite from ESA [13]. As Sentinel-3, Sentinel-4 is part of the Copernicus programme but this latter satellite is still in preparation. The Sentinel-4 mission will focus on monitoring the concentrations of trace gases and aerosols in the atmosphere for investigating the evolution of air-quality and climate, mainly over Europe [13].

UVN is a spectrometer that will be used for atmospheric observation in a wide range of wavelengths (from 305 to 500 nm in the UV/visible and from 750 to 775 nm in the NIR). Figure 1.3 presents a picture of the UVN calibration assembly integrated in the clean room of CSL during its qualification test campaign.

The principle of the UVN calibration is based on two separate ways: the first calibration is performed by placing a diffuser between the detector and the Sun, as for OLCI, while the second calibration is performed by switching on an on-board White Light Source (WLS) which generates a collimated beam using a parabolic mirror, an integrating sphere and a slit. As for OLCI, there are a nominal diffuser for the first calibration and a redundant one. They are placed on a rotating filter wheel assembly that has three different positions. The third position is for the parabolic mirror associated to the WLS. Figure 1.4 presents this wheel assembly.

In this example, the calibration unit uses the two in-flight calibration techniques. Indeed, the diffusers are used for a calibration using the Sun as a celestial standard while the WLS provides a well-known beam of light for the calibration of the instrument. The Sun and WLS calibration light is injected in the UVN instrument thanks to a mechanism that allows to switch between observation and calibration modes.

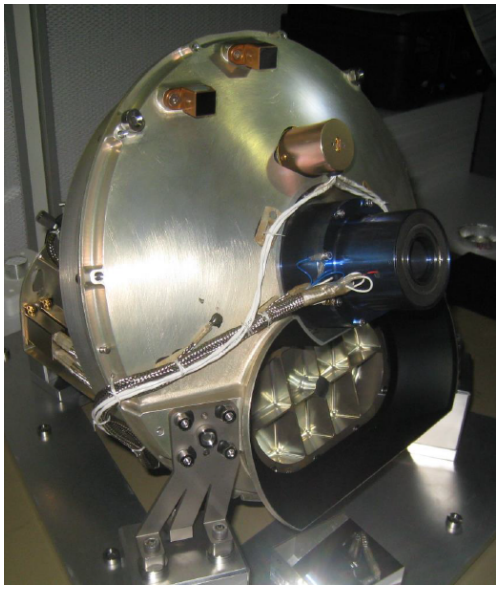

Figure 1.3: Picture of the calibration assembly of the UVN instrument integrated in the CSL clean room.

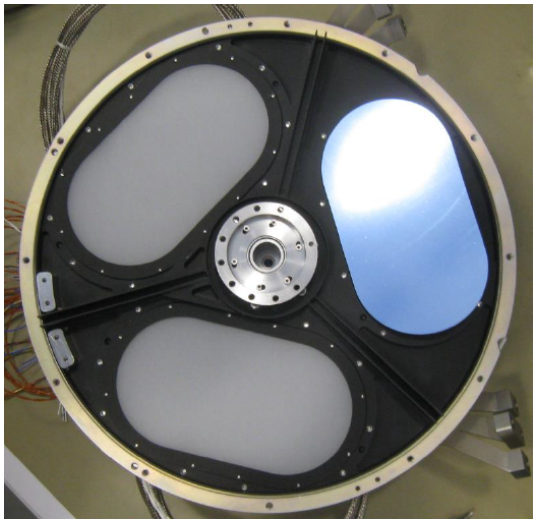

Figure 1.4: Rotating filter wheel assembly of the calibration unit of UVN. The element on the right is the parabolic mirror and the other two are the diffusers.

## 1.2 Calibration Elements

### 1.2.1 Celestial Standards

Celestial standards are a relatively easy way to calibrate optical instruments during a space mission. Indeed, they do not require any on-board components that make the system more complex and that have to be studied, tested and qualified for flying. They can be used for flat field or even for wavelength calibration.

Celestial objects such as the planets of our solar system (Mars, Jupiter, Saturn), or well-known and luminous stars (including the Sun) are very good candidates for being standards for the calibration as they have been observed precisely from the ground with a lot of different instruments [3]. Calibrated ground-based observations are thus available, hence their spectral properties are fully characterized. It is then possible to observe them with the in-orbit instrument and establish the calibration. It has also to be noted that cross-calibration is possible, as these standards can also be observed with other spaceborne facilities such as the Hubble Space Telescope (HST) that carries in-flight calibration units.

The disadvantage of this technique is that some wavelength domains cannot be covered from the ground, such as the UV domain which constitutes the main interest of this manuscript. In order to avoid this problem, theoretical mathematical models are often used to extend the results to unobservable domains [3]. As mentioned above, cross-calibration could also be used for establishing the standards though not all the needed wavelength domains may be covered.

Eventually, a problem with celestial standards is that they lack information for the calibration of very high resolution spectrometers. Indeed, for the wavelength calibration of this kind of instrument, one needs to illuminate it with a light source containing a very high density of spectral lines with well-known and stable wavelengths all over the observational domain, a case which rarely exists in nature hence the need for other solutions (Section 1.2.3).

### 1.2.2 White Light Sources

White light sources are usually needed for flat field calibration. The ideal white light source should provide an output as flat as possible with respect to wavelength. A flat output is needed to remove the wavelength dependence for the specific flat field calibration that characterizes the sensitivity variation between pixels of the detector. Moreover, the wider wavelength range it covers, the better it is.

An example of a white light source which was used in several space missions is Quartz Tungsten Halogen (QTH) bulbs for the calibration of instrument in the visible and NIR spectrum. These lamps are made of a Tungsten filament crossed by an electric current and which is inside a Quartz bulb filled by Halogen gas [14] (Figure 1.5). They operate as thermal radiators (they are based on incandescence principle), meaning that light is generated by heating a solid body (the Tungsten filament) to a very high temperature. Therefore, the higher the operating temperature, the brighter the light will be.

This kind of lamp generates a relatively flat continues spectrum of light. The spectral domain covered by the lamps depends on the materials used for the filament and the gas surrounding it and also on the working temperature that can be reached because the emitted light is similar to a black body radiation (the maximum

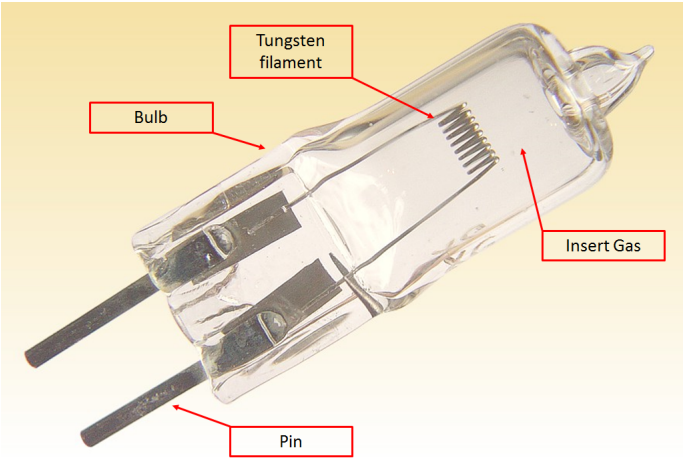


Figure 1.5: Example of a commercial QTH bulb.

of emission follows Wien's law). It is possible to cover the spectral domain from UV to IR using the right combination of materials and working temperatures.

Another kind of lamps producing a continuous spectrum in the UV are the Deuterium arc lamps (Figure 1.6). They are working on another principle: a tungsten filament and an anode are placed inside a nickel box structure. Unlike the previous lamps, the filament is not the source of light and instead an arc is created from the filament to the anode which excites the molecular deuterium contained within the bulb. The deuterium eventually emits light as it transitions back to its initial state [15].

Figure 1.6: Example of a commercial Deuterium arc lamp [15].

It has to be noted that the spectra of QTH or Deuterium lamps are not perfectly flat over the wavelength domain that they cover. The ideal WLS with a constant output over all the spectrum does not exist. Therefore we have to work with the available sources and take into account the intensity variations as a function of the wavelength to calibrate the instruments with these lamps. Moreover, a WLS that covers the entire spectrum does not exist either. To cover a wide spectral range, several lamps with different properties have to be used.

### 1.2.3 Hollow Cathode Lamps

A Hollow Cathode Lamp (HCL) consists of an anode and a cathode inside of a glass tube. An inert gas is placed inside the glass tube. A schematic representation of a HCL is presented in Figure 1.7.

When a high voltage is applied between the anode and the cathode, the gas inside the tube starts ionizing, creating a plasma. The ions are then accelerated into the cathode, sputtering off atoms from it. After that, both the gas and the sputtered cathode atoms are excited by collisions with other particles in the plasma. Eventually these excited atoms decay to lower states thereby emitting photons at precise wavelengths, depending on the inert gas and the cathode material [16].

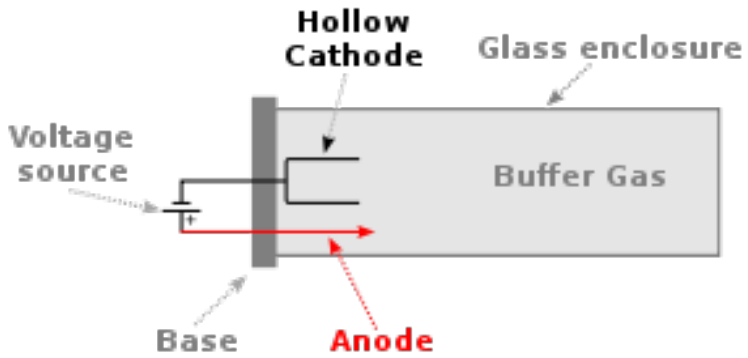


Figure 1.7: HCL overview and concept [16].

This kind of lamps have been widely used for in-flight calibration of scientific space missions such as IUE and several spectrographs on HST. The most important property of HCLs is that they provide a very rich spectrum full of sharp spectral lines. Therefore they are ideal for wavelength calibration of various species of instruments [17].

The main drawbacks of HCLs is that they suffer from ageing. Their intensity fades by factors between 5 and 15 after thousand of hours of use and this drop of intensity is not constant over the wavelength domain covered by the lamps [18]. Moreover, the operating voltage for a given current increases with time [17]. It is possible to calibrate these effects by performing accelerated aging tests at laboratory level to characterize the performance of the lamps over time.

# Chapter 2

# Application to the Arago Mission for the M4 and M5 Calls from ESA

## 2.1 Mission Presentation

### 2.1.1 Scientific Objectives

During the formation and the entire life of stars, several key astrophysical parameters such as magnetic fields, stellar winds and binarity, for example, influence their dynamics and evolution. Whilst the basic principles of these influences are known, their details are not well understood, and the observational determination of some of these parameters (magnetic fields) is required to achieve a deep understanding of their impact, especially during crucial short-lived phases of stellar evolution.

The Arago mission proposes for M5 to address these topics in the context of the following two questions:

- What is the life cycle of matter in the Milky Way?
- How do stars affect their planets and the emergence of life?

The GAPHE team, involved in the scientific consortium of Arago, is mainly concerned with the first question. The study of massive stars will be treated by answering several sub-questions thanks to the foreseen UV data:

1. What is the role of **magnetic fields** during the stellar formation and evolution?
    - Ionized outflows are submitted to electromagnetic forces which therefore influence/control the *mass-loss* of magnetic massive stars. Several phenomena such as the reduction of mass-loss, the magnetic confinement of

stellar outflows, and the braking of stellar rotation [19] are consequences of the wind-magnetic field interaction but there is a lack of data to fully understand them.

- Observations of magnetic fields of massive stars at the more *advanced stages of their life* (WR[1] for example) provide a crucial source of information to constrain how these fields evolve over the lifetime of the stars.
- Massive stars perish dramatically in *supernovae explosions* that provide strong feedback to the interstellar medium [20]. The UV domain is well suited to study the remnants of these explosions.

2. What are the 3D structure, geometry and dynamics of the **stellar environments** throughout the star's evolution?

    - Massive stars are part of the most important drivers in the evolution and the processes occurring within galaxies. Stellar winds are at the center of interest here but large uncertainties on their properties still remain. These uncertainties could be removed by observing UV line profiles of the stars and their associated polarization.

### 2.1.2 UV and Visible Spectropolarimetry

The scientific objectives of Arago impose to observe stellar spectral lines in a wide range including the visible and UV wavelength domains. The Arago scientific consortium has therefore defined the necessary wavelength range to be covered as **[119-888] nm**, providing a broad spectral coverage including all critical UV and visible spectral diagnostics required to achieve the science goals.

### 2.1.3 Circular and Linear Spectropolarimetry

In addition to the measurement of the stellar spectra (Stokes[2] I), the science goals defined above require the measurements of circular polarization (Stokes V) in the spectra to detect and quantify the magnetic field as well as of linear polarization (Stokes Q and U) to fully characterize the 3D configuration of the magnetic field and of the circumstellar environment [21]. Therefore, Arago is designed to be able to measure **all Stokes (IQUV) parameters** over most of its wavelength domain.

### 2.1.4 Instrument

The payload of Arago consists of a 1.3-meter Cassegrain telescope and a polarimeter placed in front of two spectrographs working in the [119-320] nm and [350-888] nm spectral ranges respectively. The two spectrographs have different spectral resolutions which are defined by the scientific needs of the mission. The

[1] Wolf-Rayet stars are evolved massive stars with unusual spectra showing prominent broad emission lines of highly ionised helium and nitrogen or carbon. The spectra indicate very high surface enhancement of heavy elements, depletion of hydrogen and strong stellar winds.

[2] For more details on polarization and the Stokes parameters, see Appendix A.

visible/NIR spectrograph requires a minimum resolution of 35000 which is equivalent to first generation on-ground instruments (such as MUSICOS [22]) while the UV spectrograph requires a minimum resolution of 25000 which is sufficient for the study of the stellar environment. There is a gap in the spectral domain of the UV and optical channels (between 320 and 355 nm) which is acceptable since it does not include scientifically important lines.

The telescope forms a F/13 beam that enters the polarimeter just after its focal plane. The polarimeter consists of a modulator followed by a polarisation separator. At the end of the polarimeter, the two orthogonal states of polarisation (produced by a Wollaston polarizing beam splitter) enter a dichroic plate which reflects the UV light and transmits the visible/NIR wavelengths in their respective spectrograph and detection chain. The visible/NIR detection chain uses a Charge Coupled Device (CCD) sensor while the UV detection chain uses a Microchannel Plate (MCP) assembly. These kind of sensors will be introduced and compared in Section 4.3.2.

## 2.2 Perimeter of Belgian Activities

From the technical point of view, two Belgian entities are involved in the consortium of Arago: the CSL and the Institute of Astrophysics in Leuven (KUL). Belgium is responsible for the internal calibration module (design, module procurement of all models, qualification and tests) and for the on-ground calibration (setup facilities and tests).

CSL is in charge of developing the on-board calibration module and the ground calibration hardware while the KUL will focus on EGSE (Electric Ground Support Equipment, used during the tests and calibration of the instrument on ground), software and ground calibrations.

During the preparation of the M4 and M5 proposals, the focus was put on the development of the on-board calibration module that could meet the requirements and the needs of the mission because it is the most challenging part of the Belgian responsibilities.

## 2.3 Calibration Requirements

This section lists the points that require in-flight calibration in order to achieve and maintain the scientific performances of the Arago instrument. Some of these points need a dedicated solution added to the payload while the others are calibrated through special observations without any additional component on-board.

### 2.3.1 Offset

The detector offset should be measured via series of zero integration time exposures and is then subtracted from the measured signal to obtain the scientific data.

It does not set any requirement on the calibration unit.

### 2.3.2 Dark

The detector dark current should be measured via series of dark exposures of various durations. Therefore the calibration unit should include a shutter mode where no light (from the sky or the internal light sources) illuminates the detector of the instrument.

### 2.3.3 Flat Field

The flat field (FF) calibrations serve several purposes that are listed in the following sections.

#### 2.3.3.1 Pixel Response Non Uniformity

The Pixel Response Non Uniformity (PRNU) is a problem arising at the detector level and it is due to variations in the response of the individual pixels. It might be caused by variations in the pixel size for example. Hence, it is wavelength-independent and, a priori, this effect can be calibrated on the ground by uniformly illuminating the detectors with white light sources.

However, the aging of the detector and the influences of the space environment need to be monitored on a regular basis. Thus, a specific internal light source is required to perform this measurement in-flight. It needs to be as spectrally uniform as possible and it must illuminate all parts of the detectors that are used for scientific or calibration purposes. It is hence necessary to inject it ahead of the polarimeter to calibrate the areas receiving the two polarizations from the sky.

#### 2.3.3.2 Blaze Function and Cross-order Profiles

In an echelle spectrograph, several diffraction orders are depicted in the final imaging detector. Each order is associated to a blaze function that represents the relative intensity of the signal transmitted by the grating as a function of the wavelength. It is also important to correctly calibrate the cross-order profiles to avoid extracting spectra in regions of the detector where the signal from two adjacent orders may overlap.

The blaze functions and cross-order profiles should be calibrated via the same light source as for the PRNU.

#### 2.3.3.3 Linearity

The linearity of the detector's response with respect to the incoming flux can be estimated on the ground. It also can be monitored in-flight via series of FF measurements of varying duration.

### 2.3.4 Relative Spectral Response Function

The Relative Spectral Response Function (RSRF), i.e. the global spectral transfer function of the instrument can be measured and must be regularly monitored via observation of celestial standards of which the spectrum is known or can be modelled with sufficient accuracy.

This point does not impose any requirement on the calibration unit.

### 2.3.5 Wavelength Calibration

The Stokes parameters describing the polarization of the light are part of Arago's main scientific outputs. The extraction of these parameters is done by demodulating the signal recorded in two perpendicular states of polarization and in several position angles of the polarimeter. It is hence of paramount importance that:

i. The instrument remains as stable as possible during the complete series of observations to be combined in the analysis. It has been estimated by the scientific team of Arago that a displacement of the spectrum between the data of a given observing sequence exceeding 1/15 of a pixel is sufficient to compromise the polarization measurement.

   - This places stringent requirements on the pointing stability as well as on the thermal stability of the payload to ensure that the wavelength solution (correspondence between pixel coordinates and wavelength) remains as stable as possible during the whole observation sequence. Indeed, if there are movements of the target with respect to the slit they can affect the spectral profiles and degrade the spectral resolution.

ii. The wavelength solution can be measured for every observation with a very high accuracy. This second point places requirements on the layout of the calibration unit and the light source used for the wavelength calibration:

   - The source must contain a sufficient number of spectral lines in every spectral order to guarantee a complete and accurate wavelength solution.
   - For establishing an accurate wavelength solution and monitoring it at regular intervals, the light from the wavelength calibration source must pass through the same optical path as the light from the celestial targets. The source must hence be injected in the path ahead of the polarimeter. In addition, the source must be usable for a long time, since such calibrations will be performed at high cadence.

### 2.3.6 Calibration of Polarization

There are several effects that modulate the polarization of the signal through the entire instrument [23]:

- Induced/instrumental polarization which is associated to the optical elements of the instrument;
- Cross-talk effects;
- Polarization rotations which characterize the rotation of linear polarization states;
- Influence of polarization on photometry.

The instrumental polarization modulation is characterized by the Mueller matrix of the complete optical chain[3]. This matrix is the product of the matrices of each optical element in the chain. A good determination of these matrices during the ground tests is essential.

The optical elements most susceptible to aging in-flight include the main mirror and the entrance optics, all placed before any possible injection point of on-board calibration sources.

The baseline, established in agreement with the consortium for the calibration of the polarization, contains a thorough on-ground calibration of instrumental polarization, and an in-flight monitoring thanks to celestial standards. Consequently, no optical element dedicated to introduce or modulate the polarization is necessary in the calibration unit.

### 2.3.7 Intra-pixel Response Non Uniformity

In theory, the Intra-pixel Response Non Uniformity (IPRNU) can be calibrated by moving point sources around the detector with sub-pixel scale displacements. In practice this is very difficult to implement, and is extremely time-consuming.

If necessary, it will be calibrated at component level on the ground and therefore no requirement on the calibration unit is added.

[3]See Appendix A for more details on the Mueller matrix formalism.

## 2.4 Calibration Unit Preliminary Design

### 2.4.1 Block Diagram

Figure 2.1 shows the block diagram of the calibration unit integrated in the instrument of Arago.

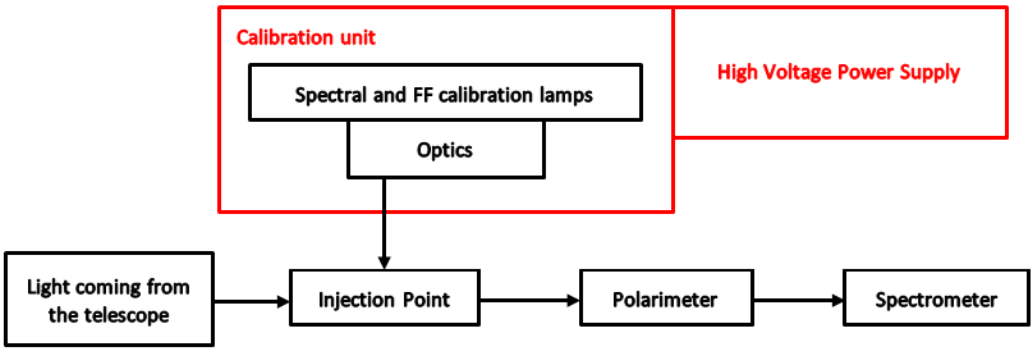


Figure 2.1: Block Diagram of the calibration unit integrated in the Arago payload.

The calibration unit box includes an Optics box because some optical elements need to be integrated in order to inject an F/13 beam in the optical path of the instrument.

The Spectral and FF calibration lamps box contains calibration lamps needed to cover the requirements exposed in Section 2.3.

The Injection Point box, which is outside the calibration unit, is obviously directly related to calibration. Anticipating the results of the next sections, it is composed of optical elements mounted on a mechanism which inject the optical beam coming from the calibration unit in the optical path of the instrument.

Eventually, there is also a high voltage power supply box in the block diagram. This box is required because of the kind of light sources selected for the calibration unit, again anticipating the next sections.

### 2.4.2 Calibration Light Sources

#### 2.4.2.1 Flat Field Sources

In order to cover the wide spectral wavelength range of Arago, it is necessary to use several FF calibration sources. The spectral domain is indeed too wide ([119-320] nm and [350-888] nm) to be covered by a single lamp.

The first proposed light source which is able to cover the visible and NIR spectral parts of the Arago instrument is a QTH bulb lamp (concept presented in Section 1.2.2). As it can be seen from Figure 2.2, the relative intensity spectrum is not perfectly flat. The maximum is reached approximately at 600 nm and then the intensity decreases at shorter wavelengths while it remains relatively constant for larger ones. Near 350 nm, the relative intensity becomes lower than one percent of the maximum value. However this kind of lamp is still a very good candidate for the FF calibration between 350 and 888 nm, i.e. over the second part of the Arago spectral domain. If the spectrum of the lamp is well established during the qualification program, the relative intensity decrease between 350 and 600 nm should not be a problem. Qualifying the output of the calibration lamps and integrating them to the instrument to verify the entire chain is obviously a part of the development program in such ambitious projects.

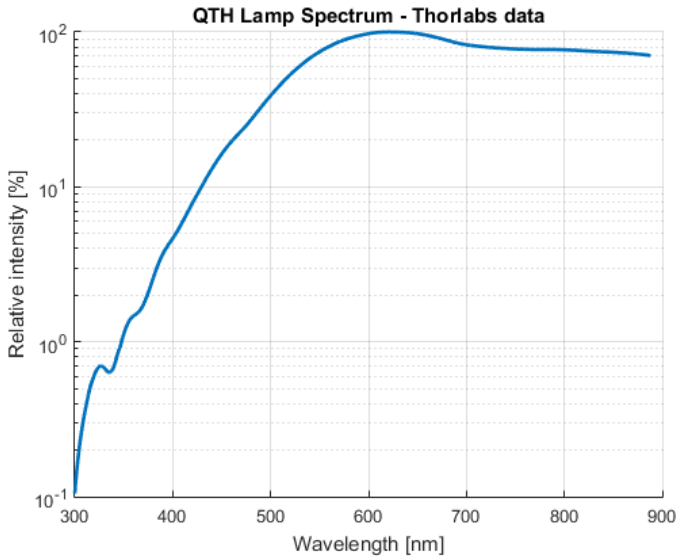


Figure 2.2: QTH bulb spectrum of a commercial lamp from Thorlabs [24].

Moreover, QTH lamps have already a space mission's heritage. Indeed, the SCIAMACHY instrument on the ENVISAT satellite (operational from 2002 to 2012) used QTH lamps for its in-flight calibration. SCIAMACHY was an imaging spectrometer performing global measurements of trace gases in the troposphere and the stratosphere. It was working over a wider spectral domain than Arago, from 240 to 1700 nm and in selected regions between 2000 and 2400 nm [25]. The calibrating module of UVN (see Section 1.1.2.2) is also using QTH bulbs from Welch Allyn for the WLS part. The bulbs are illuminating the integrating sphere which transfers the light to the parabolic mirror mounted in the wheel mechanism. The light is reflected by the mirror into the instrument for calibration.

The second proposed light source, needed for covering the UV spectral domain, is a Deuterium arc lamp. Indeed, Deuterium lamps have their maximum intensity

emission between 150 and 200 nm with a relatively narrow peak. As can be seen from Figure 2.3, the relative intensity spectrum is not perfectly flat as for the case of QTH bulb lamps. The advantage of Deuterium lamps is that they have a strong intensity in the UV from 117 to 170 nm. Beyond this point, intensity is decreasing and drops below one percent of the peak intensity around 260 nm. The fact that the relative intensity is very low between 260 and 320 nm in the instrument operational range is not necessarily an issue considering the throughput of the instrument that will be very high at these wavelengths owing to high optical and detector efficiencies.

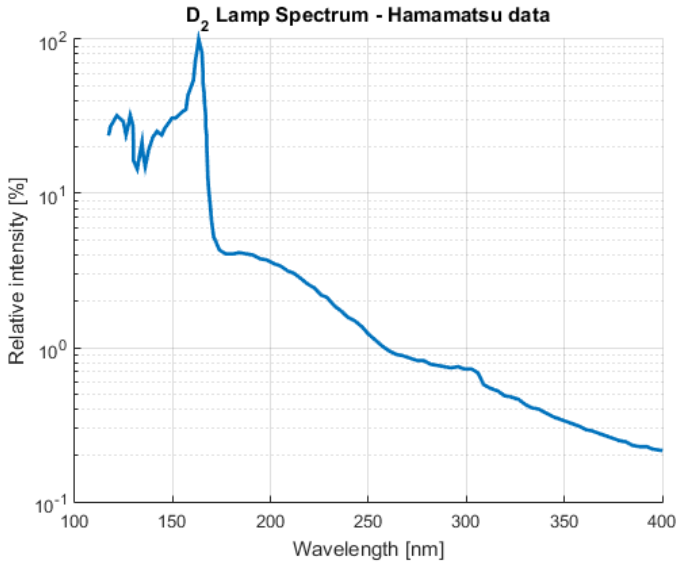


Figure 2.3: Deuterium arc lamp spectrum of a commercial lamp from Hamamatsu [26].

As for QTH bulbs, Deuterium lamps have a strong heritage from space missions such as IUE or HST where they were used for FF calibration of COS [27].

#### 2.4.2.2 Wavelength Calibration Source

The most suitable choice for the spectral calibration lamp is a Platinum-Neon (Pt-Ne) HCL. This kind of calibration lamp has the advantages to have a very strong heritage in space missions such as IUE and HST and also to cover the UV spectral domain from 113 to 320 nm with more than 3000 spectral lines [17][18]. In order to cover a wider spectral range with a high density of spectral lines, it is possible to add about 10% of Chromium (Cr) to the cathode. This was done for the STIS instrument on the HST to get a continuous distribution of emission lines over the range 115-800 nm [28]. Figure 2.4 presents, in log scale, a full STIS spectrum of the HCL.

It has to be noted that the spectrum is not limited to 800 nm as it is specified in [28]. Figure 2.4 clearly shows that the spectrum extends at least up to 900 nm, allowing to cover the entire spectral domain of Arago. Since this lamp covers such

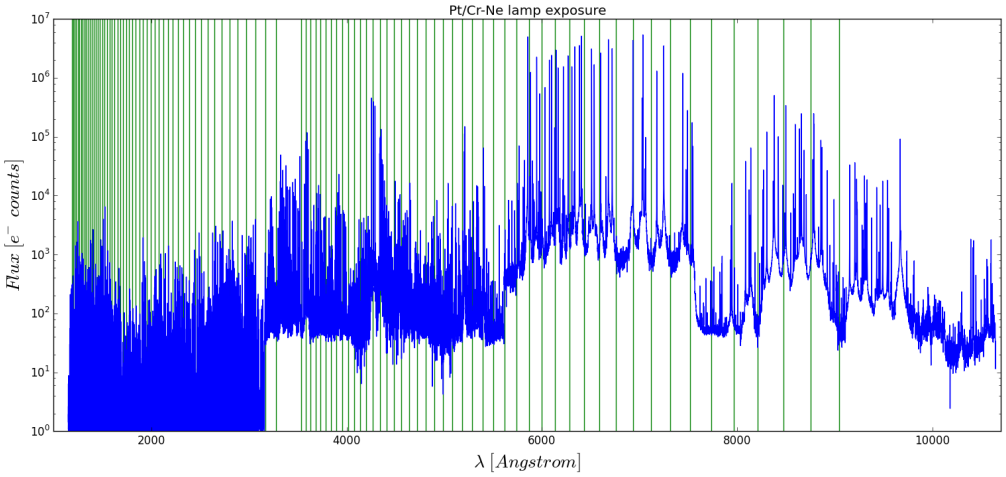


Figure 2.4: STIS Pt-Cr-Ne reference spectrum from [29] and [28].

a broad range of wavelengths, it can provide a suitable solution for the wavelength calibration of the full domain of the spectropolarimeter of Arago. The density of spectral lines is somewhat lower in parts of the visible and NIR domains than in the UV domain. However, it has been verified with the Arago consortium that the number of lines over the entire spectral domain is sufficient to achieve the calibration needs[4].

### 2.4.3 Mechanical Parts

Figure 2.5 presents the 3D overview of the calibration unit box and its injection point box as it should be integrated in the optical path of the Arago instrument. The parts composing these boxes are discussed in the following sub-sections.

#### 2.4.3.1 Calibration Unit Box

The calibration unit box is composed of two main assemblies: a wheel assembly carrying the calibration light sources and a mirror assembly.

The first element is the Lamp Wheel Assembly (LWA, Figure 2.6). The calibration lamps are mounted on a mechanism in order to be able to select them for different calibration modes. This design choice results from the fact that several light sources are used, two for FF and one for wavelength calibration, and that it is neither possible nor meaningful to use them simultaneously. There are three identified calibration modes: visible and NIR FF calibration using the QTH bulb lamp, UV FF calibration using the Deuterium arc lamp and wavelength calibration using the Pt-Cr-Ne HCL. Each lamp is mounted on the wheel with a redundant version in case of breakdown or unexpected degradation. At this preliminary stage of the

[4]It was also mentioned in the proposal of Arago for M5 that a more classical Thorium-Argon (Th-Ar) HCL could be used as a backup solution for the visible and NIR parts of the spectrum.

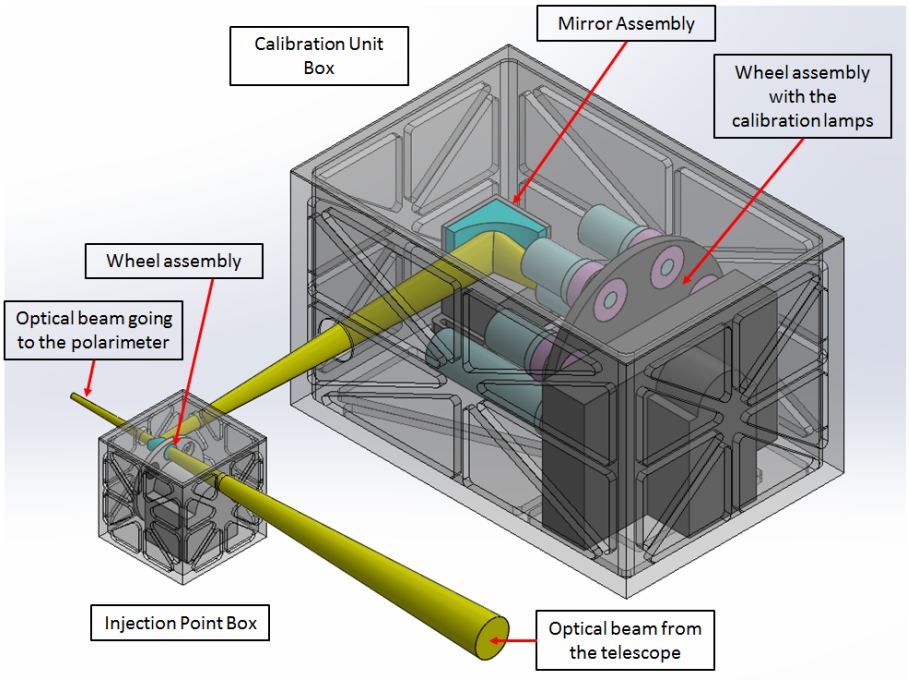


Figure 2.5: Overview of the Calibration Unit Box and the Injection Point Box preliminary designs for the Arago instrument.

design, it is not possible to affirm that a single redundant lamp for each kind of lamp is sufficient or if a second redundant element is needed.

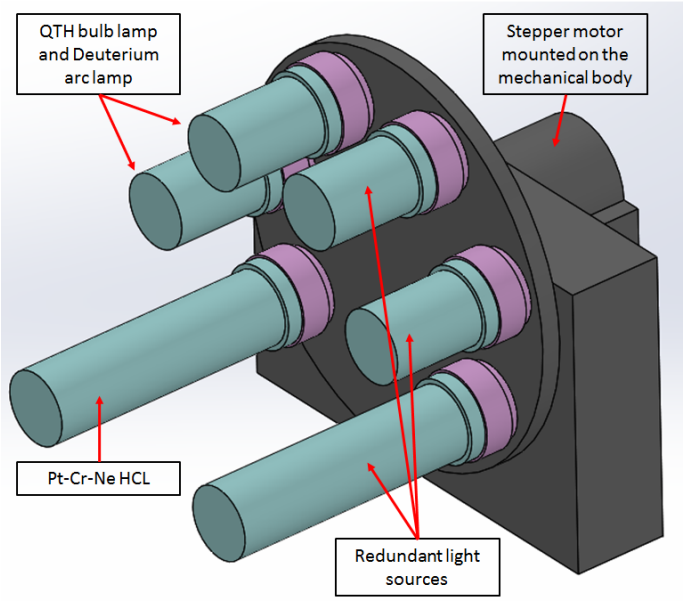


Figure 2.6: Overview of the LWA which is placed inside the calibration unit box. It is composed of a mechanical body on which a stepper motor is mounted. The motor is connected to a wheel part on which the calibration lamps are placed.

The use of an integrating sphere connected to all the light sources was also studied during the proposal preparation. The advantage of such devices is that they prevent the use of a wheel mechanism which is complex and also defined as a single point of failure, hence is critical. However, after some contacts with manufacturers such as Spectralon, it was found that the use of these spheres at wavelengths below 180 nm is not possible because of the reflectivity of the coatings that decreases in this spectral domain. Because of the very large number of reflections occurring inside the sphere, the losses become prohibitive.

The second element is the mirror assembly which is positioned in front of the LWA. The mirror is used to reflect the light from the lamp which is positioned in front of it for the calibration. The light is reflected in the direction of the injection point box which is placed in the optical path of the Arago instrument.

#### 2.4.3.2 Injection Point Box

The injection point box main element is a small wheel assembly which has three distinct positions (Figure 2.7)

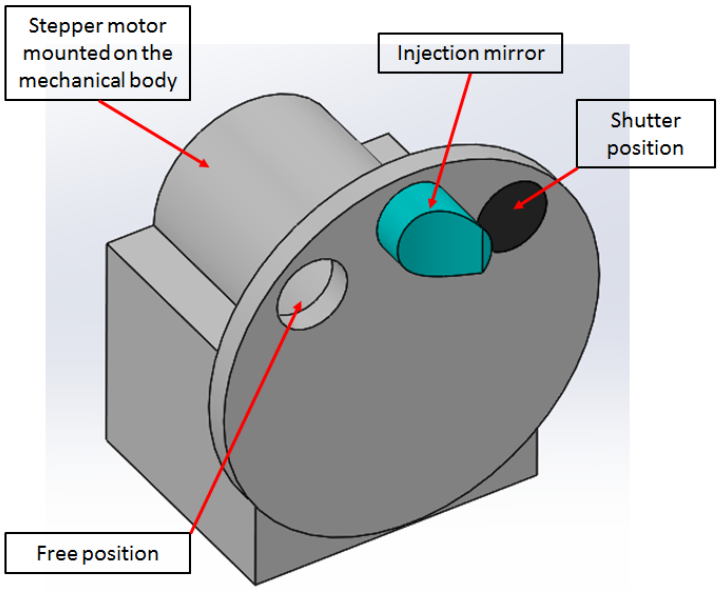


Figure 2.7: Overview of the Wheel Assembly which is placed inside the injection point box. The design is relatively similar to that of the LWA.

The three positions of the wheel assembly are the following:

- **Mirror position**: the injection mirror is placed in the optical path and the light from the calibration unit box is reaching its surface. The light from the calibration sources is reflected by the injection mirror to the direction of the polarimeter of the instrument. The association of the two mirrors of the

calibration unit should be designed to recreate an optical beam with an f-number similar to that of the telescope of Arago. For this purpose, a simple association of elliptical mirrors is sufficient. Some special care will be needed during pre-flight on-ground calibration to establish the Mueller matrices of the combination of the mirror assembly and the injection mirror as the reflection on these mirrors will introduce instrumental polarization into the light of the calibration sources.

- **Shutter position**: a shutter is placed in the optical path and prevents the light from the sky to reach the detection chains and allows performing dark calibration. The lamps from the calibration unit box are then assumed to be in an off state.

- **Free position**: nothing is placed in the optical path and the light from the sky is reaching the polarimeter and the detection chains. This is the observing mode. The lamps are also assumed to be off in this configuration.

It has to be noted that in case of failure of the drive of the wheel, the light from scientific targets have to go through the injection point box. It means that the natural position of the wheel should correspond to the free position and that it must always come back to this position when the system is not controlled.

### 2.4.4 Power Supply Considerations

The calibration unit is designed for working with several HCL. These lamps are working with high voltage current as it can be seen in [17]. Typically, a HCL needs about 300 V and 10 mA for ignition and 200 V and 10 mA for steady-state operation.

The main electronics of the Arago satellite, however, is designed to provide all the systems with a voltage of only 28 V which is obviously not enough for the calibration unit. This situation imposes the definition of a power supply box dedicated to the calibration unit.

Referring to [30], there are three ways of packaging high voltage assemblies in instruments: solid potting, conformal coating and completely bare. Each of these packaging have several advantages and disadvantages. For example, the solid potting packaging is very well insulated and is then protected from contamination and external electromagnetic fields but it is heavier than the other solutions.

In this specific case, the power supply can be made of a transformer powered by the main electronics of the satellite and converting the low voltage (28 V) into high voltage (200-300 V). Indeed, the principle of an ideal transformer is the following (Figure 2.8): A magnetic core is used to couple the primary and secondary circuits. An AC electrical current in the primary winding (red part in Figure 2.8) creates a varying magnetic flux in the core which affects the secondary winding (blue part in Figure 2.8). Therefore it induces an alternative voltage in the secondary winding.

Combining Faraday's law and the energy conservation, it is possible to write for the ideal system:

$$V_S = V_P * \frac{I_P}{I_S} = V_P * \frac{N_S}{N_P} \tag{2.1}$$

In Equation 2.1, $V$, $I$ and $N$ stand for the voltage, the current and the number of winding turns in the primary (index $p$) and secondary (index $s$) windings (Figure 2.8). Using the adequate ratio $\frac{N_S}{N_P}$, it is thus easy to convert the 28 V input from the main electronics in a suitable voltage for the lamps.

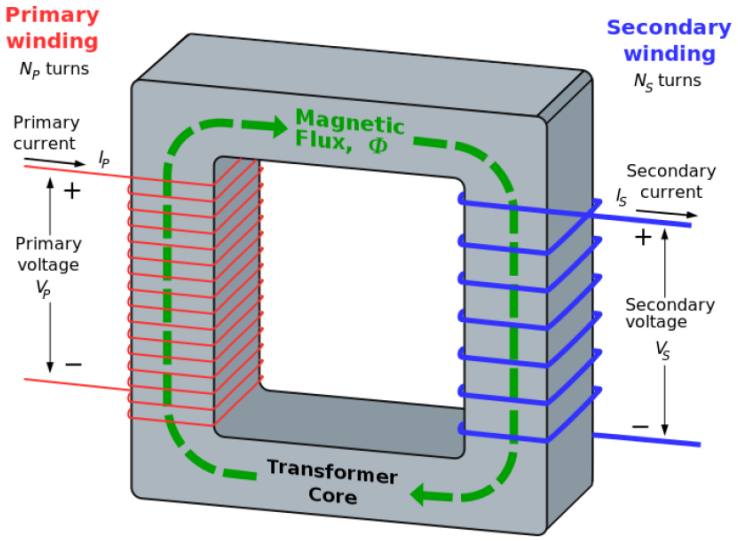


Figure 2.8: Ideal electrical transformer principle [31].

In a real transformer, some effects such as hysteresis, Joule losses and leakage flux have to be considered. Therefore, the efficiency of a real system is not 100% but according to [31], it usually reaches 90%.

Due to magnetic effects, the system should be isolated from the other parts of Arago's instrument and electronics. A suitable shielding should be designed to insulate the transformer part, which would increase the weight significantly. As a consequence, the solid potting packaging seems to be the best solution despite its larger weight. Bever et al. [30] gives a lot of advice and precautions to take to design such space components, as well as the tests necessary to qualify them.

# Part II

# Very Small Missions Feasibility Studies

# Chapter 3

# Cubesats Missions

## 3.1 Cubesat Standard

### 3.1.1 Overview

The Cubesat standard has been proposed in 1999 as a collaborative effort between Prof. Jordi Puig-Suari at California Polytechnic State University (Cal Poly), San Luis Obispo, and Prof. Bob Twiggs at Stanford University's Space Systems Development Laboratory (SSDL) [6]. The goal is to have at hand a standardization of very small satellite platforms in order to reduce costs and development time and increase accessibility to space while involving students in the development of space projects.

A Cubesat unit is a 10 cm cube with a mass up to 1.33 kg and should be compliant with the specifications of [6]. Since the beginning of the standard in 1999, many Cubesat developers have emerged and propose standardized platforms and sub-units such as computer, solar panels, communication systems and so on. They propose a wide variety of solutions that, for a large part of them, already have a space heritage.

It is also interesting to note that Cubesats have their own standardized orbit deployer which is called the Poly Picosatellite Orbit Deployer (P-POD), designed by Cal Poly. Figure 3.1 shows an overview of a P-POD and a three-unit Cubesat that should be mounted inside the P-POD before launch. The P-POD is a rectangular box with a door and a spring mechanism that, when activated, eject the Cubesat outside the box. The design of a Cubesat satellite should also be compatible with the P-POD design in order to ensure safety and success of the mission [6].

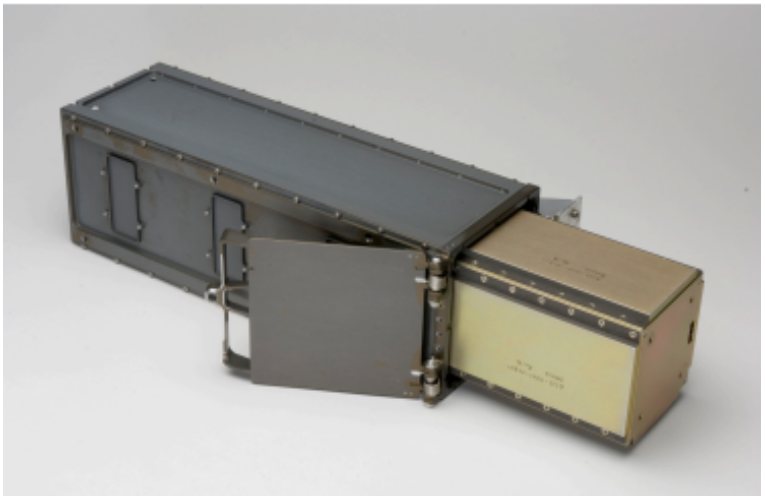

Figure 3.1: Overview of a P-POD and a three-unit (3U) Cubesat [6].

### 3.1.2 Interests for Cubesats

Cubesats are used for four main purposes [32]:

- **Education**: Because of the lower costs and the relatively easy access to launches, Universities all over the world have encouraged students to invest their master and PhD theses in research work on Cubesats designs, with different and varied purposes. This thesis is one example of this objective while the OUFTI-1 satellite, built at the University of Liège by students who worked on the project from 2008 to 2016 for their master theses, is another one.

- **Technology Demonstration**: The low cost of Cubesats, the less rigid risk management and the relatively short development time are also an advantage for research centers of industrials that want to test a new technology concept, like a specific mechanism or instrument. It has to be noticed that for large space missions, the risks have to be minimized. With that philosophy in mind, it is quasi impossible now to introduce new technologies on large missions because any malfunctioning or failure will cost a huge amount of money to the space agencies. Before the introduction of a new concept, we thus have to rise its Technology Readiness Level (TRL) to make it possible to fly on a satellite. A low cost Cubesat mission is perfect for rising TRLs of new concepts.

- **Science**: This third point can be easily related to the two previous ones. Since the beginning of the standard, many scientific Cubesats have been launched and operated. Some of them were designed by students, some had scientific objectives, some tested new technologies, or a combination of those [32].

- **Communications**: This last point is the least abundant in the field of Cubesats because the size of the platforms is usually not sufficient to compete with the large communications satellites that come from industry. However, according to the list of Cubesats missions of [32], a few communication Cubesats were

launched mostly for amateur radio service.

The purpose of the next chapters is to present feasibility studies of Cubesat systems designed for astronomical observations. These are thus all related to the third point of the list, science. Eventually, in Chapter 5 a new concept of polarimeter that has never been used in any space instrument will be presented. The purpose of this latter research is to demonstrate that this polarimeter can be accommodated on a small satellite in order to test it in-flight and rise its TRL. The technology demonstration aspect is therefore also under consideration, along with the education purpose since this work is part of a thesis.

## 3.2 Cubesats in Astronomy and Astrophysics

It appears from [32] that most of the Cubesats launched until 2013 that had a scientific purpose were intended for Earth observation. This trend is confirmed in [33] and [34], where we can see that Cubesats have not been used so much for astronomy and astrophysics. To give an example: according to [34], between 2013 and 2017 NASA sponsored 104 Cubesats in which only one is devoted to astrophysics: HaloSat (still under development, see Section 3.2.3.1).

This section is dedicated to the presentation of past or present successful astrophysics missions using Cubesats platforms and other ones that are currently in their final phases of conception or planned to be developed.

### 3.2.1 BRITE

BRITE is the acronym for BRIght Target Explorer. It is a constellation of nanosatellites which are designed for astrophysical research, resulting from a collaboration between universities from Austria, Canada and Poland [9][35]. Six satellites were launched between 2013 and 2014 and five of them are operating, performing precise optical photometry of the brightest stars in the sky. The sixth one did not detach from its launcher.

Figure 3.2 presents an overview of the BRITE satellites structure. The Cubesats of the BRITE constellation are composed of eight units (8U, $20 \times 20 \times 20$ cm). Figure 3.2a shows an exploded view of the satellite with its key components labelled. We can notably see in the interior of the satellite the On-board Computers part for the control of the system, the optical payload and some sensors (star tracker and sun sensors) and reaction wheels for the attitude control. The exterior is composed of panels on which solar panels are placed for the power supply and several antennas are also integrated for the communication with the ground stations. Figure 3.2b shows a picture of one of the BRITE constellation's fully integrated satellite before launch.

The instrument on-board the satellites is an optical photometer composed of several lenses that focus the light onto a CCD detector [35]. As it is explained in

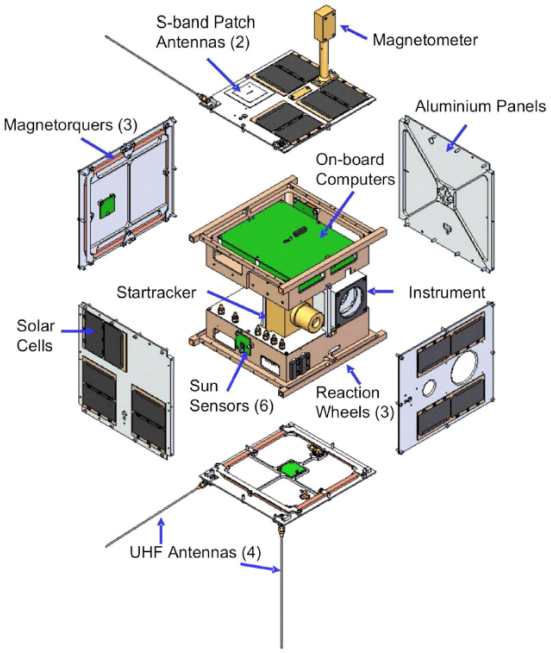


(a) Schematic overview of the BRITE satellites structure with the key components labelled [35].

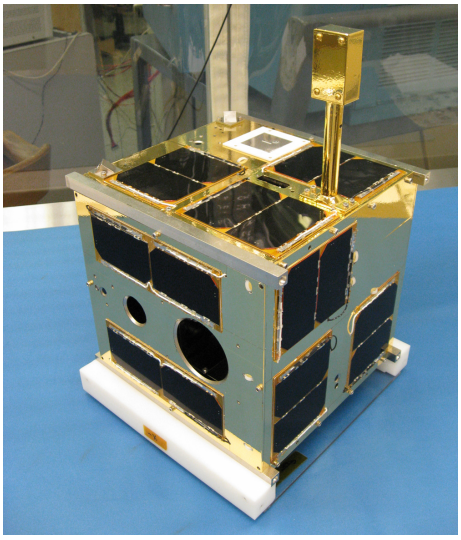

(b) Picture of one of the satellite from the BRITE constellation [36].

Figure 3.2: Overview of the BRITE satellite structure.

[35], the detector is not cooled by any means and therefore its operational temperature is around 20°C, which is very high for this kind of detector. Indeed, CCDs are subject to several noises such as the dark current which increases with temperature. Other space missions using these detectors control the temperature of their detectors in order to have them at -40°C or below. This way, the data acquisition is more efficient and the scientific results are improved. However, according to [35], the results of the BRITE mission are meeting the mission requirements and are very encouraging for the future of astrophysics with Cubesats.

It has to be noted that the BRITE satellites are the first Cubesats launched and operated with an astrophysical purpose (the observation of stars) as the prime objective. The BRITE constellation demonstrates that it is possible to achieve precise astrophysics objectives with very small satellites and for a limited cost. In addition, the problems encountered by the satellites of the constellation that are reported by the project teams [35] allow new projects to be able to anticipate certain issues. For instance, we can mention the problem of radiation which degrades the detector. The satellites of the constellation are operating in Low Earth Orbit (LEO) and thus are exposed to energetic protons and electrons trapped in the magnetosphere. These particles can cause damage to electronics, memory and CCD detectors. The degradation of the CCDs was a very important problem that required monitoring during the mission. The degradation of the instrument response was mitigated by implementing a chopping observing mode. In this mode, the instrument observes a certain portion of the sky and performs successive exposures while offsetting the telescope pointing back and forth. Then, the two offset frames are subtracted and

the result is an image with one positive and one negative target image and the background defects are mostly removed [35].

### 3.2.2 CXBN-2

Cosmic X-ray Background Nanosatellite-2, CXBN-2, is a two unit (2U, 10 × 10 × 20 cm) Cubesat mission that was developed by the Space Science Center at Morehead State University. It was launched in April 2017 and it is the direct successor of the CXBN mission that was launched in 2012 as a secondary payload on the NASA ELaNa VI OUTSat mission [37][38]. CXBN-2 is still functioning and its goal is to significantly improve the precision of the scientific measurements done by CXBN. It has to be noted that the CXBN mission suffered from an anomalous low power mode that prevented the satellite to transfer sufficiently large amount of scientific data to the ground station. The mission was therefore not able to fulfil all its objectives [37].

The scientific purpose of the mission is the measurement of the Cosmic X-ray Background in the 30-50 keV range of photons energy and with a precision better than 5%. These measurements are necessary for constraining models that attempt to explain the relative contribution of X-ray sources in the extragalactic medium [37]. For making these observations, the satellite embarks a set of two Cadmium Zinc Telluride (CZT) detectors. It is a type of semiconductor detector which is very efficient for hard X-rays and soft gamma-rays detection.

Except for the payload of CXBN-2, all the major sub-systems of the satellite have flight heritage: they have been developed by teams of other missions or by industrials and have flown on the first CXBN mission. On the other hand, the payload is an evolved and improved version of the CXBN mission. Figure 3.3 shows the CXBN-2 satellite flight model integrated and ready for launch at the facility of the Space Science Center at Morehead State University. The payload of the satellite, composed of the CZT detectors, is integrated in the top unit where we also see a deployable antenna at the top of it. The sub-systems and the deployable solar panels are integrated in the bottom unit.

As for the CCD detectors of the BRITE constellation, the CZT detectors are more efficient if they are cooled. Deployable radiators were considered as the best solution for evacuating the heat generated by the CZT assemblies. However, the thermal analyses revealed that the design of the radiators needed to cool the detectors made the satellite sub-systems too cold for operations during the eclipse phases [38]. Therefore, a pouch made of a phase changing material was considered in order to provide smoother temperature changes in orbit transition to and from eclipse. Since the phase changing material that could be used for the application was a toxic material, this solution was subsequently discarded because the satellite was designed to be deployed from the International Space Station. The final solution for the thermal regulation was simple: to cover the surfaces of the outer panels with a layer of paint that allows the most efficient evacuation of heat by radiation to the cold space [38].

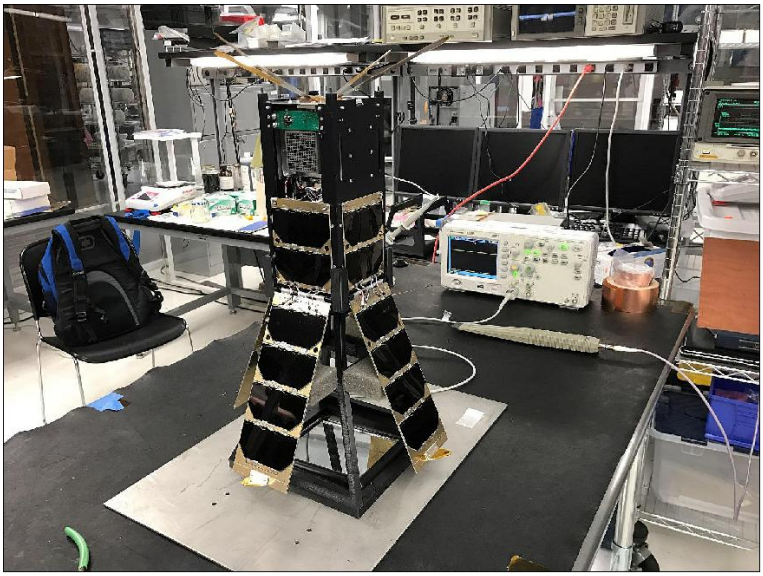

Figure 3.3: Picture of the CXBN-2 flight model in the Spacecraft Integration and Assembly facility of the Space Science Center at Morehead State University [37].

#### 3.2.2.1 ASTERIA

ASTERIA stands for Arcsecond Space Telescope Enabling Research in Astrophysics. It is a six unit (6U, 10 × 20 × 30 cm) Cubesat developed by the Jet Propulsion Laboratory (JPL). It was deployed from the ISS on 20 November 2017. Figure 3.4 shows an overview of the satellite in laboratory. ASTERIA is a project of technology demonstration of very precise astrophysical measurements using a Cubesat. The main challenges of the mission are to achieve arcsecond-level line-of-sight pointing error and highly stable focal plane temperature control in order to do precision photometry for studying stellar activity and transiting exoplanets [39]. At the beginning of the project, the mission/satellite was called ExoplanetSat and it was supposed to be a three unit Cubesat (3U, 10 × 10 × 30 cm) [40].

The payload of the satellite (Figure 3.5) is a telescope made of lenses and a baffle assembly. At the end of the instrument, a Complementary Metal Oxide Semi-conductor (CMOS) imager is mounted on a two-axis piezoelectric positioning stage [40].

The pointing which is required for achieving the science goals of the mission is extremely challenging. Indeed, the current attitude control systems that are available for Cubesats do not provide accuracies better than 20 arcsec approximately. This is 20 times larger than the requirement of ASTERIA. These off-the-shelf systems are usually made of several reaction wheels and one or two star trackers. Because of this lack of pointing accuracy, the ASTERIA team had to design a customized attitude control system for the mission. They integrated an off-the-shelf attitude control system for coarse pointing and the fine pointing control is achieved by tracking a set of guide stars on the CMOS sensor and moving the piezoelectric stage to compensate

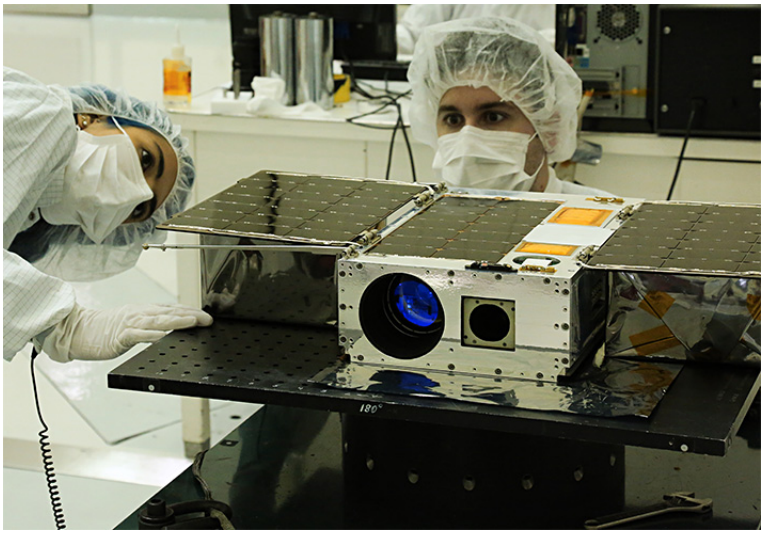

Figure 3.4: The ASTERIA satellite being integrated and tested in the laboratory before its launch and commissioning [39].

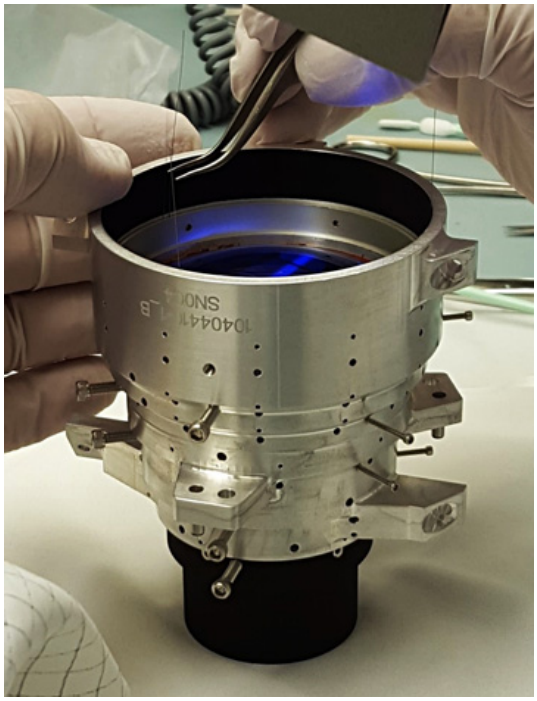

Figure 3.5: The ASTERIA telescope optics being integrated and aligned in the laboratory [39].

for residual errors. This way, the light of an observed star will always illuminate the same pixel or set of pixels during an integration, improving the photometric performance of the telescope.

### 3.2.3 PicSaT

PicSat is a three unit (3U, 10 × 10 × 30 cm) Cubesat developed by a small team of the LESIA group at Paris Observatory. The PicSat satellite was designed and tested the last few years and it was eventually launched in January 2018. The goal of this mission was to observe the transit of the exoplanet Beta Pictoris b in front of its bright star Beta Pictoris [41]. After 10 weeks of operation, the communication with the satellite was lost in March 2018 and after several attempts to re-establish contact, the PicSat team decided to call mission-closed in early April 2018 [42].

The scientific objective of the PicSat mission required to perform high-precision photometry in the visible part of the spectrum. Moreover, the mission had also the technical objective to demonstrate the feasibility of injecting star light into a single mode optical fiber with a Cubesat in space. Therefore, the payload which was designed and build is a fibered photometer in which the usual two dimensional detector is replaced by a single pixel avalanche diode [41].

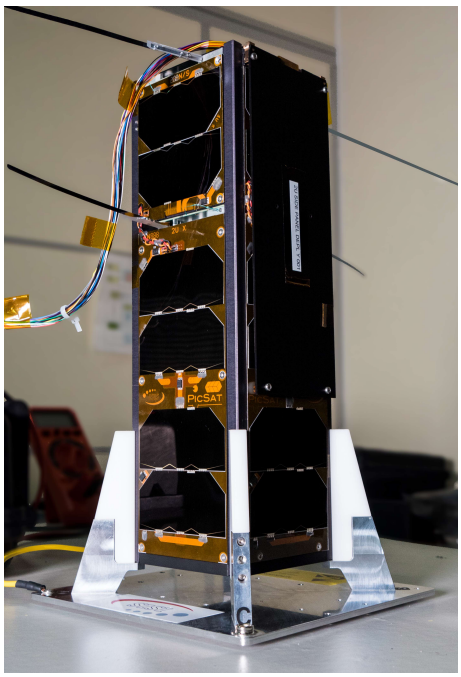


Figure 3.6: The PicSat satellite after integration and qualification at the Paris Observatory [42].

Figure 3.6 shows the PicSat satellite flight model integrated at the Paris Observatory. The satellite is divided in three dedicated units [42]:

- **Top unit**: it embarks the telescope composed of two mirrors and the star tracker. The primary mirror of the telescope has a diameter of 5 cm and the secondary mirror focus the light towards the focal plane where the fiber of 3 $\mu$m diameter is placed. The fiber is supported by a piezoelectric actuator that can correct its position.

- **Middle unit**: it contains the photodiode which is connected to the optical fiber and the payload electronics.
- **Lower unit**: it contains the antennas, the communication and navigation systems, the attitude control system and the power unit.

#### 3.2.3.1 HaloSat: a mission under development

HaloSat is the last Cubesat mission selected by NASA in 2017 [34]. It will consist of a 6U Cubesat that will embark an X-ray payload to study the hot galactic halo by measuring X-ray emissions, between 400 eV and 2000 eV [43]. The development of the project started in 2016 at the University of Iowa, before the mission selection, and is supposed to last two years. Therefore the launch of the satellite is planned for 2018.

### 3.2.4 Perspectives

Although Cubesat missions designed for astrophysics are not so numerous, the previous missions presented in this chapter have proven that it is possible to achieve some niche scientific goals with small satellites. The visible part of the spectrum and the X-rays are already covered by instruments on-board Cubesats. It is proposed in the next chapters to broaden the coverage of the spectral domain by adding the UV.

Additional new missions like ASTERIA are even more complex. The perspectives of this latter mission are important. If it is successful, it will definitely demonstrate that Cubesats are very important for astrophysics because they offer very large possibilities for small costs.

Eventually, it is interesting to point that for the presented Cubesats, the design of the payloads themselves is not very complicated. They are composed of a small number of optical elements, they do not contain any mechanism or moving parts and they do not embark internal calibration systems. This is due to the inherent constraint of the platform size. Because of the small size of the satellite, the payload should be as compact as possible. However, the requirements, even for Cubesats, are getting higher and higher despite their constant size. The difficulty lies in the ingenuity of developing a simple, compact and efficient system, while associating it with subsystems that guarantee the proper functioning of the mission.

# Chapter 4

# Feasibility Study of a UV Photometer On-board a 3U Cubesat

Some parts of this chapter were published in the article *A 3U CubeSat to collect UV photometry of bright massive stars* from Desselle et al. in the Journal of Small Satellites (see Appendix C).

## 4.1 Proposed Instrument and Mission

The UV domain has a large diagnostic power for the study of massive stars as they have their spectral energy distribution peaking in the UV. Spectroscopy offers the highest scientific return as many chemical elements have strong resonance lines in this wavelength domain. However, high resolution spectroscopic missions require large aperture telescopes that can only be accommodated on medium or large space missions [44].

On the other hand, as demonstrated by the Optical Monitor instrument on-board XMM-Newton [45], sensitive UV photometry can be performed with much smaller telescopes. In particular, monitoring the photometric variations of stars has an important scientific return. This is true for space-borne photometry in general, as it overcomes the limitations due to variable atmospheric absorption and provides in some cases, long homogeneous time series of essentially un-interrupted photometric measurements. Such data are of course primordial for asteroseismology, where measuring the radial and non-radial pulsations of stars allows probing the physical conditions in their interiors [46]. In this discipline, an important problem, especially for massive stars, is the identification of pulsation modes. UV photometric time series are crucial to complement optical data in this respect.

The power of such data is however not restricted to asteroseismology. This is well illustrated by the intriguing CoRoT light curves of early-type stars in NGC 2244 [47], or by the detection of flaring activity and rotational modulation in magnetically active late-type stars with Kepler [48]. UV photometric monitoring is no

exception here.

In addition, accurate space-borne UV photometry also allows studying the development of disks around Be stars, as well as many phenomena linked to binary interactions (tidal deformations, eclipses...).

Therefore, the goal of this chapter is to demonstrate that a very small and non-expensive space mission is able to address these several science cases. This is why the Cubesat standard was considered at the beginning of the project. After some preliminary considerations, the three unit (3U, 10 × 10 × 30 cm) platform was selected as the smallest one which is able to satisfy the scientific requirements (Table 4.1) formulated by the GAPHE working group. A smaller platform would not allow designing a telescope sufficiently sensitive to meet the specifications while carrying the elements necessary for the operation of the satellite. In view of the numerous successful 3U Cubesat scientific missions such as CINEMA or EXOCUBE [49], we are confident that 1.5U volume is sufficient to accommodate the service module. The requirements are inspired by the Optical Monitor instrument on-board XMM-Newton [45], but scaled for the smaller telescope size. The aim of the telescope is to acquire photometric time series of bright, mainly massive, stars between 2500 and 3500 Å. A relatively wide Field of View (FoV) diameter of 1° is defined as a requirement in order to be able to observe several stars simultaneously in very specific cases and also to be able to perform differential photometry observation. Differential photometry consists in obtaining measurements of a principal target and one or several other targets with similar magnitudes for comparison. In the present context, differential photometry could notably help distinguishing genuine variations of a star from effects due e.g. to temperature changes of the detector. Such a mission has never been performed before since Cubesats are usually designed for Earth and atmosphere observations, cosmic rays detection or stellar observations in the visible domain [32]. Observing in the UV does not allow to use lenses like in already existing Cubesat payloads such as BRITE [9], hence the innovative character of the present project.

| Reference | Parameter | Requirement | Goal |
|---|---|---|---|
| 3U-1 | Spectral range | 2500-3500 Å | 2500-3500 Å |
| 3U-2 | Angular resolution | 15 arcsec | 10 arcsec |
| 3U-3 | Field of view (diameter) | 1° | 2° |
| 3U-4 | Target magnitudes | V≤4 | V≤5 |
| 3U-5 | Photometric accuracy | 0.001 mag | 0.0005 mag |
| 3U-6 | Typical exposure time | 5 min | 1 min |
| 3U-7 | Mission duration | 2 years | 4 years |
| 3U-8 | Duty cycle | 60% | 75% |

Table 4.1: Scientific requirements for the proposed near-UV telescope.

## 4.2 Optical Design

The optical design has been optimized using the *CODE V* software from *Synopsis*. The ASAP software from Breault Research has been used for additional analyses such as stray light analysis (Section 4.2.2.5).

### 4.2.1 Basic Considerations and Constraints

#### 4.2.1.1 Volume Constraints

Since the transmission of lenses is very poor in the UV, reflecting optics must be used instead. The baseline design is a Ritchey-Chrétien telescope composed of two reflective hyperbolic mirrors. This kind of telescope has several advantages such as a high optical performance with only two reflective surfaces as well as a large aperture and effective collecting area for a given size of the telescope.

A preliminary research about off-the-shelf components for Cubesats revealed that half of a three-units is needed for vital sub-units. The payload was thus constrained to fit into the remaining 1.5 units. On the other hand, the optical axis is oriented along the direction of the Cubesat body length to benefit from a large focal length (Section 4.2.1.3). It has to be noted that a smaller platform (1U or 2U) cannot be used for the design of the scientific mission. It simply does not allow to design a photometer reaching the requirements and simultaneously having a fully operational satellite. A larger platform cannot be justified either because it would leave too much space in the satellite. This additional space could be used for other sub-units or to slightly increase the quality of the payload but it is not required and thus not necessary.

The entrance pupil diameter is fixed at 90 mm. This value is very close to the maximum dimension that can be accommodated within a Cubesat. A larger value could cause problems to fix the secondary mirror and also introduces vignetting problems because of the internal Cubesat structure.

#### 4.2.1.2 Field of View

Requirement *3U-3* specifies a FoV diameter of 1° and the goal value is fixed at 2°. During the optimization process, it appeared that the wider FoV of 2° was too large considering the optical performances needed and the volume constraint. A larger telescope is required for reaching this FoV goal, hence a larger Cubesat. In the meantime, it is entirely possible to obtain a very good optical quality over the smaller FoV of 1°.

Usual off-the-shelf scientific detectors have squared effective areas. Therefore, the FoV that will be imaged by the instrument should be larger than the effective 1° FoV because it is defined as a FoV diameter and not a diagonal (Figure 4.1).

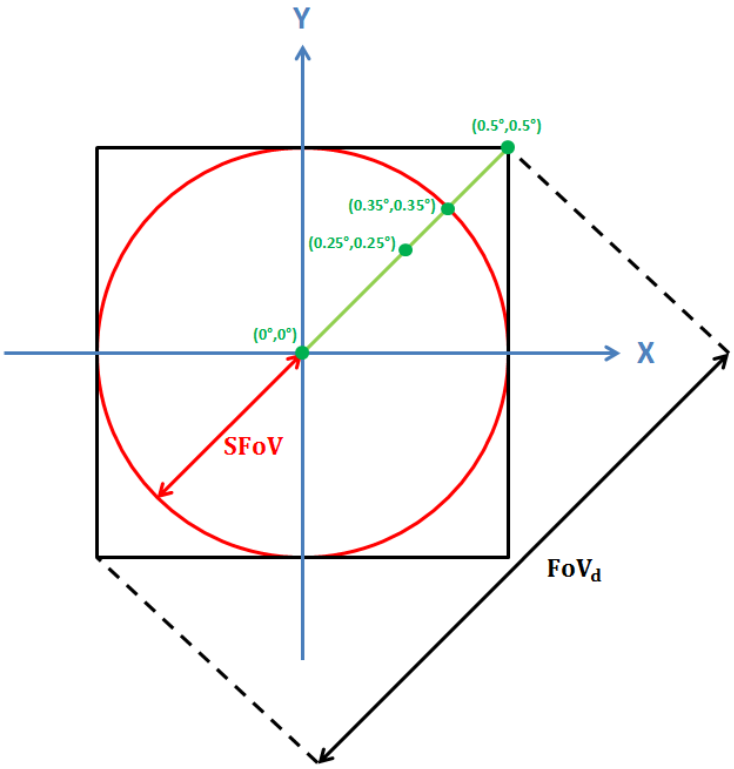


Figure 4.1: Field positions over a squared focal plane. The red circle shows the effective FoV specified by *3U-3*. The black square represents the overall focal plane of the instrument where the corners are outside the scientific areas.

As the Ritchey-Chrétien telescope is axisymmetric, the optimization of the system along only one dimension is sufficient. The points represented in Figure 4.1 are the ones defined for the optimization process in CODE V. Table 4.2 summarizes these points and their associated weight in the software. Point 4 has a lower weight because it is not in the scientific part of the focal plane. However, it is part of the image and it is better to avoid a large degradation of the optical quality at the corners and this is why its weight is non-zero.

| Point Number | X Coordinate | Y Coordinate | Weight |
|---|---|---|---|
| 1 | 0° | 0° | 1 |
| 2 | 0.25° | 0.25° | 1 |
| 3 | 0.35° | 0.35° | 1 |
| 4 | 0.5° | 0.5° | 0.5 |

Table 4.2: Points defined in CODE V for the optimization of the optical design and their associated weight.

#### 4.2.1.3 Effective Focal Length

The effective focal length is defined by Equation 4.1 [50][51] where $\Delta x$ corresponds to the half-width at half-maximum of the *Point Spread Function* (PSF) of the telescope in the focal plane and $\Delta\theta$ corresponds to the angular resolution of the system which is specified by *3U-2*.

$$f_{eff} = \frac{\Delta x}{\tan \Delta\theta} \tag{4.1}$$

At this point, the only known parameter of the equation is $\Delta\theta$ that must be lower or equal to 15 arcsec. For $\Delta x$, several possibilities exist, depending on the number of pixels that are associated to the PSF of the telescope since $\Delta x = \sqrt{\#Pix} * Pixel_{size}$ where $\#Pix$ is the number of pixels illuminated by the PSF and $Pixel_{size}$ is 13 to 26 $\mu m$ for off-the-shelf frame-transfer sensors from *e2v* [52] (anticipating the discussion relative to detector's technologies in Section 4.3.2).

As an example, Figure 4.2 shows $f_{eff}$ as a function of $\Delta\theta$ and $\#Pix$ considering a pixel size of 13 $\mu$m.

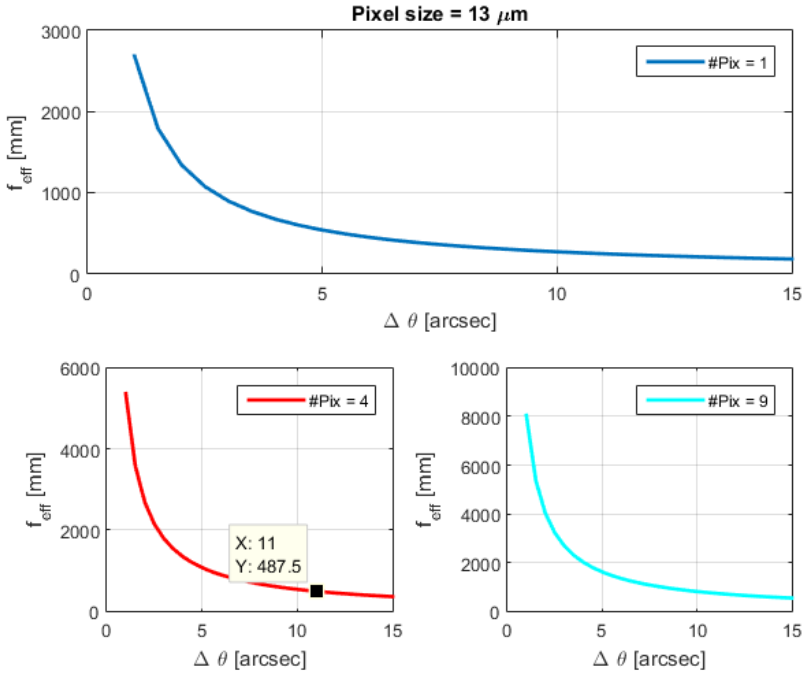


Figure 4.2: $f_{eff}$ as a function of $\Delta\theta$ and considering several values of $\#Pix$. The pixel size is fixed at 13 $\mu$m.

At first, $f_{eff}$ was left free in CODE V in order to catch a trend in the optical design considering only the volume and FoV constraints. It turned out very difficult to obtain reasonable design qualities (small spot sizes and high surface ratio

between secondary and primary mirrors) with $f_{eff}$ larger than 550 mm, hence this defines the maximum acceptable value for this parameter. Having a look at Figure 4.2, it is noted that for this size of pixels, $\Delta\theta$ will range between 10 and 15 arcsec, respectively the goal and the requirement of *3U-2*.

Anticipating the issue of pixels' saturation during scientific observations, it is better for the application to illuminate more than one pixel with the light coming from a target star and therefore $\#Pix = 1$ is to be avoided.

Eventually, in order to minimize the size of the detector focal plane for reducing mass and complexity, $\#Pix = 4$ and $Pixel_{size} = 13\mu m$ were selected over $\#Pix = 9$ and $Pixel_{size} = 26\mu m$, giving $\Delta x = 26\mu m$.

Several tests with CODE V have led to fix the value of $f_{eff} = 487.5\ mm$ which is the best compromise between the secondary/primary mirrors aperture ratio (see Section 4.2.2.1, $o = \frac{\phi_{secondary}}{\phi_{primary}} = 0.35$ leading to an obstruction factor of only $o^2 \approx 12\%$) and the angular resolution value $\Delta\theta = 11\ arcsec$, which is better than the requirement and close to the goal.

#### 4.2.1.4 Number of Pixels and Focal Plane Size

Knowing the angular resolution, the number and size of pixels illuminated by the PSF and the FoV diameter, the number of pixels in one direction needed for an acquisition and the minimum focal plane size are inferred (Equations 4.2 and 4.3).

$$\#Pixels = \frac{FoV}{\Delta\theta} * \sqrt{\#Pix} = \frac{3600"}{11"} * 2 = 654.54\ pixels \tag{4.2}$$

$$Plane_{size} = \#Pixels * Pixel_{size} = 654.54 * 13 * 10^{-3} = 8.50\ mm \tag{4.3}$$

Usually, for sensors, the number of pixels in one given direction is a power of 2 ($2^8 = 256$, $2^9 = 512$, $2^{10} = 1024$, etc...). This means that for imaging a complete scientific scene, the use of an off-the-shelf detector of $1024 \times 1024$ pixels detector is needed because the size just below is too small. It results in an imaging FoV diameter of $1.5644°$ (Figure 4.3). Since the telescope is only optimized for the effective scientific FoV and a baffle is designed to reject the light outside this FoV (Sections 4.2.2.4 and 4.2.2.5), the focal plane is composed of dead areas on the sides where the imaging quality and the amount of light reaching them is very low.

It is also conceivable to select a smaller detector (i.e. $512 \times 512$ pixels) but then the scientific FoV will be reduced to $0.7822°$ instead of the required value of $1°$. Whether this reduced FoV is acceptable or not needs to be assessed by the scientific working group. At this point, the baseline for the instrument design is still the required value of *3U-3* and the bigger detector is the baseline.

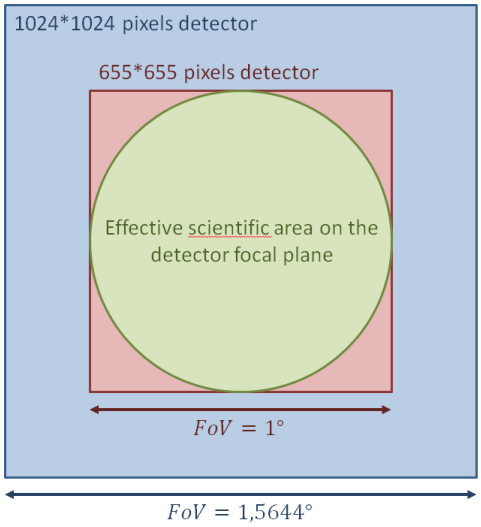


Figure 4.3: Schematic view of the detector focal plane. The green area is the effective scientific part for which the telescope is optimized. The red area represents the minimum square focal plane size calculated with Equation 4.2. The blue area is the entire focal plane size of a $1024 \times 1024$ pixels sensor.

#### 4.2.1.5 Filter

A filter should be integrated to the optical design to select the desired spectral range (requirement *3U-1*) and reject the other wavelengths. The filter, which is placed right before the focal plane in the optical design, has a small impact on the back focus of the design because of its refractive index. The scientific spectral domain is quite wide, ranging from 2500 to 3500 Å. It is relatively difficult to find off-the-shelf filters having such a large bandpass of 100 nm.

Figure 4.4 is representing the transmittances of the UG11 filter from Schott [53][54]. This filter has a very large bandpass which covers the scientific spectral domain of the instrument. However the curves show that the UG11 filter has non-negligible transmittances from 350 to 400 nm which are outside the spectral requirement. Using this filter requires a thorough calibration of the instrument for quantifying its behaviour with respect to the wavelength.

It has to be noted also that the filter has a non-zero transmittance in the visible/near infra-red around 700 nm. It is almost impossible to find a filter with a large effective bandpass which perfectly fits the spectral requirement. To get rid of these problems, it is necessary to consider using a filter specially made for the instrument but which will be more expensive than an off-the-shelf product.

#### 4.2.1.6 Conic Constants and Radii

The last constraints that were established to optimize the optical design are related to the conic constants and the radii of the two hyperbolic mirrors which

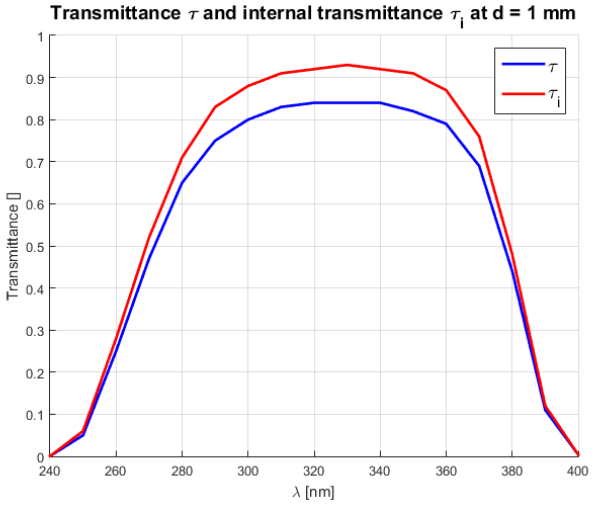


Figure 4.4: Transmittance $\tau$ and Internal Transmittance $\tau_i$ of the UG11 filter from Schott [53][54]. $\tau$ refers to the transmittance at the interfaces between the filter and its environment while $\tau_i$ is relative to the transmittance inside the filter.

compose the Ritchey-Chrétien telescope [51].

The radii must be negative in order to obtain right curvature sides in CODE V, i.e. a concave primary mirror and a convex secondary mirror. The conic constants range between -1 and -5 to ensure manufacturability of the surfaces [51].

### 4.2.2 Design Characteristics

#### 4.2.2.1 Geometry

The geometrical characteristics of the optimized optical design and extracted from CODE V are presented in Figure 4.5. As specified in Section 4.2.1.1, the entrance aperture has a 90 mm diameter. The effective diameter of the secondary mirror, M2, is equal to 29.2 mm. For deducing the obstruction due to M2, it is necessary to consider a larger diameter because of its supporting structure. Anticipating the mechanical design presented in Section 4.3, the diameter of M2 support is fixed at 33 mm, yielding an effective telescope diameter of $\phi_{eff} = \sqrt{90^2 - 33^2} = 83.73$ mm.

Figure 4.6 shows the 3D design of the telescope as it is optimized with CODE V. Figure 4.7 shows a 2D view of the telescope from CODE V (Figure 4.7a) and a cut view of the telescope as it is imported in Solidworks (Figure 4.7b) directly from CODE V. It can be seen from Figure 4.7b that the diameters of M1 and M2 are larger than presented in Figure 4.5. Indeed, edges are added to the mirrors for their mechanical accommodation to their structures in the spacecraft. Eventually, the central hole in M1 is also larger in Figure 4.7b than in other representations because the Solidworks model has already been modified to incorporate the baffling

| Surface # | Surface Name | Surface Type | Y Radius | Thickness | Glass | Refract Mode | Y Semi-Aperture |
|---|---|---|---|---|---|---|---|
| Object | Source | Sphere | Infinity | Infinity | | Refract | |
| Stop | Entrance Pupil | Sphere | Infinity | 103.0000 | | Refract | 45.0000 |
| 2 | M1 | Conic | -283.6496 V | -100.0000 V | | Reflect | 45.8747 |
| 3 | M2 | Conic | -117.9696 V | 140.0000 V | | Reflect | 14.6059 |
| 4 | Filter | Sphere | Infinity | 1.0000 | 'UV_FIL' | Refract | 7.0000 |
| 5 | | Sphere | Infinity | 3.0000 | | Refract | 6.0996 |
| Image | Focal Plane | Sphere | Infinity | 0.0000 | | Refract | 6.0406 |
| End Of Data | | | | | | | |

Figure 4.5: Snapshot of the Lens Data Manager related to the optimized telescope optical design from CODE V.

system that will be presented in Section 4.2.2.4.

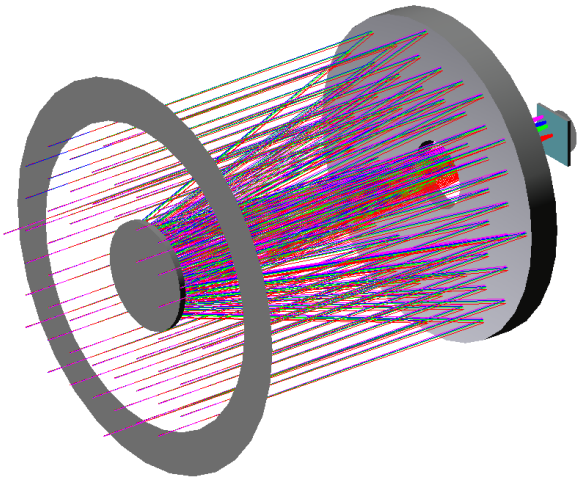

Figure 4.6: 3D Layout of the Ritchey-Chrétien Telescope.

#### 4.2.2.2 Spot Diagram

The spot diagram of a system is the image of a point-like object realized by the system. This is a highly useful analysis tool for checking whether the spot is for example well included in a given array of pixels.

Generally, the RMS spot diameter is used to measure the size of the image spot. This parameter corresponds to the diameter of a circle containing approximately 68% of the spot energy [55].

The spot diagrams for several off-axis positions are shown in Figure 4.8 where the squares are $26 \times 26$ $\mu m$ since the system is optimized to fit the spot onto 4 pixels of 13 $\mu m$ size. As it can be seen for off-axis angles inside the field specified in the scientific requirement (from (0°,0°) to (0.35°,0.35°)), the light is spread over the $2 \times 2$ pixel area expected to cover the PSF. The diameter of the spots (RMS or even 100%) are much smaller than the overall size of the $2 \times 2$ pixel area. This is no

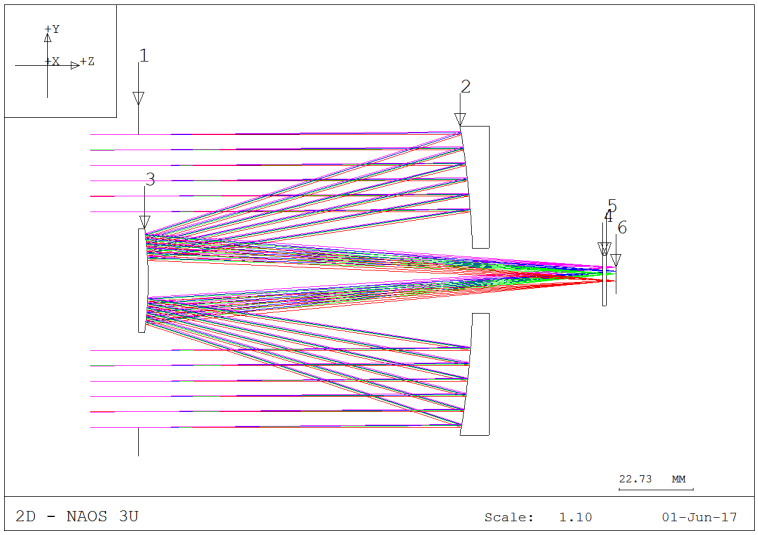


(a) 2D Layout extracted from CODE V with a ray-tracing representation.

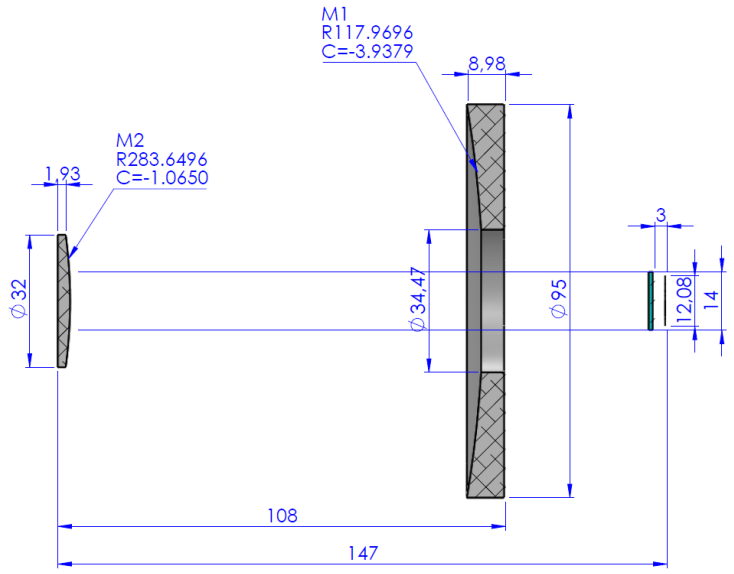


(b) 2D Layout and several measurements obtained with Solidworks

Figure 4.7: 2D Layout of the Ritchey-Chrétien Telescope.

more the case for large off-axis angles out of the scientific FoV but still illuminating the corners of the focal plane, i.e. (0.5°,0.5°). Of course, as it was discussed in Section 4.2.1.2, the instrument is not optimized for these corners and degradation of the spot sizes is expected. However, for off-axis angles out of the scientific FoV but close to it, i.e. (0.375°,0.375°), the RMS size is still smaller within the chosen $2 \times 2$ area and thus it is expected that the light from these angles will not pollute the other main FoV by spreading out their pixels. There is a central hole in the spots shown in 4.8. This hole is not visible for all the spots because of the figure resolution. It is simply due to the central obscuration by the secondary mirror at

the entrance of the telescope.

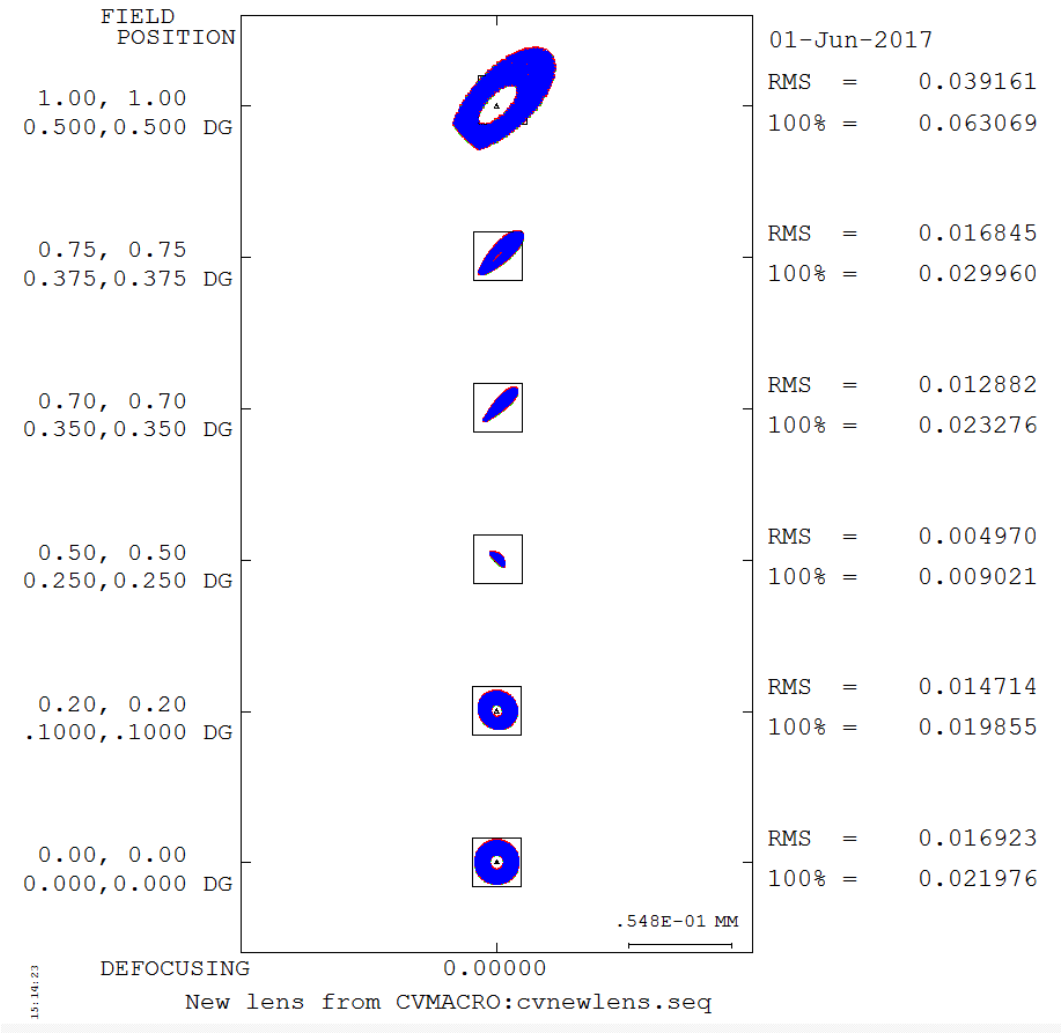


Figure 4.8: Spot diagrams of the designed telescope for squared areas of 26 $\mu$m side considering 6 off-axis angles ((0°,0°), (0.1°,0.1°), (0.25°,0.25°), (0.35°,0.35°), (0.375°,0.375°) and (0.5°,0.5°) from bottom to top).

Regarding the shapes of the spots, they appear to be quite uniform for small off-axis angles ((0°,0°) or (0.1°,0.1°) for example) but shapes degrade rapidly for larger off-axis angles where the spots are flattened along the radial direction in the focal plane. This is typical of astigmatism which is expected for a Ritchey-Chrétien configuration. This design may also suffer from field curvature aberrations [50]. Figure 4.9 shows the third order aberrations encountered at the focal plane. Astigmatism indeed accounts for the largest contribution to the system aberrations. Field curvature is the second highest contribution. Other aberrations (spherical, coma, distortion and chromatic) are negligible compared to astigmatism and field curvature, as expected for this kind of telescope. This degradation of the PSF uniformity has implications on the data reduction, although observations of fields with several

bright stars falling into the FoV of the instrument will be the exception rather than the rule. Thus the degradation of the spot uniformity for large off-axis angles is not considered to be an issue.

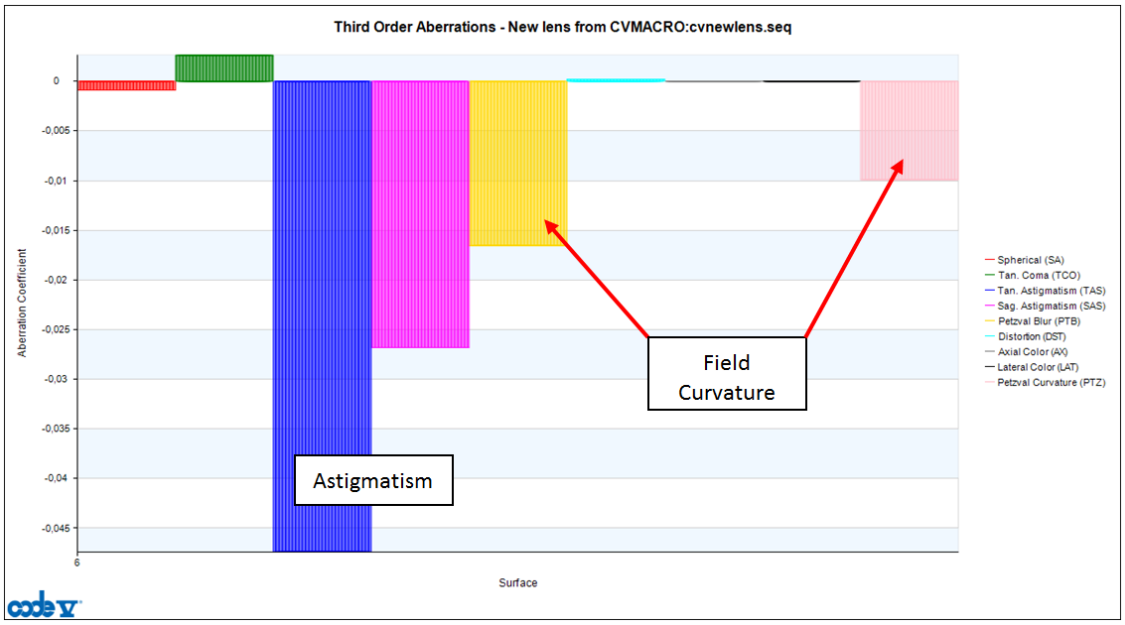


Figure 4.9: Third order aberrations of the telescope at the focal plane. The main contributions are from the astigmatism (blue and purple) and the field curvature (yellow and pink).

#### 4.2.2.3 Modulation Transfer Function (MTF)

The MTF measures the ability of an optical system to transfer the intensity modulation of an object (a star for example) to the image. Due to aberrations, diffraction and other disturbing effects, the contrast in the image is not the same as in the object. This means that the dark parts are not as dark and the bright ones are not as bright as in the original pattern [55].

In order to define the MTF, it is necessary first to define the image modulation:

$$Modulation = \frac{I_{max} - I_{min}}{I_{max} + I_{min}} \tag{4.4}$$

This definition is illustrated in Figure 4.10 from [55] where a simple periodic object is considered with an intensity that varies sinusoidally. When imaged by the optical system, aberrations and other disturbing effects induce a loss of contrast since the highest and lowest intensities have respectively decreased and increased.

Now, as presented above, the MTF is the ratio of the modulation in the image by the one in the object. The MTF is expressed as a function of spatial frequency which

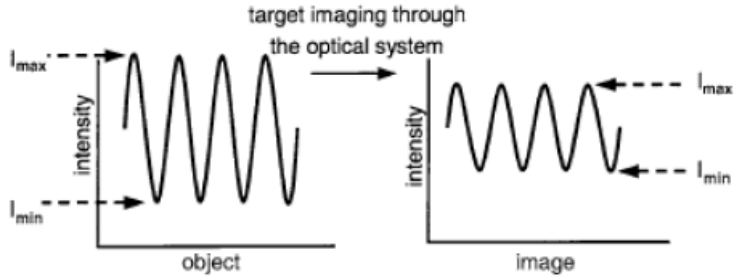


Figure 4.10: Modulation of intensity: object versus image [55]

is generally in the form of line pairs per millimeter. It thus expresses the transfer by the optical system of modulation from the object to the image as a function of spatial frequency.

Figure 4.11 illustrates the MTF of the telescope that CODE V produces for the off-axis angles used in the optimization process. These MTF only take into account the optical system (no detector or jitter contributions). It can be seen that the MTF degrades faster for the central field (0°,0°) than for other off-axis angles. This can be understood while looking at the spots of Figure 4.8 and especially the RMS sizes of the spots. The off-axis spots have smaller RMS sizes and therefore the contrast associated to them is better.

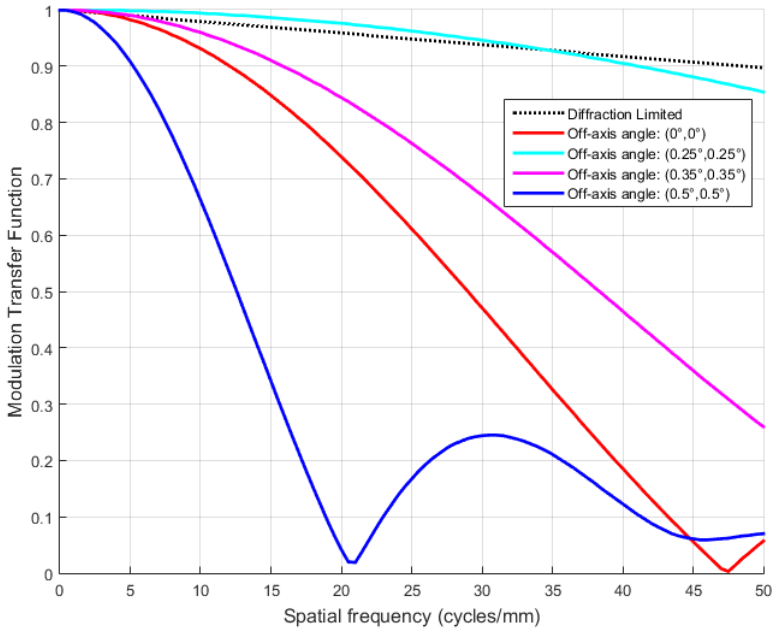


Figure 4.11: MTF of the telescope for several off-axis angles.

Therefore, to obtain a better quantification of the MTF, the first contribution

to add to the computation is the detector's contribution. Indeed, the sensor is composed of geometrical apertures (the pixels) that influence the MTF shapes. The final MTF is the product of the optical MTF (Figure 4.11) and the sensor's MTF. Two effects can be mentioned at this stage:

- The MTF is degraded by the detector;
- The range of spatial frequencies that can be represented is limited to values below the Nyquist frequency $\nu_{Nyquist}$. This frequency is expressed as $\nu_{Nyquist} = \frac{1}{2p}$ where $p$ is the size of two pixels because the PSF is spread over an area of $2 \times 2$ pixels, hence $p = 26\ \mu m$. This is the maximum spatial frequency that can be seen by the detector: $\nu_{Nyquist} = 19.23\ line\ pairs/mm$.

The detector MTF can be assimilated to the Fourier transform of a 26 $\mu$m square aperture:

$$MTF_{detector}(f) = sinc(pf) = \frac{\sin(\pi pf)}{\pi pf} \tag{4.5}$$

Considering the lowest MTF which is inside the scientific FoV (off-axis angle (0°,0°)), it is then possible to convolve it with the detector's MTF, leading to Figure 4.12. It can be seen that the MTF of the telescope associated to the detector drops from 75% to 48% at the Nyquist frequency. Since there is no requirement with respect to the MTF value at the Nyquist frequency, it is not possible to establish whether this result is compliant or not. However, a reasonable standard is to take a MTF above 10% [55], which is then in accordance with the result.

Another source of image degradation is the jitter. The jitter stems from the Line-of-Sight (LoS) movements due to vibrations inside the spacecraft structure. These vibrations induce an image blurring that must be controlled in order to get images satisfying the required optical quality. One way to study its impact is to implement a jitter MTF, and to convolve it with the previous one (telescope and detector).

Although different sources of vibrations exist, they can all be taken into account within a single equation. Equation 4.6 is presenting the jitter MTF where $\sigma^2$ is the LoS jitter variance from all sources (often expressed in $\mu$rad).

$$MTF_{jitter}(f) = e^{-2\pi^2\sigma^2 f^2} \tag{4.6}$$

Jitter noise measures are actually needed to obtain a value for $\sigma^2$. In the framework of this project, no direct measurements are available. Therefore several values of $\sigma^2$ have been considered in order to know for which value the MTF will drop to 10%. This is represented in Figure 4.13. It can be seen that the MTF drops to $\approx$ 10% when the jitter is equal to 40 arcsec (200 $\mu$rad). This limit of LoS jitter

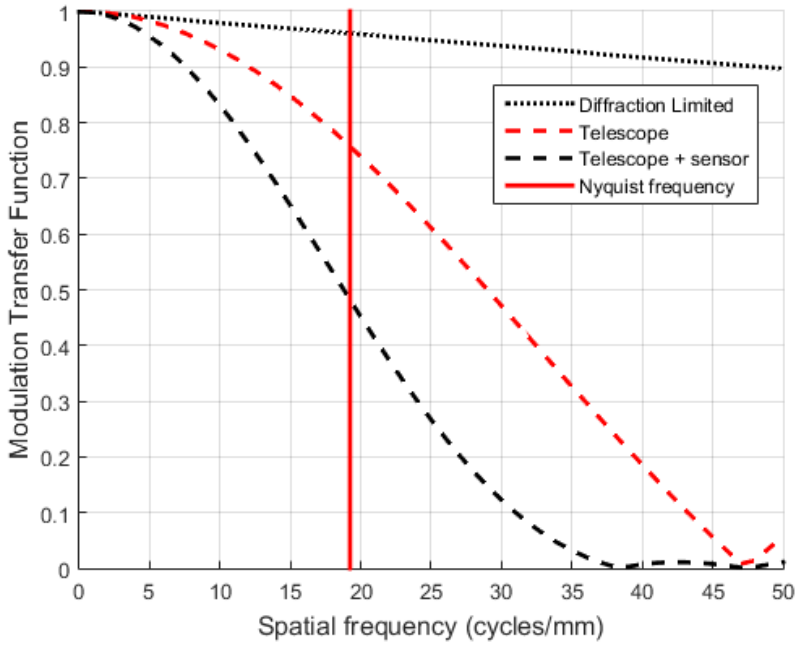


Figure 4.12: MTF of the telescope for an off-axis angle of (0°,0°) associated to the detector's MTF.

variance will be discussed in Section 4.3.4 because it defines a requirement on the attitude determination and control system (ADCS) that must be taken into account.

#### 4.2.2.4 Baffling System

As all other telescopes, the Ritchey-Chrétien design suffers from stray light (SL) when it is not protected by an optical baffle [55]. In the framework of this study, a baffling system based on a procedure described by Terebizh [56] has been designed to prevent SL from directions outside the FoV from reaching the focal plane. The system is based on two conic baffles, each associated to one mirror of the telescope, preventing direct light from any unwanted incident angle from reaching the detector.

Figure 4.14 is defining the geometrical configuration of the telescope and its cardinal rays paths. The baffles are defined by their edges $B_1$ and $B_2$ while the effective FoV is limited in the focal plane by the points $G$ and $G'$. Rays #2 and #3 are critically important for the system design because they are defining the points $B_1$ and $B_2$. Ray #2 touches the edge $S$ of the entrance pupil at an angle $w$ (semi-FoV) and therefore defines the light diameter of M1 (point $A$). It also defines the light diameters of M2 (point $L$) and of the focal plane (point $G$). Ray #3, which is at an angle $-w$, touches the edge $B_2$ of the baffle, defines the blind spots at the two mirrors (points $H_1$ and $H_2$) and terminates at the lowest image point $G'$.

Knowing the geometrical parameters of the telescope, it is safe to say that ray

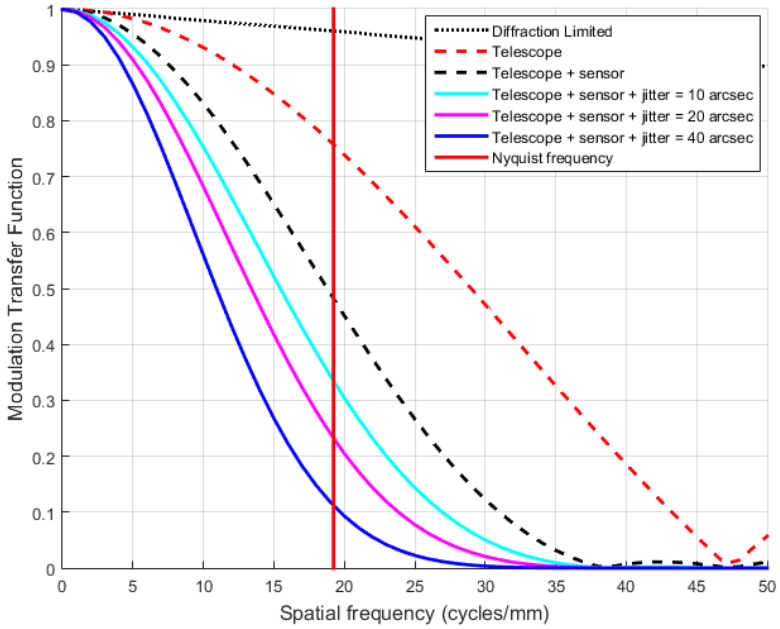


Figure 4.13: MTF of the telescope for an off-axis angle of (0°,0°) associated to the detector and jitter's MTF considering several values of $\sigma^2$.

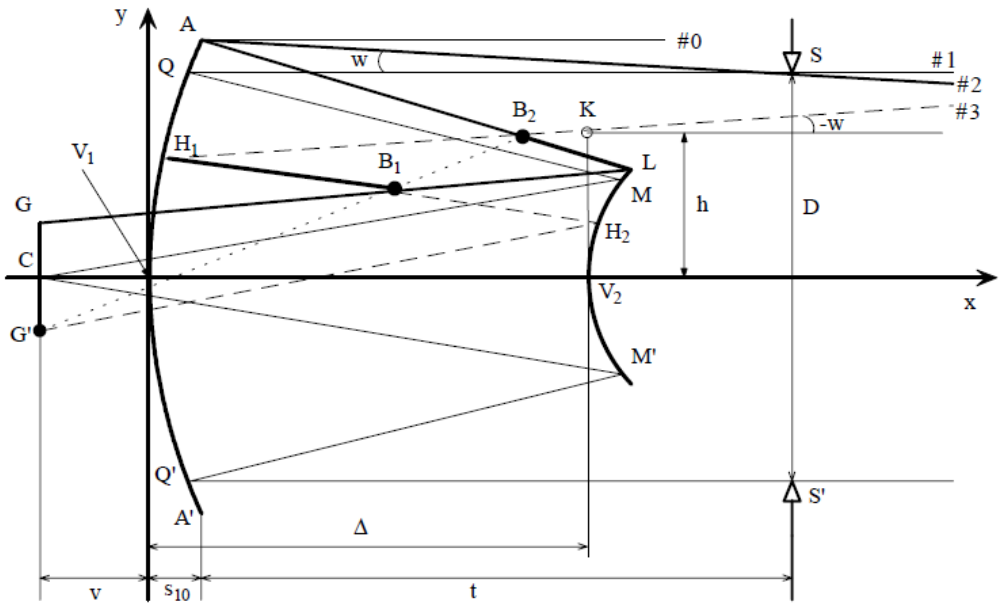


Figure 4.14: Paths of cardinal rays in a Ritchey-Chrétien telescope [56].

#2 is fully defined. The situation is different for ray #3 because the coordinates of the point $B_2$ are unknown. An additional requirement should be provided in order to optimize the baffle to reject SL and minimize the entrance obscuration. The solution proposed by Terebizh is the following: *The lowest field border and the highest*

*edge points of the baffles should lie on a straight line.* According to Figure 4.14, the straight line is $G'B_1B_2$. The free parameter of this optimization process is then the height $h$ which corresponds to the $Y$ coordinate of point $K$. It is directly linked to the height of the front baffle (point $B_2$ and ray #3).

For an arbitrarily chosen $h$, it is reasonable to assume that $G'B_1B_2$ will not be a straight line and to introduce a point $B_3$ which is aligned with $G'$ and $B_1$. The situation is more like the one of Figure 4.15. The goal is then to define $h$, i.e. the position of ray #3, in order to satisfy the additional condition that the quantity $\rho(h)$ which is mathematically expressed as in Equation 4.7 must be minimum. Here $(X_2, Y_2)$ and $(X_3, Y_3)$ are the coordinates of the point $B_2$ and $B_3$ respectively. The condition simply means that the two points must coincide to obtain the straight line $G'B_1B_2$.

$$\rho(h) = \sqrt{(X_3 - X_2)^2 + (Y_3 - Y_2)^2} \tag{4.7}$$

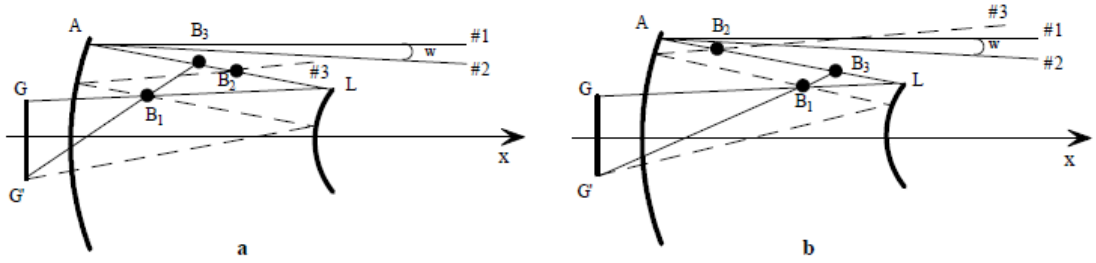


Figure 4.15: Two versions of the ray #3 path when points $B_2$ and $B_3$ do not coincide [56].

The way Equation 4.7 is computed is fully explained in [56]. The coordinates of the two points are computed in the $(X, Y)$ reference frame (Figure 4.14) knowing the equations of the mirrors and the rays. The computation of the merit function $\rho(h)$ for a series of height h is shown in Figure 4.16. $h$ varies from 16 mm ($\approx$ radius of M2) to 45 mm (radius of the telescope's entrance pupil). It can be seen that the minimum of the merit function, which is really close to zero, is encountered at $h \approx 19\ mm$. Knowing this parameter allows to compute the final coordinates of the points $B_1$ and $B_2$ and eventually to finalize the design of the optical baffle around the telescope.

Figure 4.17 shows a cut view of the baffling system integrated to the two mirrors of the telescope. The front baffle, associated to M2, will be mounted on the M2 support that is not represented in the figure and the rear baffle, associated to M1, will be composed of two pieces that will be fixed and positioned at the rear of M1 support. This configuration forces to re-assess the value of the effective diameter of the telescope because the central obscuration is now larger with the front baffle installed around M2: $\phi_{eff} = \sqrt{90^2 - (2 * h)^2} \approx 81.50\ mm$.

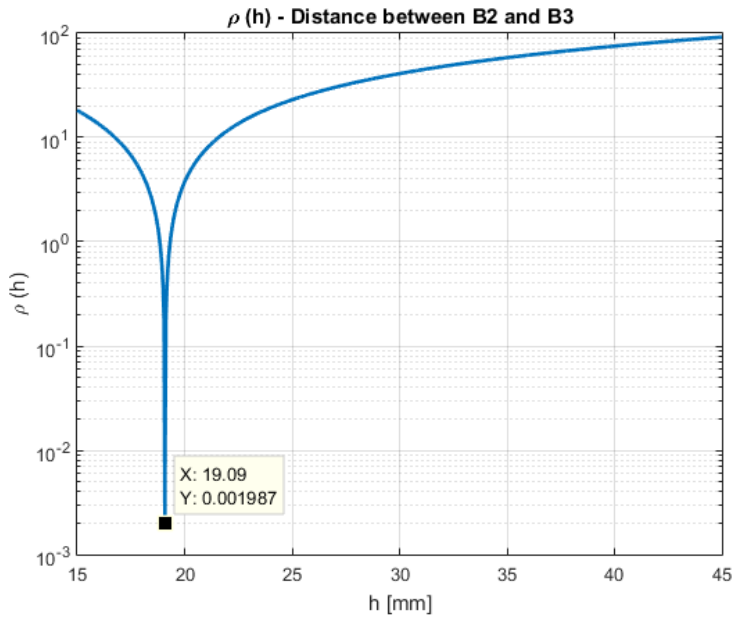


Figure 4.16: Merit function $\rho(h)$ for the design of an optimal baffle accommodated to the Ritchey-Chrétien telescope inside a 3U Cubesat.

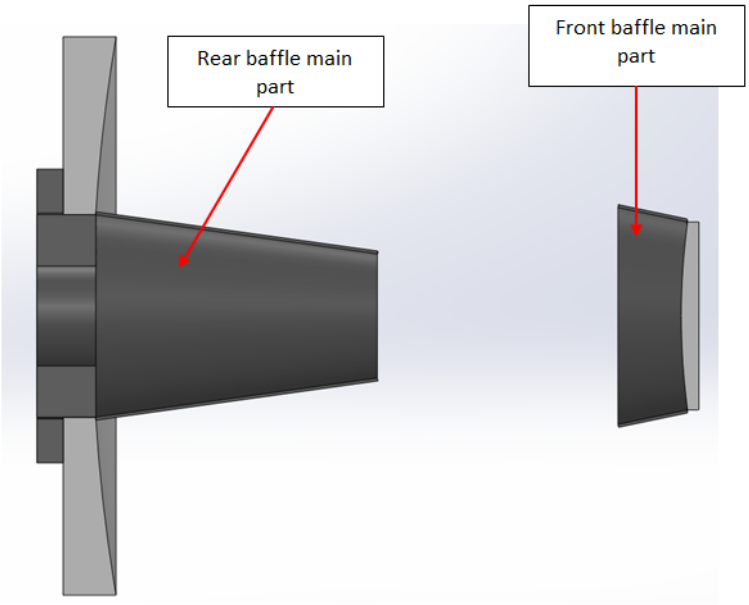


Figure 4.17: Cut view of the baffling system obtained from [56] and integrated to the optical design.

#### 4.2.2.5 Stray Light Analysis

Using the ASAP software, it is possible to quantify the relative amount of photons coming from off-axis angles of an entire sky hemisphere, entering the telescope and reaching the focal plane. This quantity was determined in the following way: a

light source covering a part or the entire focal plane is defined, and then it is assumed that this source emits light in one hemisphere in the direction of the secondary mirror. The light is then back-propagated through the telescope until it reaches the entrance pupil. Those photons are eventually sorted according to their incidence angle on the pupil to identify the off-axis fields reaching the detector since their propagation path is reversible. This method is commonly used since any simulation using the direct path cannot simulate an infinite set of FoVs.

First, it is interesting to analyse the impact of the baffle design described in Section 4.2.2.4. For this purpose, a perfect case is assumed where all the surfaces of the instrument inside the spacecraft are considered as fully absorbing, except for the mirrors of course. The entire focal plane is a light source and the light is back-propagated through the telescope. Figure 4.18 shows the relative amount of photons as a function of the fields of view that are successfully going through the telescope, with (Figure 4.18a) and without (Figure 4.18b) the baffles. In any case, all the directions that potentially produce a non-zero amount of photons are represented. It can be seen from Figure 4.18a that only the fields that must be imaged by the detector are going through the telescope, resulting on an image covering only $1.4° \times 1.4°$. The overall sensitivity appears very smooth and constant throughout the FoV imaged by a $1024 \times 1024$ pixels detector (see Section 4.2.1.4). It also can be seen that there are some dead points with very low intensities which are due to the fact that the number of photons/rays emitted in the software is not infinite. In contrast, Figure 4.18b shows an image of $20° \times 20°$ with large variations, demonstrating that light from large off-axis angles (up to $\pm 10°$) could reach the detector with very high relative intensity when the telescope is not protected by an optical baffle. The rings around the effective FoV are due to multiple reflections between M1 and M2.

In more realistic cases, the inner walls of the baffles and the spacecraft are coated with Chemglaze (black coating with very low reflectance [57]) even if they still induce some scattered reflections. The Harvey model is used for characterizing the reflections on the mirrors, more specially their scattering behaviour with respect to roughness. Figure 4.19 is presenting the results for this configuration the same way as Figure 4.18 except that here, the point of interest on the focal plane is only its central position and no more the overall detector. It is important for the quantification of the SL noise to focus the computation on specific areas of the focal plane to compare this noise to levels of scientific signal (see Section 4.5.4.2).

It can be seen from Figure 4.19 that the maximum is naturally reached on-axis since this corresponds to the direct geometrical path end position. However, scattered light from some other off-axis angles can reach these pixels too. Nevertheless, the relative intensity of these other angles are below 0.001% of the on-axis maximum level. When the noise from the entire hemisphere is integrated, assuming a uniform emission, it is found that for 1 effective photon from (0°,0°), there is 0.06 photon from the rest of the field: under this assumption the central position of the focal plane thus receives 94.3% of effective signal and 5.7% of noise from the sky background.

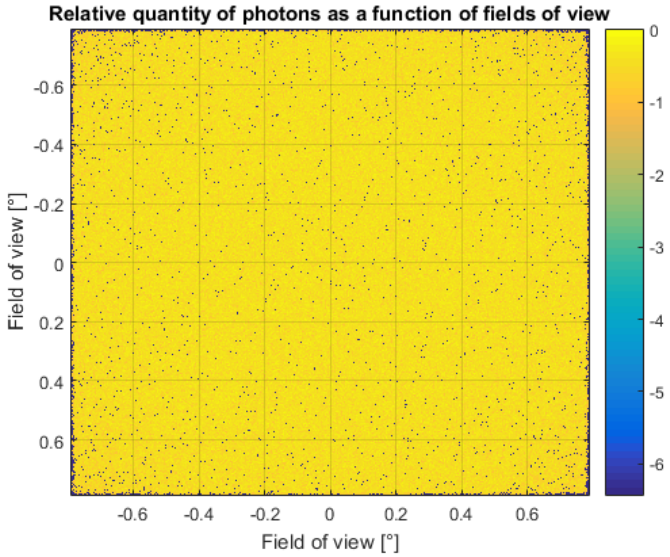


(a) With the baffles.

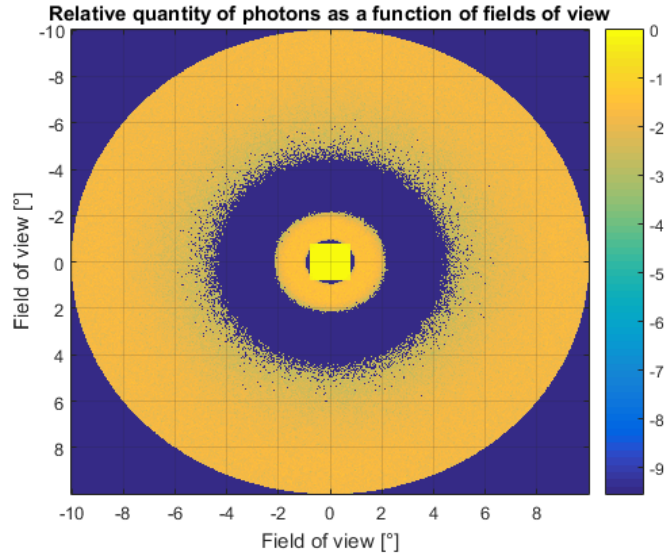


(b) Without the baffles.

Figure 4.18: Logarithm of the relative quantity of photons, passing through the instrument and reaching any part of the focal plane, as a function of the fields of view. These results are computed for the ideal case where the non-reflecting surfaces are fully absorbing.

To assess the effective level of stray light, the brightness of a sky hemisphere as it will be seen from space has to be evaluated. There are two main contributions: stellar and zodiacal light [58]. Using the results from [59] and [60], the estimated amount of light from these contributions at the entrance of the instrument is $N_{SL} = 8.73 * 10^7$ $photons/cm^2.s$ over the spectral domain covered by the telescope, i.e. 2500-3500 Å. This quantity is associated to an entire hemisphere of the sky. Since $N_{SL}$ is a substantial number, it seems reasonable to improve the

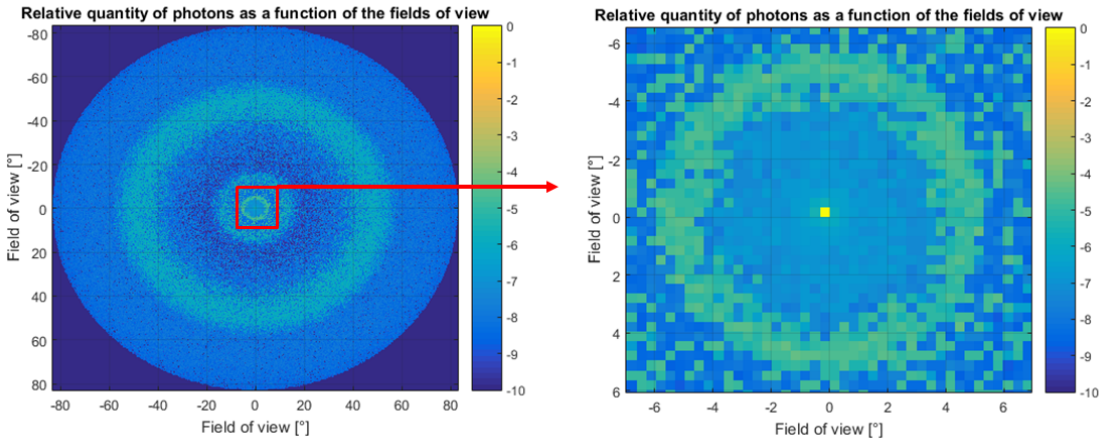


Figure 4.19: Logarithm of the relative quantity of photons, passing through the instrument and reaching the central position of the focal plane, as a function of the fields of view over an entire hemisphere of the sky, assuming a Chemglaze coating.

baffling system to further reduce the amount of SL.

To do so, it is possible to add some vanes inside the baffles of Section 4.2.2.4 and also to add a large baffle with vanes around the entire telescope in the spacecraft (main baffle in Figure 4.20). The vanes are placed in the baffles to block particular paths of SL which are important. This is done using ASAP to visualize the paths of non-negligible off-axis angles contributions. The new aspect of the system is shown in Figure 4.20.

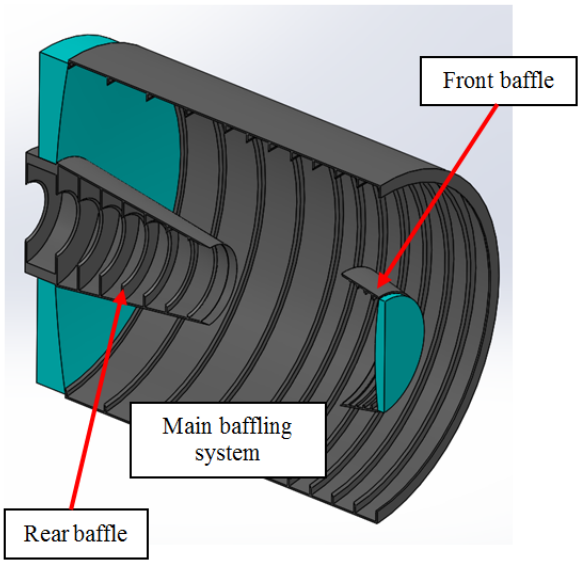


Figure 4.20: Cross-sectional view of the baffling system with the addition of a *main baffling system* and vanes inside the front and rear baffles.

Repeating the computation for the central position of the focal plane with the new baffle design, the obtained results are presented in Figure 4.21. Integrating the entire noise, it appears that the noise level is only 0.007 photon with the addition of the main baffle and the vanes (0.7%). Therefore the rejection of SL has been improved by an order of magnitude.

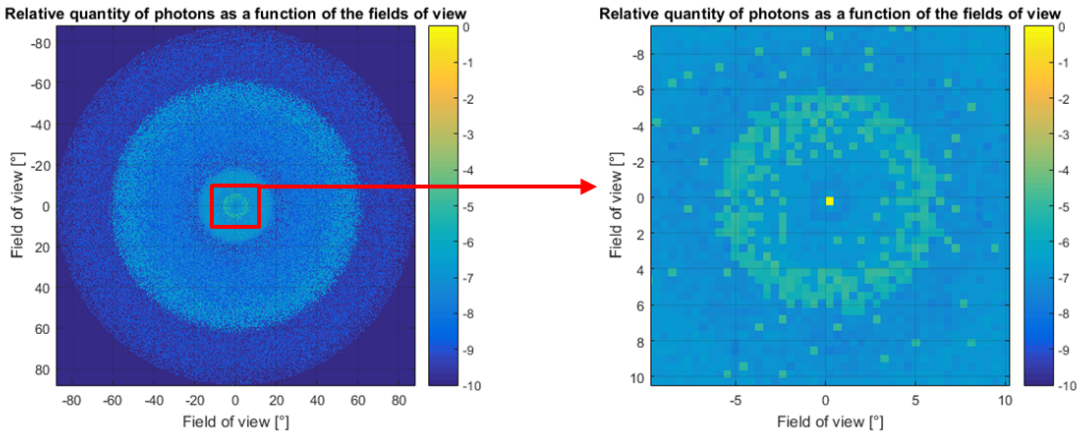


Figure 4.21: Same as Figure 4.19 with the baffle from Figure 4.20.

It is now impossible to further improve the rejection of SL without blocking paths of effective signal considering the design of the telescope and its integration inside the Cubesat. Another solution could be to integrate a deployable baffle that will be placed in front of the entrance pupil. However, the use of a deployable system introduces a very high complexity to the system in terms of design, power and reliability which is at odds with requirements of a Cubesat project.

## 4.3 System Overview

### 4.3.1 Solar Panels Configuration

#### 4.3.1.1 Table Configuration

Figure 4.22 shows the design of the 3U Cubesat with its solar panels in a table configuration. The z-axis of the CAD corresponds to the optical axis of the instrument. Figure 4.23 shows a cross-sectional side-view of this configuration, in the yz-axes plane. It can be seen that the payload fits into 1.5 unit as it was chosen. The other half of the spacecraft is dedicated to the sub-units needed to make the system work. The volumes of these units (including the Cubesat's structure and the solar panels) are simulated using computer-aided designs (CAD) of some components off-the-shelf (COTS) from several manufacturers.

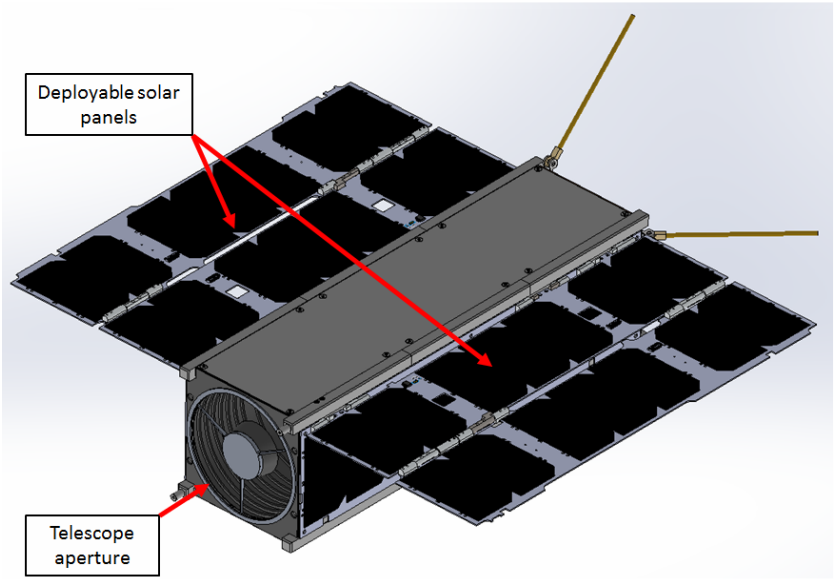


(a) View from the top.

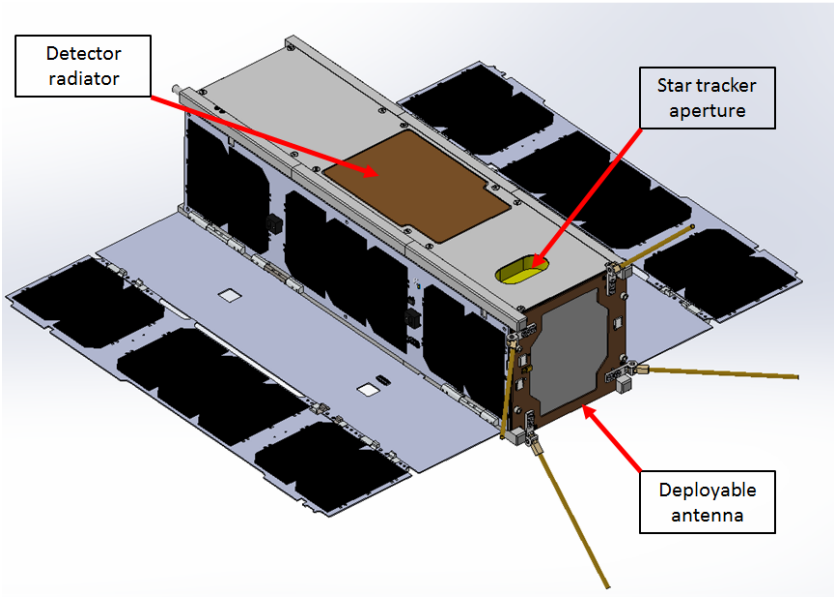


(b) View from the bottom.

Figure 4.22: Overview of the table configuration for the 3U Cubesat. The Cubesat structure CAD is from ISIS Space [61], the solar panels CAD are from Clyde Space [62] and the deployable antenna CAD is from GOMSpace [63].

#### 4.3.1.2 Cross Configuration

Figure 4.24 shows the design of the 3U Cubesat in the cross configuration. The antenna in this configuration is not the same as for the table configuration. Indeed, if we used the same deployable antenna as for the table configuration, it would be on the side of the solar panels and would thus face the Sun all the time during the mission. Such a configuration is clearly not recommended with respect to the thermal balance of the antenna and communication with the ground segment. This

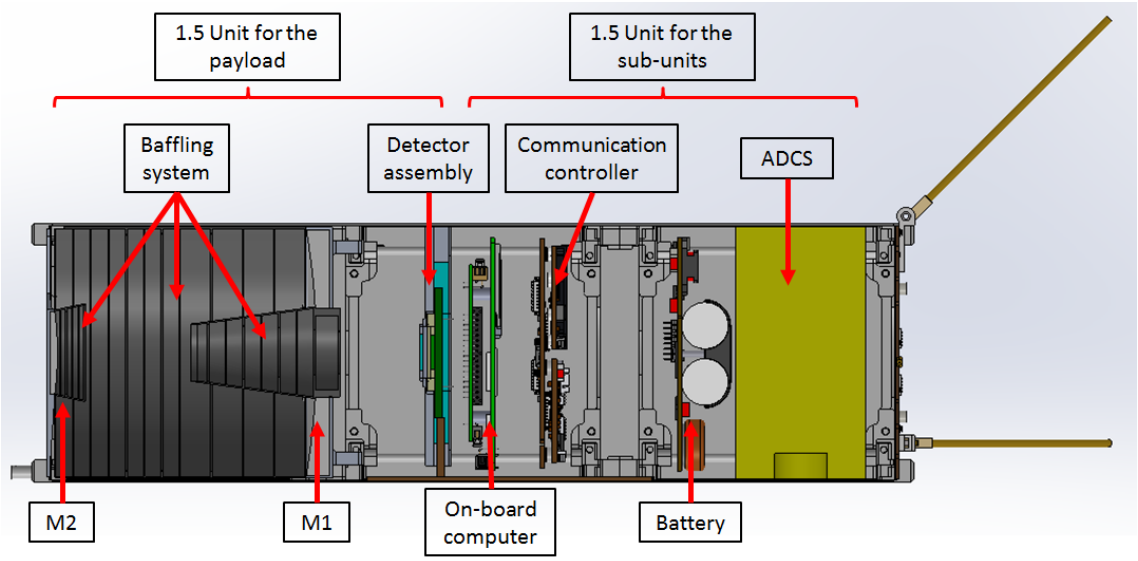


Figure 4.23: Cross-sectional side-view of the table configuration of the 3U Cubesat. From left to right: the secondary mirror and its baffle which are mounted on a support linked to the structure by three thin feet - the primary mirror and its baffle which are mounted on a support directly fixed to the structure - the detector assembly composed of the detector, an electronic card, a thermal insulation made of Permaglas, an aluminum structure and a radiator - the on-board computer (CAD from ISIS Space [61]) - the communication controller (CAD from GOMSpace [63]) - the battery (CAD from GOMSpace [63]) - the attitude determination and control system (volume from Blue Canyon Technologies [64])).

is why a patch antenna, positioned on one side of the spacecraft, is preferred for this configuration.

#### 4.3.1.3 Sky Visibility

It is important to consider the scientific needs (sky visibility) and the technical constraints (illumination of solar panels, Earth avoidance) in order to choose the most interesting configuration between the table and the cross.

Anticipating Section 4.4.1, a dusk-dawn Sun-synchronous orbit, at an altitude of 800 km and an initial right ascension of the ascending node (RAAN, see Section B.1) $\Omega_0 = 270°$, is assumed for the mission. The main technical constraints are the following for each satellite configuration (table or cross):

- The satellite needs a certain amount of electrical power. This implies that the solar panels must be turned towards the Sun or, at least, that the Sun light must reach the solar panels under an incidence angle not too far from $\frac{\pi}{2}$.
- The instrument cannot observe the Sun or the Earth and scattered light from the Sun and the Earth must be avoided. For the Sun, the angle between the

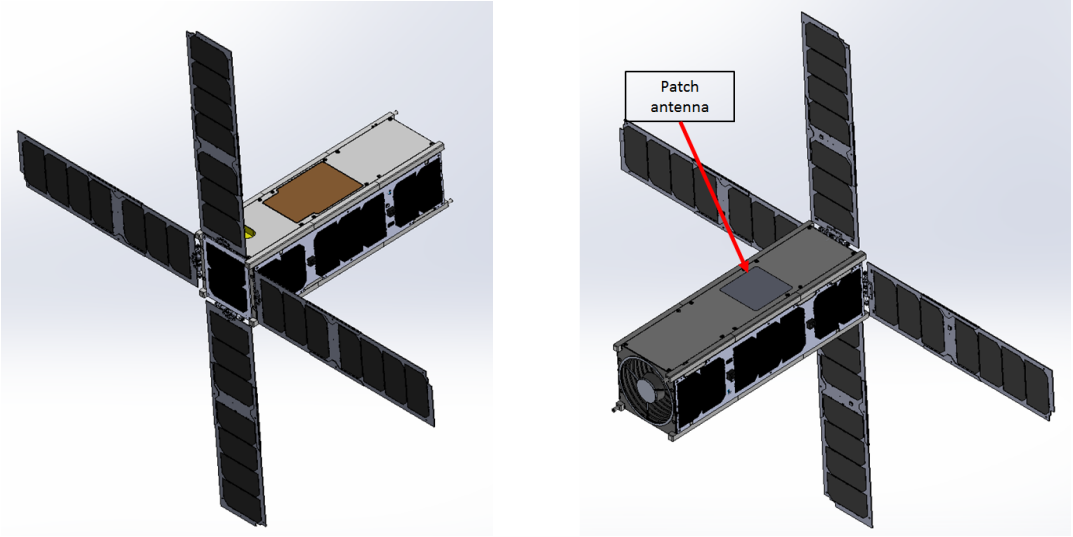


(a) View from detector's radiator side. (b) View from the patch antenna side.

Figure 4.24: Same as Figure 4.22 for the cross configuration.

entrance pupil plane normal and the Sun direction must be higher than $\frac{\pi}{2}$. This constrains the table configuration because of the panel's position w.r.t. the entrance pupil[1]. For the Earth, an avoidance angle has to be defined. Figure 4.25 illustrates the avoidance angle $\Delta$ and also $\theta = \arcsin \frac{R_{Earth}}{A} = \arcsin \frac{R_{Earth}}{R_{Earth} + a}$ where $a$ is the satellite's altitude. It is possible to define a cone of opening angle $\Delta + \theta$ around the direction towards the center of the Earth that cannot be observed.

- Eventually, the instrument's FoV should avoid the Moon except possibly for some calibration observations. The instrument is carrying a filter that only selects the near-UV spectral range where the incoming flux from the Moon is lower. However, the brightness of the Moon sets restrictions on the pointing direction to prevent any damage of the detector and to avoid excessive thermal load on the filter. This constraint is similar to the previous one and an avoidance angle should be defined knowing the position of the Moon in the sky at any given time.

These constraints limit the part of the sky that can be observed at any given time. The way the observable parts of the sky are limited is highly dependent of the solar panels configuration.

The first constraint relative to the electrical power can be translated in the problem of sky visibility by the definition of a power tolerance angle $\Psi$ such that the needed power at any given time is available i.e. $P_{needed} = P_{max} \cos \Psi$. The schematic

[1]It does not impact the cross configuration because the solar panels and the entrance pupil are located at opposite sides of the satellite. The condition is always met by definition of the system.

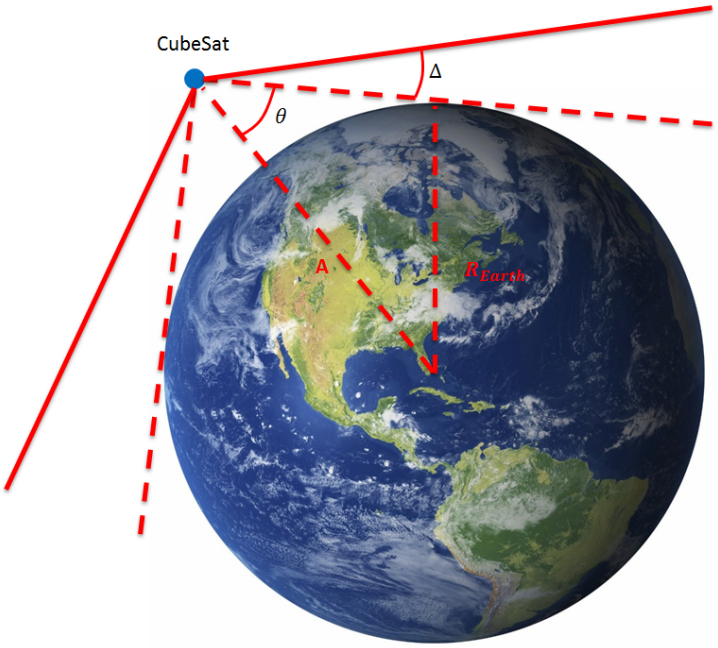


Figure 4.25: Schematic representation of the avoidance cone due the Earth.

representation of Ψ is shown in Figure 4.26. It has to be noted in Figure 4.26a that even if the $-\Psi$ angle is acceptable w.r.t. the power aspects, it is not considered because the scattered Sun light would become a major issue.

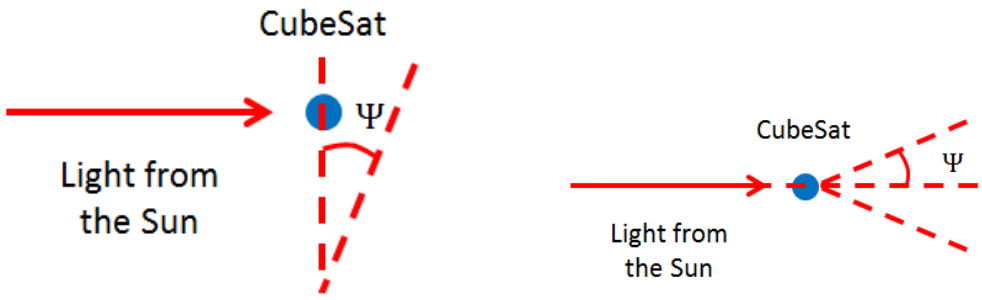


(a) Ψ for the table configuration.

(b) Ψ for the cross configuration.

Figure 4.26: Schematic representation of the power tolerance angle Ψ for the two solar panels configurations.

The visibility region defined by Ψ is then truncated by the intersections with the Earth avoidance zone. In order to define the region of the sky which is observable at any given time, the position of the Sun has to be known at any time. In a similar way, we need to know the position of the Moon. For this purpose, the ephemerides provided by the Institut de Mécanique Céleste et de Calcul des Ephémérides (IMCCE) were used. Eventually, the position of the satellite w.r.t. the Earth must be

defined in order to know the avoidance cone. At the end of these steps, the observable cone is derived. These computations have been made by G. Rauw, co-advisor of this PhD thesis, and are reported in [65] and in the next subsection.

#### 4.3.1.4 Comparison of the Configurations

The results of the sky visibility problem are presented in Figure 4.27 for the two panels configurations and with external conditions as similar as possible, i.e. same Earth and Moon avoidance angles and same power tolerance angle. The contours on the maps of Figure 4.27 represent several numbers of satellite revolutions with non-zero visibility. The number of revolution can be translated into a number of days. The maps cover the entire sky in equatorial coordinates (right ascension and declination). Therefore Figure 4.27 represents the parts of the sky which are accessible for observation with a given satellite configuration and it also quantifies how long these parts of the sky are accessible.

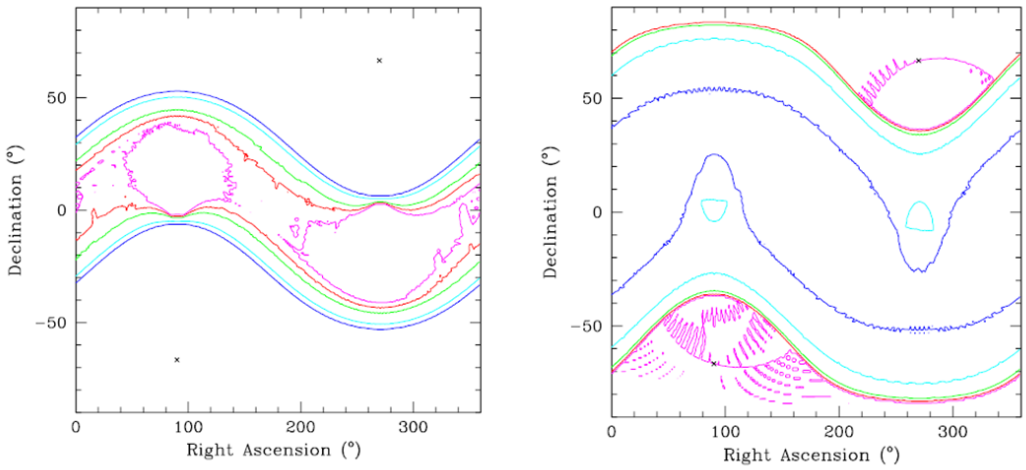


Figure 4.27: **Left:** sky visibility over the entire mission of two years with a putative launch on 1 January 2020 at 00h00 UT for a cross configuration of the solar panels and with $\Psi = 30°$, $\Delta = 15°$ and a Moon avoidance cone with 15° half opening angle. The map yields the number of spacecraft revolutions with non-zero visibility. **Right:** same but for the table configuration. In all panels, the contours correspond to 20% (blue), 50% (cyan), 80% (green) and 98% (magenta) of the maximum visibility of the corresponding panel. For the left panel, the maximum value is 477.3 spacecraft revolutions, which is equivalent to 33.1 days. For the right panel, the maximum value is 1531 spacecraft revolutions, which is equivalent to 106.3 days [65].

The left part of Figure 4.27 presents the results for the cross configuration. It clearly shows that the overall sky visibility of this configuration is very poor. Only regions relatively near the ecliptic can be observed and for a maximum duration of only about one month.

The right part of Figure 4.27 presents the same results for the table configuration. In this case, it is immediately obvious that the configuration offers a much better overall sky visibility than the previous one. The quasi-totality of the sky is now observable and the duration of accessibility is much higher. For example, the maximum visibility for the table configuration is three times higher than for the cross (106.3 days compared to 33.1 days).

Thanks to these calculations, it is easy to understand that from the scientific point of view, the table configuration is the best option because it gives access to a larger part of the sky and therefore a larger set of stars. For that reason, the table configuration is kept as the best candidate and therefore it is used for the thermal environment analysis that is presented in Section 4.4.

### 4.3.2 Detector Choice and Characteristics

#### 4.3.2.1 Back-Thinned CCD

A Charge Coupled Device (CCD) is a light sensitive silicon chip which is divided in a large number of pixels. The pixels are used to detect photons and accumulate the charges[2] before the reading of the entire array. The charges of each pixel are transferred to an analog-to-digital circuit that converts the signal. The output is a digital image consisting of a matrix associated to the pixel array. Each element of the matrix is a number related to the amount of light falling on the corresponding pixel. It is interesting at this point to list some parameters of the detectors [66]:

- The **Quantum Efficiency** (QE) of a light sensor is a crucial point for photometry. It characterizes the number of photons falling on a pixel that are actually detected. It is often expressed in percent and is wavelength dependent.
- The **dark current** is related to electrical charges generated in the device even if no light is entering the detector. It is due to the generation of electrons in the semi-conductor material and cannot be avoided because it is a natural phenomenon related to the temperature of the device.
- The **readout noise** is an electronic noise associated to the amplifiers used to convert the signal from the pixels to a digital image.

In a classical CCD sensor with a front illuminated structure, the pixels are placed at the back of a layer of Poly-Si electrodes. The Poly-Si electrodes absorb some percentage of incoming light and this absorption is wavelength-dependent. Especially, the UV light is blocked by this front layer and thus classical CCD sensors are absolutely not efficient for UV light detection. To overcome this disadvantage, in a back-thinned CCD structure, the CCD is turned upside down in order to place the

[2]The charges are created by the photoelectric effect. This effect is a phenomenon in which electrons are emitted from matter, particularly metals, when energy from an electromagnetic radiation (light) is absorbed.

pixels in front of the incoming light and the layer of Poly-Si electrodes are at the back of the pixels. The structure is also thinned to about ten microns in thickness. This second type of CCD structure is now very efficient for the UV light detection because the UV photons are no longer absorbed by the electrodes. The principles of these two structures of sensor are presented in Figure 4.28 [67].

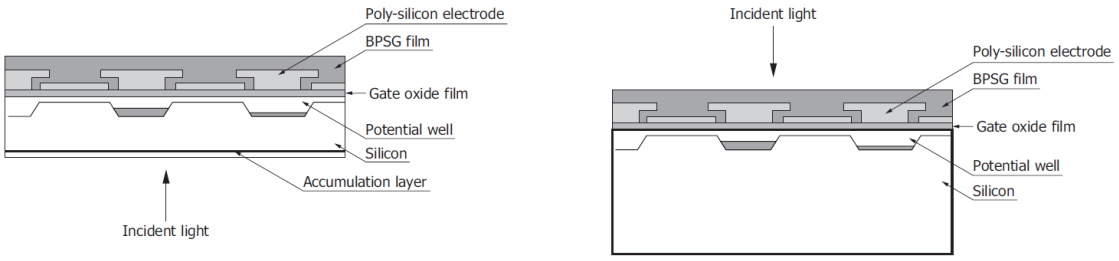


Figure 4.28: Schematic overview of the back-thinned (left) and normal (right) CCD structures principles [67].

However, as it is specified in [68], there appears a positive charge at the interface between the accumulation layer and the silicon that creates a potential well which traps photoelectrons at the CCD back surface. Due to the short absorption length of UV photons in silicon and the existence of this potential well, the detection efficiency is not optimal and can be improved. The potential well can be eliminated by the introduction of a thin layer of $p+$ doped silicon [68]. This solution provides high quantum efficiency in the UV range if the dopant concentration is sufficiently high and if the $p+$ layer is sufficiently thin.

Regarding the space heritage of back-thinned CCD, we can cite the detector of the Extreme ultraviolet Imaging Telescope (EIT) instrument on-board the SoHO spacecraft [69]. EIT was developed at CSL and its detector is a back-thinned CCD specially designed for the instrument which was working in the extreme UV at four different wavelengths: 17.1, 19.5, 28.4 and 30.4 nm [69]. Other famous instruments such as the Faint Object Camera (FOC) on the HST [70] or its replacement, the Advanced Camera for Surveys (ACS) [71], used or are using back-thinned CCDs for detection in the UV as well as in the visible domains.

#### 4.3.2.2 CMOS

The Complementary Metal Oxide Semi-conductor (CMOS) is a light sensor which is often compared to its technological competitor, the CCD. Unlike CCDs, CMOS detectors have most of their required electronics integrated onto the sensor itself. In other words, each pixel of a CMOS contains its own active amplifier right back to the light sensitive area. The light reaching the pixel creates electric charges (electrons) that are then converted into an amplified voltage signal that can be processed by the rest of the sensor electronics [72].

The main difference between CCDs and CMOS resides in the output of the pixels. In the case of CCDs, the output is an electrical charge which is transferred to an amplifier circuit to be converted. For CMOS, it is a voltage already amplified by the pixel's direct circuitry. There are also other differences relative to the main electronics architecture of the sensors according to [72].

However, the basic principle of the two sensors is fundamentally the same: the light is falling onto an array of pixels composed of a semi-conductor material that creates electrons by means of the photoelectric effect. Therefore, a practical comparison of the devices is needed [72]:

- Typical CMOS sensors have a lower detection uniformity than CCDs due to the direct electronics associated to the pixels. The images captured by CMOS sensors have generally more noise than the ones of CCDs.
- CMOS sensors are relatively young compared to CCDs. Their manufacturing process is still expensive while the same process for CCDs is very mature and therefore less expensive.
- CMOS packages are smaller and theoretically consume less power than CCDs.

It appears from this brief comparison that CCDs are always a good solution for astronomical observation because they are more efficient than CMOS. Due to the fact that this technology is also very mature, it is also currently cheaper regarding custom demands and a priori more reliable. However, CMOS are highly studied and developed and start also to be considered for space science missions. For example, the detector of the SWAP instrument on-board PROBA-2 is a CMOS [73]. Due to their small footprint and consumption, they should be very promising for the future.

#### 4.3.2.3 Microchannel Plates (MCP)

Microchannel Plates (MCP) are plates composed of numerous microscopic electron multiplier channels. The upper and lower surfaces of these plates are metallised electrodes. An external high voltage is applied to these electrodes. The inner surfaces of the channels are semiconducting such that a current through the channel surface produces a homogeneous electrical field inside it [74]. Figure 4.29 presents an overview of a general MCP structure.

An MCP detector assembly uses one or several MCPs that are stacked together in front of an optical coupler. The MCP part does not allow to produce an image as CCDs do for example. This is why an optical coupler is needed for imaging the observed scene. The working principle is the following [74]:

1. An incoming photon hits a channel surface, releasing an electron thanks to the photoelectric effect;
2. The electrical field accelerates the photo-electron towards the back end of the channel;

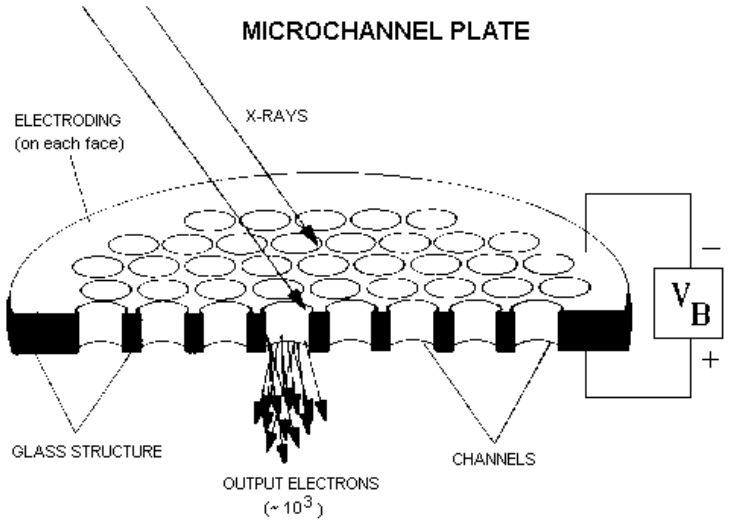


Figure 4.29: Schematic overview of the MCP structure from [75]. The voltage $V_B$ is applied to the electrodes. In this example, the incoming light is X-ray light because the figure source is relative to the High Resolution Camera on-board the Chandra satellite.

3. The photo-electron hits the channel wall and may release additional electrons;
4. An electron avalanche is created in the channel before leaving it to the optical coupler device;
5. The optical coupler could be a phosphor screen or a detector such as a CCD or a CMOS.

As it can be seen in Figure 4.29, a single photon can produce, at the end of the MCP, one or several thousands of photo-electrons. By stacking several MCPs together, the gain can easily reach dozens of thousands which is very large. In this kind of detector assembly, each photon counts as it is able to produce such electron avalanches at the end of the detection chain. This is the biggest advantage of these detectors that can work as photon counter.

MCPs are directly sensitive to UV photons, X-rays, $\alpha$-particles, charged particles and neutrons as well as electron beams and ions [74]. Even if the detection efficiency of UV photons is relatively low because of their low energy compared to the other detectable photons/particles, MCP detectors have already been used for UV space instruments such as the Cosmic Origins Spectrograph (COS) on-board the HST [76] for example. One drawback of these detectors is that they require a high voltage to create the electrical field needed for the acceleration of the photo-electron.

#### 4.3.2.4 Conclusion

Since the main types of detector technologies suitable for UV photometry have been reported, it is now possible to compare them with respect to their major characteristics in order to select the most appropriate architecture for the instrument's detector assembly. The main points of interest are the following:

- **QE over the spectral domain of interest**: The QE should be as high as possible over the [2500-3500] Å range. This way, the instrument will be more efficient and will satisfy the scientific requirements: it will be possible to observe fainter stars (*3U-4*), to achieve higher photometric accuracy (*3U-5*) and to reduce the observation time (*3U-6*).

- **Space heritage**: Having a high heritage in space missions is an advantage as it means that the system is robust and can be easily accommodated to space environment without a lot of development. As in this chapter we are not interested in technology demonstration, we try to design the most robust system with elements that have already proven their reliability.

- **Mass and volume constraints**: The lightest and least bulky assembly is preferred. Indeed, we are working with a 3U Cubesat which is a very small platform and it does not allow to use any kind of system without paying attention to its mass and volume. The Cubesat standard only allows a total mass of 4 kg for the triple unit platform [6]. We also previously identified that 1.5U is dedicated to the payload and the other 1.5U for the sub-systems. The size of the detector assembly should be compliant with this constraint.

- **Complexity**: The more complex a system the more development it needs to be integrated to an instrument. Our philosophy is to reduce the development duration and the costs for such a small satellite. The least complex system should be preferred.

Table 4.3 summarizes the characteristics listed before for the different detector technologies. The QE values exposed in the table came from information given by several manufacturers such as e2v and Hamamatsu. They are leading image sensor manufacturers and we contacted them to obtain the QE of their various detectors. The table shows that CCDs are the most advantageous sensors in terms of QE, space heritage and mass/volume. CMOS sensors are also interesting for their mass/volume and complexity characteristics. On the other hand, MCP detectors appears to be beaten on every point, except for the space heritage, by other technologies for our application. It is finally apparent from this comparison that a CCD is the best choice to be integrated with the payload of the satellite. However, it must be emphasized that even if the CCD technology is well established and mastered, their high space heritage is mostly composed of visible applications and therefore their use in the near-UV is somewhat unusual.

| Characteristics | Back-Thinned CCD | CMOS | MCP Detector |
|---|---|---|---|
| QE over [2500-3500] Å | [55-75] % | [30-40] % | [20-30] % |
| Space heritage | High | Medium | High |
| Mass/Volume | Low | Low | High |
| Complexity | Medium | Low | High |

Table 4.3: Comparison of the different detector technologies available for performing UV photometry on-board a Cubesat.

A simple solution should be to use an off-the-shelf detector. e2v Technologies proposes a wide range of CCDs that can be directly used for astronomical photometry. They just have to be connected to a Printed Circuit Board (PCB) for control and data storage. As specified in Sections 4.2.1.3 and 4.2.1.4, the pixel size should be equal to 13 $\mu$m and the overall pixel array should be composed of 1024×1024 pixels in order to image the entire required FoV. **CCD47-20** from e2v [77] has these two properties. Table 4.4 presents the main characteristics of these detectors that will be used in the section relative to the photometric budget (Section 4.5).

| **Parameters** | **Value** |
|---|---|
| Pixel size | 13×13 $\mu$m |
| Number of pixels | 1024×1024 |
| Quantum efficiency at 300 nm | 60% |
| Full well capacity (peak) | 100 k$e^-$/pixel |
| Dark signal at 0°C (at -40°C) | 25 $e^-$/pixel s (0.05 $e^-$/pixel s) |
| Charge transfer efficiency | 99.9% |
| Readout noise at 20 kHz | 2 rms $e^-$/pixel |
| Maximum readout frequency | 5 MHz |

Table 4.4: Characteristics of the CCD47-20 from e2v [77].

### 4.3.3 Data Storage and Transfer

Current PCBs that are proposed for Cubesat applications are designed with several ports for memory cards up to 8 GB. It is reasonable to assume that our on-board data storage capacity will be at least 16 GB. An example of PCB/On-Board Computer (OBC) that could host 2 memory cards is the *ISIS On Board Computer (iOBC)* from ISIS Space [78] (see Figure 4.30). The iOBC is also able to embark some home-made software that will control the payload and the other sub-systems.

A scientific image size can be quantified using the number of pixels (Table 4.4). Assuming that each pixel contains 16 bits of information, the size of each image is evaluated at $DATA_{size} = 16 * 1024 * 1024 = 16.78\ Mb = 2.10\ MB$. If memory cards are only used for hosting scientific data, they are able to receive more than 7600

images before saturating.

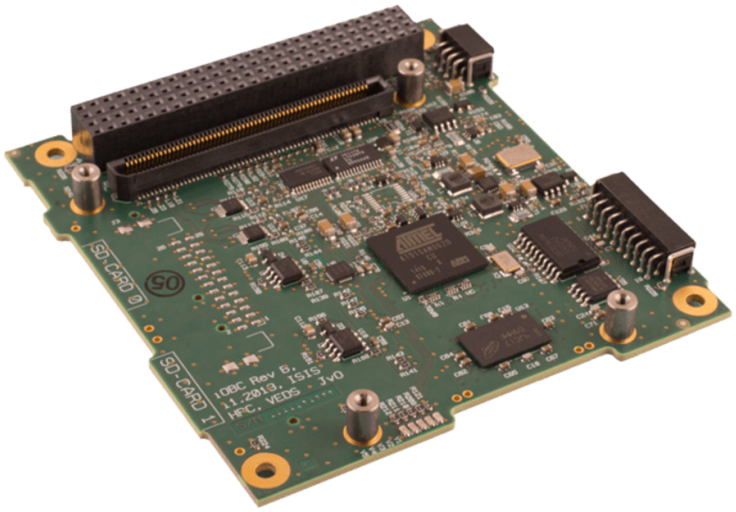


Figure 4.30: Overview of the iOBC [78].

Requirement *3U-8* from Table 4.1 indicates a duty cycle goal of 75%. In other words, it assumes that 75% of the mission is dedicated to scientific observation and therefore to data acquisition. Anticipating the orbit definition in Section 4.4.1, the duty cycle could be translated into approximately 75 min per orbit since the period will be approximately equal to 100 min. If the observation time goal of 1 min (requirement *3U-6*) is reached, 75 images will be acquired per orbit, which corresponds to 157.29 MB stored in memory cards. It will then take a little bit more than 100 revolutions to fill-up the entire memory. Two points have to be clarified before going further. The first one is that the photometric budget (Section 4.5) will show that is it not possible to reach the goal of only 1 min observation for all the targets. However, we are assuming here that this condition is reached in order to place the system in the case where the memory card fills the fastest. The second point is that the same photometric budget will also show that several integrations will be needed for the observation of one star because of saturation issues of the detector. In that case, several images (maybe several hundreds) will be stored in the memory cards for only one observation. It will be necessary to implement an algorithm on-board the satellite to combine the images to obtain only one final image that will be transferred to the ground later. The other ones will be deleted as soon as the combination is completed. Otherwise, we will saturate the on-board memory far too quickly.

Off-the-shelf antenna and communication controllers are numerous for Cubesats. From our research on manufacturers' websites, a data rate transfer up to 100 kbps is considered as a reasonable value for a preliminary evaluation. This rate transfer is indeed achievable using material from GOMSpace: a combination of the *NanoCom AX100* as transceiver controller and the *NanoCom ANT430* as antenna [79][80]. In terms of image transfer, it would take 2 minutes and 48 seconds to download a full image from the satellite to the ground station, i.e. more than 2.5 times longer

than the time of data acquisition. Hence, we will not be able to download full images while respecting the duty cycle goal (even the requirement which is equal to 60%). Restricting the data to a window of 100×100 pixels will reduce the image size to 0.02 MB (approximately a factor 100), which will be easier to handle with a COTS antenna: just a few seconds are needed to transfer such a small part of the image. A window of 100×100 pixels is sufficient to collect the signal of a target star and also the background surrounding it needed for data reduction. Since the mission is designed to observe bright stars, which are relatively isolated, such a windowing will not reduce the scientific return. However, if several targets could be observed simultaneously (e.g. observation of stellar clusters), the windowing algorithm associated to the CCD electronics could be adapted to enlarge the window (if the stars are close to each other) or to select several windows corresponding to each star of interest. These situations could be anticipated by establishing a very precise and complete observation plan for the entire mission coupled with an adapted windowing strategy.

### 4.3.4 Attitude Considerations

#### 4.3.4.1 Pointing

The attitude control of a satellite is controlling its orientation with respect to its center of gravity. It is thus directly related to the pointing of the satellite; i.e. the pointing of the instrument for observation. Therefore, the attitude is one of the major aspects of the system to take into account.

The last years have seen a lot of improvements in attitude control systems for Cubesats. For example, the ADCS of the BRITE satellites, launched in 2013 and 2014, is able to provide a pointing accuracy and stability of the order of 1 arcmin while the attitude determination is 10 arcsec [9]. In 2017, ADCS manufacturers such as Blue Canyon Technologies propose space qualified systems that guarantee a pointing accuracy and stability of the order of 20 arcsec with an attitude determination of 1 arcsec [81], which is in terms of pointing precision 3 times better than the performances of the last few years.

The *FleXcore* from Blue Canyon Technologies [81] is a fully integrated ADCS composed of 2 star trackers and 4 reaction wheel assemblies. It also integrates the processing unit designed to control the system and which can be easily connected to the OBC. The FleXcore is guaranteed to provide a pointing accuracy and stability of $\pm 0.002°$ ($1\sigma$) and around the 3 axes. It is easily translated into a pointing of $\pm 21.6$ arcsec ($3\sigma$), which corresponds to the worst accuracy in 99.7% of the time. Since the angular resolution of the instrument is equal to 11 arcsec and the pointing accuracy is worse than that, there is an uncertainty on the position of the PSF of an observed star in the focal plane. It is graphically represented in Figure 4.31. In this figure, there is 99.7% of chance that the whole PSF (red circle) falls inside the blue rectangle. Moreover, we know that with a FleXcore, the attitude determination is equal to 1 arcsec. It means that when we ask the ADCS to place the PSF at the

centre of the focal plane, like it is presented in Figure 4.31, the PSF will be inside the blue rectangle but we will know exactly where it is inside the rectangle because of the determination feedback. Therefore, we will know precisely which part of the detector is scientifically active, i.e. the position of the window that should be extracted for the data transfer.

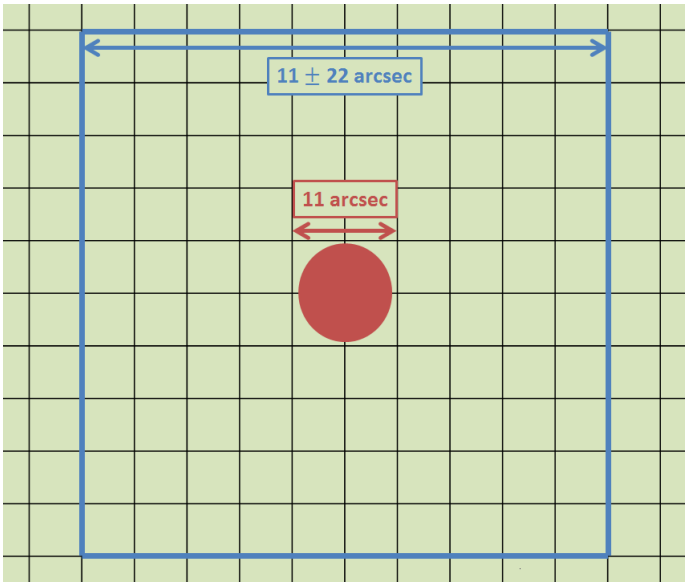


Figure 4.31: Overview of the PSF (red circle) of an observed star in the focal plane (green screen). The blue square represents the entire zone in the focal plane where the PSF could be if we ask the ADCS to place the PSF at the center of the figure.

With this kind of ADCS there is still a remaining problem: the pointing stability. If the attitude of the satellite varies during the observation of a star, leading to a displacement of the PSF in the focal plane, our photometric budget will be highly affected. However, the satellite attitude drift is a low frequency phenomenon that has an impact after a few seconds. A practical solution to reduce the systematic uncertainties introduced by the differences in sensitivity of the pixels would be to deliberately spread-out the stellar light over a large number of pixels either by defocusing the instrument or by averaging the signal over the full range of positions concerned by the attitude drift. Moreover, a very precise pixel-to-pixel calibration of the detector is therefore necessary before flight and the variation of this pixel-to-pixel response during the mission should be monitored. Unfortunately, it is not possible, because of the volume constraints, to embark a calibration unit in the satellite. An in-flight calibration of the instrument will be performed by the implementation of a chopping mode similar to the one of the BRITE satellites [35].

#### 4.3.4.2 Jitter Noise

Jitter noise was introduced in 4.2.2.3 as the LoS movements due to vibrations inside the structure. The main source of internal vibrations will be the reaction

wheel assemblies of the ADCS and the aim, at this stage, is to obtain an order of magnitude of these vibrations in terms of misalignment during observations. In this case, it is not possible to get rid of the jitter noise with short integrations because jitter is a high frequency noise and it will be present even over short time scales.

After requesting information from Blue Canyon Technologies, we have obtained the levels of reaction wheels imbalance inducing jitter noise:

- Static imbalance: 0.15 $g.mm$
- Dynamic imbalance: 4 $g.mm^2$

The static imbalance can be used to quantify the jitter noise in terms of angular perturbation. In first approximation we can consider that the Cubesat is a rigid body. The peak of jitter noise is then:

$$Jitter_{peak} = \frac{Wheels\ imbalance * Distance\ from\ wheels\ to\ CoG}{Moment\ of\ inertia}\ [rad] \quad (4.8)$$

where CoG corresponds to the Center of Gravity of the satellite. The CAD of the satellite entire system allows to know the distance from the wheels to the CoG and the moment of inertia along the three axes. The worst case is the perturbation around the z-axis (optical axis in Section 4.3.1.1) where we have:

$$Jitter_{peak} = \frac{0.15\ g.mm * 100\ mm}{2 * 10^8\ g.mm^2} = 0.075\ \mu rad = 0.015\ arcsec \quad (4.9)$$

The peak jitter, in the worst case, is equal to 0.015 arcsec if we assume a rigid Cubesat. With this value, it is safe to say that the star image will not move during observations and we are also far below the limit of 40 arcsec which is acceptable for the MTF degradation (Section 4.2.2.3). However, in the real situation the satellite will have some resonance modes that could be dynamically coupled with the imbalance of the reaction wheels. This behaviour will certainly increase the peak values of the jitter noise and thus has to be assessed in a more advanced phase of the satellite conception by computing a Finite Element Model (FEM) of the structure and performing a micro-vibration test with the input of the reaction wheels.

It has to be noted that the contact person of Blue Canyon Technologies proposed, based on their past experience with other Cubesats project, to take into account a dynamic amplification of the jitter peak from 10 to 100. A 100 amplification gives a peak of 1.5 arcsec which is still acceptable with respect to the PSF size and its positioning in the focal plane and the MTF degradation. It is therefore an encouraging point for the continuation of the design.

## 4.4 Thermal Environment and Analysis

### 4.4.1 Orbit Definition

#### 4.4.1.1 Launch Constraints

Cubesats are almost always launched as secondary payloads, i.e. they benefit from the launch of larger satellites. It means that the orbit is generally fixed by the primary satellite(s) because in most cases, Cubesats do not have any propulsion system to perform orbital manoeuvres. It is our case in this project: no propulsion system is considered. The advantage for Cubesats is that, since they are deployed by P-PODs (see Chapter 3), they can be integrated and launched into virtually any launch vehicle. Therefore, the launch possibilities are numerous.

Since no propulsion system is considered for the current satellite, a LEO is the baseline for the mission design. However, considering that the launch possibilities are numerous, we can define the kind of LEO that is the most suitable for the mission to be successful. A very interesting kind of orbit is the Sun-Synchronous Orbit (SSO) which is described in details in Appendix B. The main advantage of SSOs is that their orbital parameters can be tuned to obtain a quasi-constant Sun exposure of the satellite. This kind of SSO is called a *dusk-dawn* SSO. It can be easily defined using Equation B.6 that links the semi-major axis $a$ to the inclination $i$ (definition of the orbital parameters in Appendix B). Therefore, $a$ or $i$ should be fixed in order to calculate the other parameter. It can be seen in [82] that most of the satellites in SSO have a mean altitude between 600 and 800 km. It has thus been assumed that an altitude of 800 km would be an effective and reasonable choice. It is effective because with a higher altitude, the satellite will suffer less from the atmospheric drag and the mission duration, without propulsion to correct the altitude, will increase.

As specified above, the advantage of dusk-dawn SSO is the quasi-constant Sun exposure. It simplifies the definition of the thermal environment, minimizes the temperature variations during the mission and maximizes the amount of power available for the solar panels. However, it also has an important drawback: having a quasi-constant Sun exposure maximizes the satellite exposition to intense thermal radiations, hence maximizing the temperature of the satellite and its internal components. Since the selected detector is a CCD, it is rather negative to work with high temperatures because it increases the dark noise, affecting the detection efficiency. This problem has been taken into account and the solution was to design an optimized radiator connected to the detector assembly. The heat from the detector will be transferred to the radiator through a thermal strap and then it will be evacuated to cold space via radiation. The radiator design will be detailed in Section 4.4.2.

#### 4.4.1.2 Orbit Propagation

We established in the previous section that the orbit for the mission should be a dusk-dawn SSO with an altitude of 800 km, corresponding to a semi-major axis $a \approx 7200km$. Equation B.6 allows to calculate the inclination $i$ thanks to the definition of $a$. It gives an inclination $i = 98.58°$.

The dusk-dawn property of the orbit eventually constraints $\Omega$, the Right Ascension of the Ascending Node (RAAN, defined in Appendix B). Indeed, an ideal situation for such an orbit would be to have a $\beta$ angle equal to 90°, meaning that the Earth-Sun direction is perpendicular to the orbit plane. The $\beta$ angle is defined in Appendix B as the angle between the Earth-Sun direction and its projection onto the orbital plane of the satellite. The value of $\beta$ is linked to the inclination $i$, already defined, and also the RAAN $\Omega$ (Equation B.3). It is possible to easily define the full orbit using the *Satellite Tool Kit* (STK) software from AGI.

Table 4.5 presents a STK pre-recorded dusk-dawn SSO, defined while specifying the altitude and the launch date. The launch date was imagined on January 1, 2020 at midnight UTC (Universal Time Coordinated). As we are working with a circular orbit ($e = 0$), the definition of $\omega$ is meaningless and the standard is to define $\omega = 0°$ for the software in such cases. The true anomaly at launch $\nu_0$ is defined by STK thanks to the definition of the launch date.

| Parameters | Value |
|---|---|
| $a$, semi-major axis | 7178.14 km |
| $e$, eccentricity | 0 |
| $i$, inclination | 98.58° |
| $\Omega$, RAAN | 190.13° |
| $\omega$, argument of periapsis | 0° |
| $\nu_0$, true anomaly at launch | 0.11° |
| $T$, period | 100.87 min |

Table 4.5: Orbital parameters of the dusk-dawn SSO defined with STK.

Figure 4.32 shows the variation of the $\beta$ angle of the orbit presented in the Table 4.5. The variation of $\beta$ is a function of time and it is represented in the figure for a mission duration of 2 years (requirement *3U-7*). The absolute value $|\beta|$ is oscillating from 58° to 90°. The mean value is $|\beta_{mean}| = 74.19°$. Even if the variations of the angle seem to be high, it has to be noted that the definition of the SSO minimizes these variations. Without the constraints of the SSO for the orbital parameters (Appendix B), $\beta$ would vary from -90° to +90°.

For the eclipse fraction $f_{eclipse}$ (Equation B.4 in Appendix B), the results are presented in Figure 4.33. It can be seen that $f_{eclipse}$ remains at zero most of the time except when $|\beta| < 62.5°$. In this case, $f_{eclipse}$ reaches a maximum of 16.7% during two days of the simulated mission. It can be concluded that even if we have

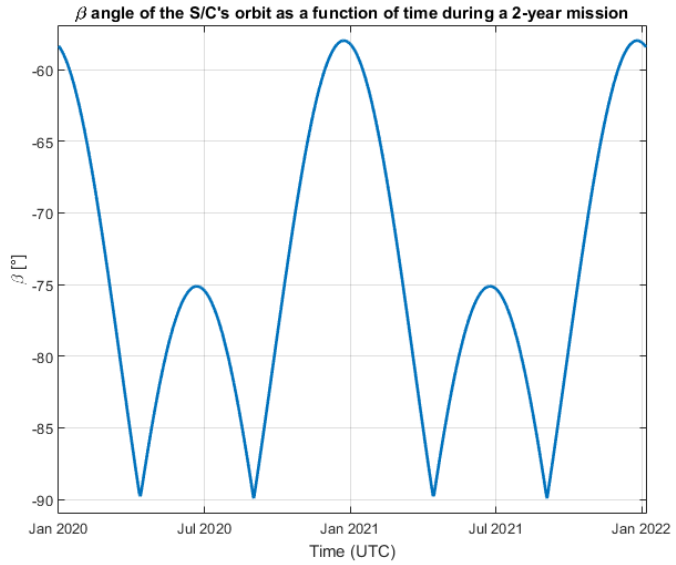


Figure 4.32: $\beta$ angle of the dusk-dawn SSO as a function of time during a 2-year mission.

defined an orbit that minimizes the environment variations, there are small parts of the mission during which eclipses of short durations occur. Even though these eclipses represent a small percentage of the time, they cannot be neglected and the satellite requires the use of batteries for the power supply and also a thermal analysis for quantifying the impact of eclipse/Sun exposure transitions and vice versa. These latter aspects will be taken into account in the next Section 4.4.2.

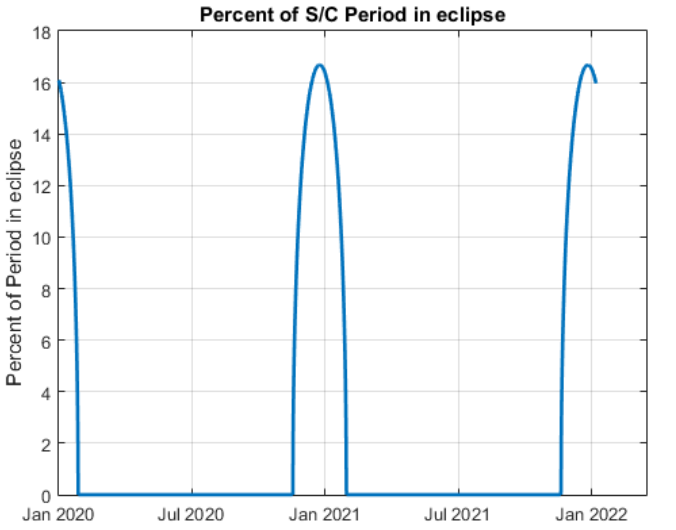


Figure 4.33: Percent of satellite period in eclipse as a function of time during a 2 years mission.

### 4.4.2 Thermal Considerations

In this section, a thermal analysis of the satellite will be presented. The objective is to present the external and internal thermal environment of the Cubesat, a thermal model made with ESATAN software and the results of this model when exposed to the thermal loads.

The detailed thermal analysis of the Cubesat is fully described in the master thesis of N. Berckmans [83]. This master thesis, that I proposed and supervised in 2017, was dedicated to the realization of a detailed geometrical mathematical model (GMM) and a thermal mathematical model (TMM) of the 3U Cubesat. These models were used to derive the temperatures encountered in the satellite especially in the worst thermal cases of the mission. These cases will be described in the following sub-sections. The goal here is not to detail the entire GMM, TMM and analyses presented in [83] (for the details, see this reference) but to explain the philosophy of the design and to demonstrate that it responds to the requirements of the mission.

#### 4.4.2.1 External Thermal Loads

There are three main heat sources that affect a satellite in LEO:

- The **Sun**: Direct sunlight is the main source of heat for a satellite orbiting around Earth. The heat flux coming from the Sun, $Q_{Sun}$, varies from 1322 $W/m^2$ at summer equinox to 1414 $W/m^2$ at winter equinox [83][84].
- The **Earth**: The Earth emits radiation in the IR domain. The radiation depends on the local temperature of the Earth.
- The **albedo**: The albedo is defined as the part of the sunlight reaching the Earth which is reflected to space. As for Earth radiation, albedo radiation varies as a function of the Earth surface which is reflecting the sunlight: snow reflection amounts to 80% whilst oceans reflection is about 5%. The mean albedo factor of Earth is 33%.

Since the satellite only sees a small part of the Earth at once, the Earth and albedo radiations vary much faster than the thermal inertia of the satellite [83]. Therefore average orbital values could be used. Handbooks such as Gilmore [85] propose average values for the Earth properties. For example, the effective temperature of the Earth ranges between 250.7 and 252.9 K. It corresponds, at our satellite altitude, to IR heat fluxes between 224 and 232 $W/m^2$ [83]. Concerning the albedo, two values are proposed: 33 and 34% based on [85].

For each heat source, the considered flux will depend on the thermal case under study. Two main cases are investigated in [83] and are presented here: the worst cold case and the worst hot case. Even though the names of the thermal cases are explicit, their detailed characteristics are presented in Table 4.6. Three remarks have to be made. First, the $\beta$ angle value of the cold case implies a maximum

$f_{eclipse}$ while for the hot case $f_{eclipse} = 0$ (see Figure 4.32). Second, a remark must be made about the seasons. At first it may seem weird that the cold case takes place in northern hemisphere winter when Earth is close to Sun hence the solar heat flux is maximum. However, Figure 4.32 shows that the periods with $f_{eclipse} \neq 0$ occur during winter. Integrating an eclipse in the analysis provides a colder case than having the lower solar heat flux without any eclipses. The impact of an eclipse is larger than the slight seasonal change in solar flux. Finally, the optical parameters correspond to the thermo-optical properties of the materials composing the satellite. They vary with time when exposed to radiation. The beginning-of-life (BOL) parameters generally allow to achieve colder temperatures than the end-of-life (EOL) parameters.

| Parameters | Cold case | Hot case |
|---|---|---|
| $\beta$ angle | -58° | <-62.5° |
| Season | Winter | Winter |
| Solar heat flux | 1414 $W/m^2$ | 1414 $W/m^2$ |
| Optical parameters | BOL | EOL |
| Earth heat flux | 224 $W/m^2$ | 232 $W/m^2$ |
| Albedo | 0.33 | 0.34 |

Table 4.6: Parameters of external environment for the thermal worst cases analysed in [83].

Eventually, the external environment of the satellite should be completed by the introduction of the *cold space*. Cold space represents the rest of the sky without the Sun and the Earth and can be represented as a black body with a temperature of only 2.7 K [84][85]. Therefore, it is not a source but rather a heat sink towards which we can evacuate heat. It will be used as the main element to cool the detector thanks to the radiator. The radiator, mechanically connected to the detector, will receive the heat of the detector via conductive transfer. After that, the radiator will radiate heat to deep space.

#### 4.4.2.2 Internal Thermal Loads: Power Budget

Internal thermal loads correspond to the heat dissipations of the sub-units inside the satellite. In order to quantify them, we first have to list the power properties of the units presented in Figure 4.23. Several COTS have been considered to quantify the general characteristics of the satellite. Many of these COTS have already been presented in Section 4.3: CCD detector, OBC, communication and antenna systems and ADCS. Their power characteristics still have to be considered. The solar panels and the battery system will also be presented with more details in this section.

The power characteristics of the already presented units are:

- **CCD Detector**: The classical power consumption of the CCD detector assembly is mainly driven by the operation of the associated PCB. In general, it

is of the order of 1 W [66][67]. Because the CCD is the most critical element with respect to temperature, we consider a security factor of two for its power consumption and the final value is therefore set to 2 W.

- **OBC**: The OBC, from ISIS Space [78], has a power consumption amounting to 400 mW on average with a peak at 550 mW.

- **Communication system**: Communication is supported by the NanoCom AX100 [79] from GOMSpace, which is associated to an additional OBC, also from GOMSpace. The total peak power consumption of the assembly (communication computer and additional OBC) is 4 W.

- **Antenna**: The deployable antenna is the NanoCom ANT430 [80] which is also from GOMSpace. It is coupled with the NanoCom AX100 communication system that handles the received and transmitted data from the satellite. The NanoCom AX100 is able to produce an output power directly transmitted to the antenna that varies from 29 dBm to 31 dBm [79]. This corresponds to a power ranging between 0.794 W and 1.258 W. This power has to be subtracted from the AX100 consumption and will not be included in the power budget. However, the deployment of the antenna should be considered for the budget. It is evaluated at 1 W.

- **ADCS**: The power consumption of the FleXcore [81] varies from 0.03 W to 2.82 W depending on the operational mode used (low power standby, star trackers on/off and reactions wheels on/off). However, we are expecting to observe a large percent of the mission duration and therefore it is assumed that the most consuming mode (star trackers + reaction wheels on) will be the most frequently used mode. It corresponds to a consumption of 2.82 W.

Since small parts of the mission will be in eclipse, the needs of a battery that stores the energy produced by the solar panels is demonstrated. The *NanoPower P31U*, from GOMSpace, is able to store energy up to 20 Whr and manage an amount of 30 W coming from the solar panels [86]. The control electronics of this battery system only needs 0.2 W to work.

Many manufacturers propose solar panels for Cubesats. We have chosen the panels from Clyde Space because they are well-documented and have flight heritage [62][87]. An overview of double-deployed solar panels for 3U Cubesats is shown in Figure 4.34. According to P. Anderson from Clyde Space, each single panel (10 $\times$ 30 cm) is able to generate 6.5 W when exposed to the sunlight at normal incidence, at a temperature of 60°C and at BOL. It is also estimated that, for a 2-year mission, the degradation of the power generation should not exceed 15%, giving $P_{2years} = 5.525\ W$. Assuming a linear degradation of the panels efficiency with time, a degradation of 30% is expected for a 4-year mission (goal of requirement *3U-7*), leading to $P_{4years} = 4.55\ W$.

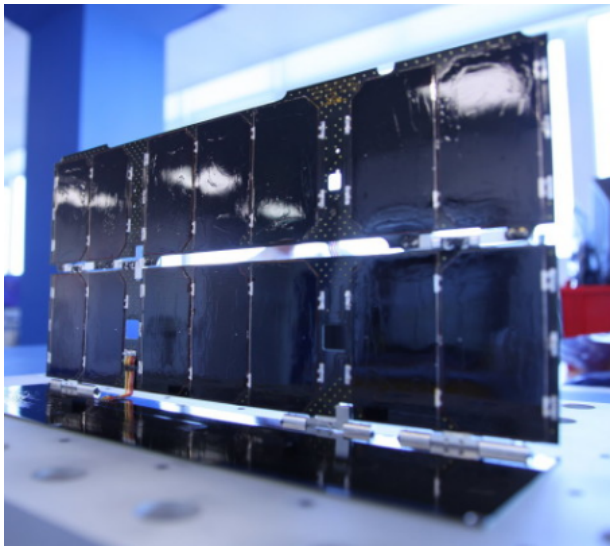

Figure 4.34: Double-deployed solar panels for 3U Cubesats from Clyde Space [62].

Table 4.7 presents the power budget, summarizing all the units of the satellite. The maximal power consumption of each sub-system is presented as well as a consumption with 20% margin applied for uncertainties. Within those margins, a total power of 18.68 W is obtained considering the specific worst case where all the elements are working simultaneously at their peak power. In order to allow this case to work in the worst configuration, i.e. at EOL of a 4-year mission, four solar panels are needed as well as a charged battery. However, this power budget is very pessimistic since this situation will not occur during the mission. For example, the antenna and solar panels mechanisms will just be used during the initial deployment phase of the satellite, at BOL and just once. This is why Table 4.8 considers more realistic operational cases. They provide some margins with respect to the power available during the mission, even at EOL with four panels facing the Sun. The most energy demanding case is the *Deployment* where we need 16.28 W. *Deployment* will only occur once at the beginning of the mission when the solar panels will be more efficient and the battery will be pre-charged. The flexibility on the power consumption can be used to enhance the sky visibility by relaxing the request of a normal Sun incidence on the solar arrays.

Since the *Deployment* phase occurs only once, it is not considered as the worst hot case even if it corresponds to the highest power consumption of the sub-units. We are more interested in the behaviour of the satellite during typical observation phases. Therefore the worst hot case, which was analysed in [83], corresponds to the *Obs + Data* phase where all the sub-units are active (except for the deployment mechanism). However, we also have to take into account the duty cycle (requirement *3U-8*) in the definition of the hot case. The goal is to achieve a duty cycle of 75%. It means that 25% of the time, the satellite will not be in an observation phase. It is implemented in [83].

| Component | $P_{max}$ (W) | $P_{max}$ with 20% margin (W) |
|---|---|---|
| Detector assembly | 2.00 | 2.40 |
| On-board computer | 0.55 | 0.66 |
| Communication system | 4.00 | 4.80 |
| Antenna (mechanism) | 1.00 | 1.20 |
| ADCS | 2.82 | 3.38 |
| Solar panels (mechanism) | 5.00 | 6.00 |
| Battery | 0.20 | 0.24 |
| **TOTAL** | **15.57** | **18.68** |

Table 4.7: Power budget.

| Component | Deployment | Observation | Data transfer | Obs + Data |
|---|---|---|---|---|
| Detector assembly | NO | YES | NO | YES |
| On-board computer | YES | YES | YES | YES |
| Communication system | YES | NO | YES | YES |
| Antenna (mechanism) | YES | NO | NO | NO |
| ADCS | YES | YES | YES | YES |
| Solar panels (mechanism) | YES | NO | NO | NO |
| Battery | YES | YES | YES | YES |
| $\mathbf{P}_{total}$ (20% margin) | **16.28** $W$ | **6.68** $W$ | **9.08** $W$ | **11.48** $W$ |

Table 4.8: Expected operational phases during the mission including 20% margins.

The worst cold case could be defined as the *Observation* phase where the power consumption is the lower in Table 4.8. However, it was decided in [83] to analyse a colder phase where the detector assembly is not working. It is not defined as a failure mode but as a kind of standby mode where it is not possible to observe a star (if there is no visible target) and we do not have access to a ground station, thus prohibiting to use the communication system. In the worst cold case of [83], only the ADCS and the battery are working (3.62 W). The ADCS has to be active all the time to control the position of the solar panels with respect to the Sun. In the same way, the battery has to manage the power coming from the panels all of the time.

In the two worst cases, the power relative to a sub-unit which is on is considered as an internal heat source in the TMM. Concerning the solar panels that are producing electricity thanks to the energy coming from the Sun, the situation is more complex. The panels collect a certain amount of energy which corresponds to $Q_{Sun}$ multiplied by the surface area. From this amount of energy, a part is converted into energy and is used for the satellite. This part has to be removed from the solar panels thermal balance to derive their temperature.

#### 4.4.2.3 Thermal Model

The thermal model of the satellite, detailed in [83], can be split in two distinct parts:

1. The **Geometrical Mathematical Model** (GMM): In the GMM, the detailed geometry of the satellite and its sub-units is simplified in order to mathematically describe the geometry. The main purpose of the GMM is to compute the radiative exchange factors between surfaces. These factors are only geometry-dependent and their determination is primordial to describe the radiative exchanges with precision. The GMM is also used in ESATAN to define interfaces between different parts and the software automatically computes thermal conductances.

2. The **Thermal Mathematical Model** (TMM): In the TMM, the thermal and thermo-optical properties of the materials are defined. This includes the thermal conductivity, density, heat capacity, absorptivity, emissivity, etc [83][84]. The heat sources and dissipations are also defined in the TMM. The definition of the materials and their properties associated to the geometry simplification of the GMM allows to fully determine the system with respect to thermal considerations. Figure 4.35 shows the simplified geometry of the GMM as well as the definition of materials of certain parts of the satellite.

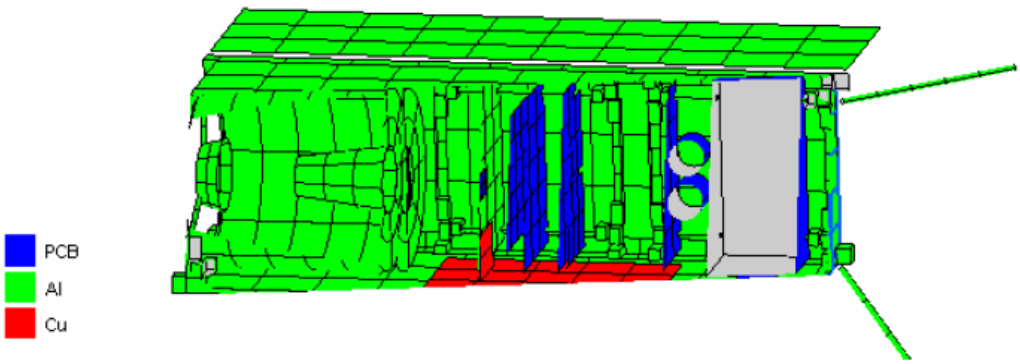


Figure 4.35: Cross-sectional view of the GMM and the definition of materials for certain parts of the satellite [83].

The main material is the aluminum 6061 alloy which composes the main structure, the solar panels structure, the antenna, the structure of the ADCS, the mirrors and the baffle of the payload and the detector support. A *PCB* material is used for the OBC, the communication system, the battery board and the ADCS and detector electronics. Copper composes the radiator. The external surfaces are covered by a white paint in order to reduce the absorbed external fluxes and to increase the power radiated to deep space, cooling the satellite.

The results of the preliminary simulations were problematic in the worst hot case [83]. Indeed the temperature of the detector was way too high (more than 40°C), leading to an enormous dark noise compromising the observations. To correct this problem, we have optimized the detector assembly model. The detector assembly model has been refined to integrate all the parts presented in Figure 4.36 and Permaglas is now defined as the material for the insulating part in the detector assembly.

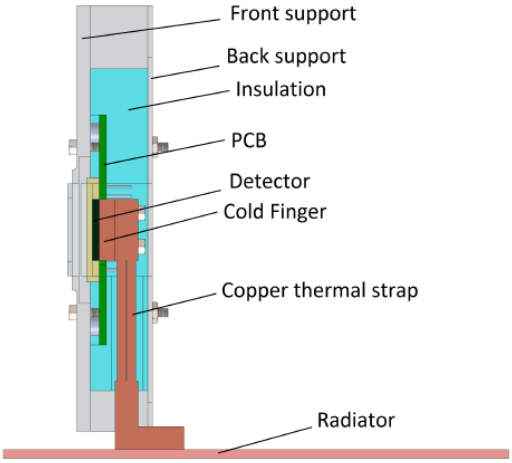


Figure 4.36: Cross-sectional view of the detector assembly [83].

The radiator design has also been modified and optimized to improve the cooling of the detector. The cold finger, made of copper, is directly glued on the rear side of the sensor thanks to a clearance in the PCB. The thermal strap length is minimized by using a straight line path through the insulation and its cross section area is maximized in order to increase its thermal conductivity. The radiator is connected to the structure of the satellite via four clams made of titanium. Titanium is used to obtain a low conductive link between the radiator and the structure while having a strong fixation. Eventually, the area of the radiator has been increased from 8 $10^{-3}$ $m^2$ to approximately 14 $10^{-3}$ $m^2$ for radiating more heat to deep space. The final results using this optimized design are presented in the following section.

#### 4.4.2.4 Results for the Worst Thermal Cases

Before presenting the results of the thermal analyses, a point concerning the number of solar panels has to be discussed. During the master thesis of N. Berckmans, the discussion concerning the number of solar panels needed was still an open subject. There were uncertainties concerning the power consumption of certain subunits, especially the communication system and the antenna. Moreover, the EOL power generation of the solar panels was overvestimated compared to that previously presented. Therefore, it was considered, at the period of the thermal analyses, that two solar panels were sufficient for the mission. The results presented in this section have been made for a 3U Cubesat with only two deployable solar panels.

However, we established by calculation what is the temperature difference between a case with two and a case with four panels. It is documented in [83]. The temperature difference between the two designs are less than 5%. It is thus assumed that the results from [83] with two solar panels can be used for a four-solar panels design.

**Worst cold case**

Figure 4.37 presents the temperatures encountered for each component of the satellite during one period corresponding to the worst cold case. The eclipse part of the period is highlighted in orange on the graphs.

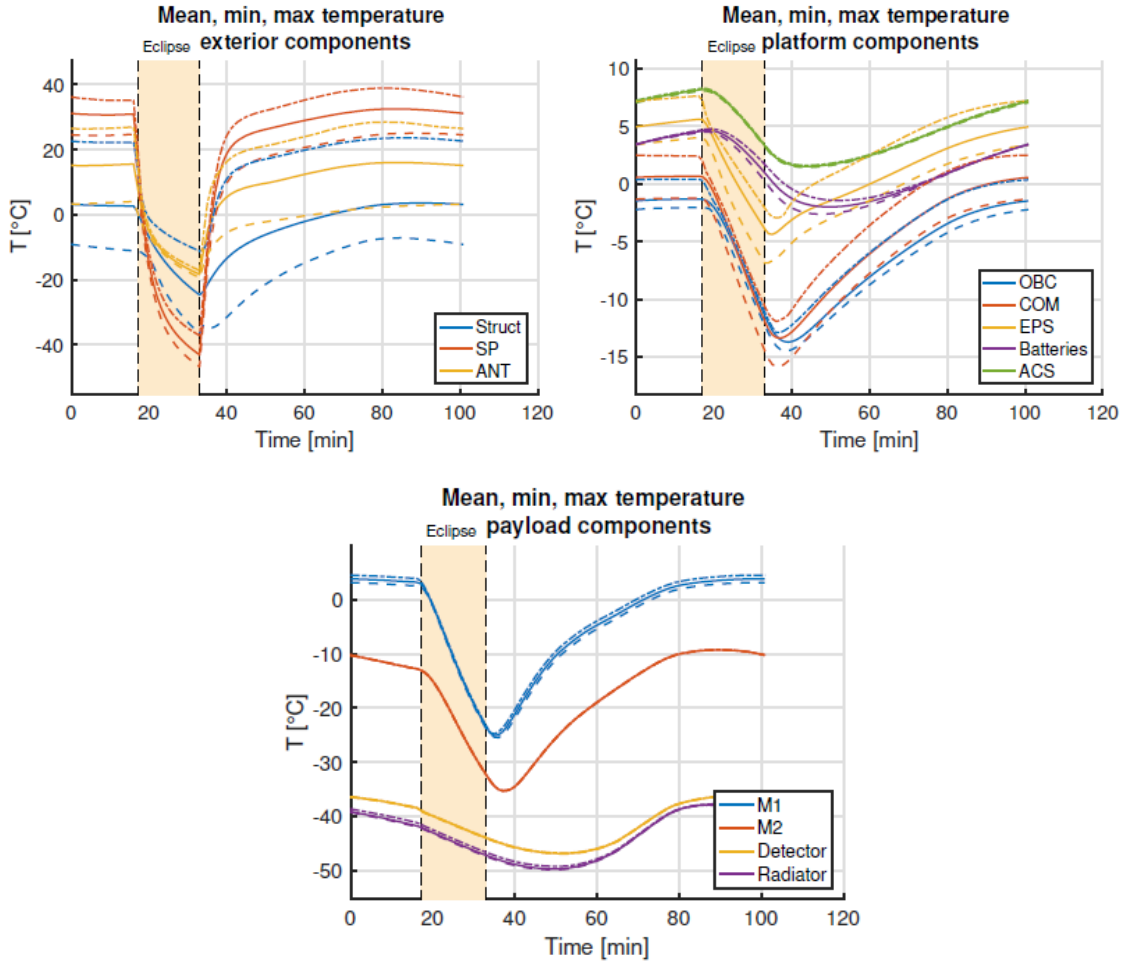


Figure 4.37: Minimum (dotted lines), average (solid lines) and maximum (broken lines) temperatures of the satellite components during one period and for the worst cold case. Eclipse time interval is highlighted in orange. *Top left*: results for the structure, the solar panels and the antenna. *Top right*: results for the OBC, the communication system, the battery (EPS+batteries) and the ADCS. *Bottom*: results for the mirrors, the detector and the radiator [83].

First, it can be seen that the largest differences between minimum and maximum temperatures concern the external parts of the satellite, i.e. the structure, the solar panels and the antenna. This is due to the fact that these parts are the largest surfaces of the satellite and their temperatures highly depend on the external environment: some surfaces are facing the Sun while others only see the Earth or the cold space. These external components of the satellite are also submitted to large temperature variations during one orbit. The solar panels, for example, have an average temperature around 30°C when stabilized and it drops to -40°C at the end of the eclipse. It only takes approximately 10 min to recover a temperature close to the stabilized plateau again. Second, as expected, the hotter internal elements are the ADCS and the battery system (decomposed in *EPS* for the PCB part and *Batteries* in the graph) with temperatures between -5°C and 7.5°C. It was expected because they are the only sub-units working and thus dissipating heat. The temperature variations during one period for these elements are low, of the order of 5°C, because of their local heat sources. Eventually, the other internal elements are colder and they are also subject to larger temperature variations during one period, around 15 and 20°C.

The results of Figure 4.37 are directly extracted from ESATAN after running the analysis based on the GMM and TMM. We have to keep in mind that, even if the results are certainly representative of what will be encountered in reality, some uncertainties persist in the model. The GMM is a simplified geometry of the satellite. It discretizes the real structure into nodes with simple geometries, therefore simplifying part of the information. The properties of the materials could also differ from the ones used in the TMM because of unexpected degradations for example. Therefore, it is recommended to add security margins on the predicted temperatures in order to verify that all the components will remain in their operational temperature ranges. The comparison between the predicted temperatures and the required ones is presented in Table 4.9 [83].

| Component | $T_{min}$ required | $T_{max}$ required | $T_{min}$ cold case | $T_{max}$ cold case |
|---|---|---|---|---|
| Structure | -40 | 80 | **−51.52** | 8.65 |
| NanoCom ANT430 | -55 | 100 | -34.35 | 13.94 |
| Solar panels | -150 | 110 | -61.74 | 23.90 |
| iOBC | -25 | 65 | -24.48 | -9.60 |
| NanoCom AX100 | -30 | 85 | -24.29 | -8.51 |
| NanoPower P31U | -40 | 80 | -12.63 | -5.24 |
| ADCS | -10 | 40 | -8.58 | -1.71 |
| Detector | - | - | -56.93 | -46.11 |

Table 4.9: Operational temperature ranges of the elements composing the 3U Cubesat and predicted temperatures during the worst cold case. A margin of ±10°C is applied on the predicted temperatures of internal components and ±15°C is applied for the external components. All temperatures are expressed in °C [83]. Bold indicates the predicted temperature which is outside the specification limit.

In Table 4.9, the temperatures required are extracted from the data-sheets of the elements. These data-sheets have been referenced any time a sub-unit was presented. The predicted temperatures from the cold case have been modified with security margins. For internal components (iOBC, NanoCom AX100, NanoPower P31U, ADCS and Detector), we have $T_{min} = T_{min,ESATAN} - 10°C$ and $T_{max} = T_{max,ESATAN} + 10°C$ while for external components (Structure, NanoCom ANT430 and Solar panels), we have $T_{min} = T_{min,ESATAN} - 15°C$ and $T_{max} = T_{max,ESATAN} + 15°C$. It can be seen that with these margins, the minimum temperature of the structure is below its specification limit. Two solutions could be undertaken to solve this problem. The first one is a modification of the surface optical properties of the colder part of the structure to absorb more heat from external sources. However, this solution could have a negative effect in the worst hot case, where we could reach too high maximum temperatures. The second solution is placing one or several heaters on the cold part of the structure. Since the power available is not totally used during this worst cold case, it is possible to use part of the remaining power to feed one or several heaters. The main drawback of such a solution is that it makes the system more complex in design and control. Such an implementation should be studied in detail before validation.

The worst cold case does not present any other critical issues. However, a point that should be considered in a more advanced phase of development is the thermo-mechanical behaviour of the structure. Large temperature variations could induced large mechanical constraints that should be avoided. Once again, if this is the case, this problem could be solved by the use of heaters.

**Worst hot case**

Figure 4.38 presents the temperatures encountered on each component of the satellite during one period for the worst hot case. In this case, there is no eclipse but there is a non-operational phase during the orbit. Indeed, it is assumed that we are meeting the goal of requirement *3U-8* concerning the duty cycle: 75% of the period is dedicated to scientific observations, the other 25% of the time is a standby mode similar to the one of the cold case. In this worst hot case, the temperatures of most parts are relatively constant because the thermal environment is constant. Only the sub-units that are turned off during the non-operational phase are submitted to temperature variations. The temperature of the solar panels is between 50 and 60°C while the temperature of the detector does not exceed 0°C during observations.

As for the worst cold case, Table 4.10 presents a comparison of the predicted temperatures including security margins to the required temperatures of the sub-units. This time, it is the ADCS that reaches a too high temperature, exceeding its maximum allowed temperature by 1.04°C. However, it is not considered as a critical issue. For this thermal analysis, we do not have a detailed design of the ADCS and therefore the thermal model of the ADCS is very basic. It is represented by one box with only one node for the sub-system and one node for the star trackers window. Once again, in a more advanced phase, a more detailed model of the ADCS should

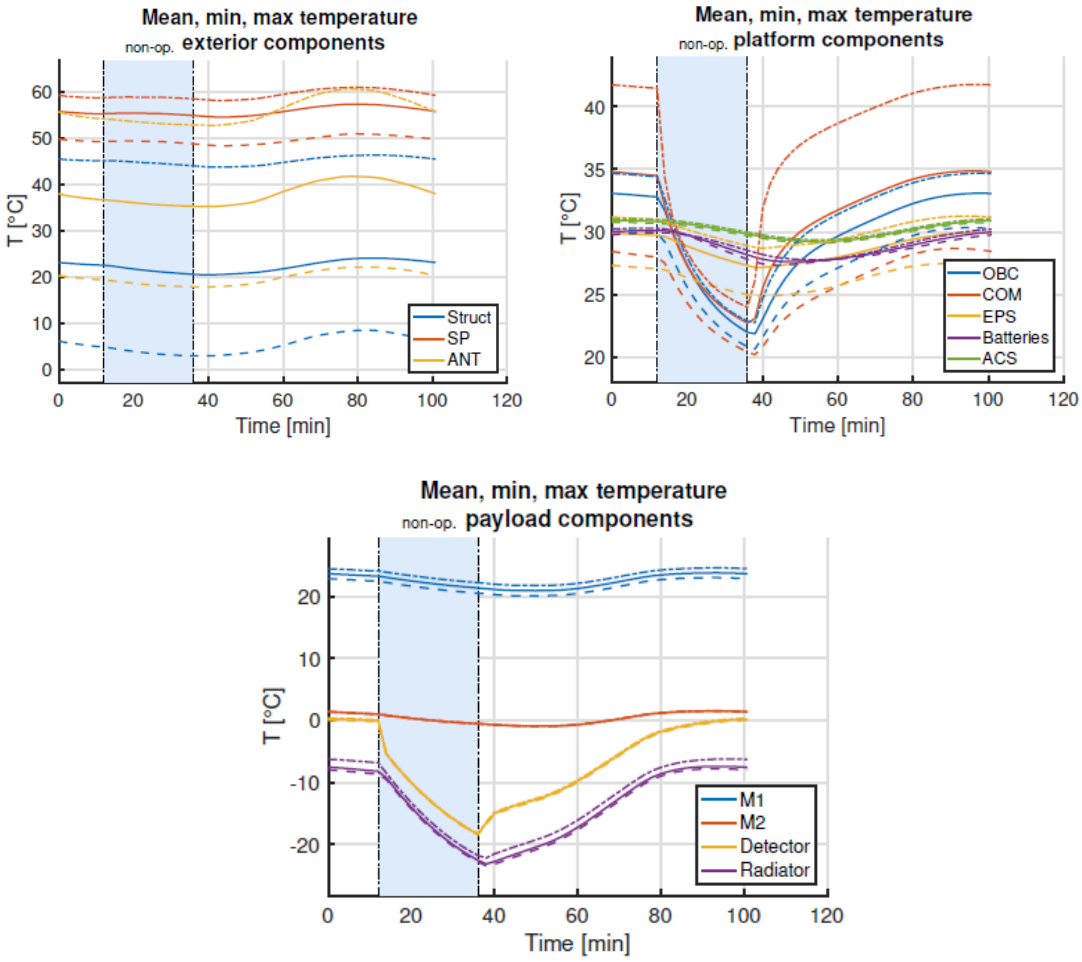


Figure 4.38: Same as Figure 4.37 but for the worst hot case. Non-operational phase is highlighted in blue [83].

be used after contacts with the manufacturer. Having a more precise model should allow us to obtain more precise results and to optimize heat transfers accordingly.

| Component | $T_{min}$ required | $T_{max}$ required | $T_{min}$ cold case | $T_{max}$ cold case |
|---|---|---|---|---|
| Structure | -40 | 80 | 17.86 | 61.24 |
| NanoCom ANT430 | -55 | 100 | 32.74 | 75.53 |
| Solar panels | -150 | 110 | 63.24 | 75.85 |
| iOBC | -25 | 65 | 30.64 | 44.69 |
| NanoCom AX100 | -30 | 85 | 33.41 | 51.77 |
| NanoPower P31U | -40 | 80 | 34.84 | 41.26 |
| ADCS | -10 | 40 | 39.11 | **41.04** |
| Detector | - | - | -8.46 | 10.33 |

Table 4.10: Same as Table 4.9 but for the worst hot case and including margins [83].

The most important information that we can extract from the worst hot case is the predicted temperature of the CCD detector. The dark noise of the CCD is a function of the temperature and increases with temperature. We have to verify if a maximum temperature of 10°C corresponds to an acceptable level of dark noise, allowing to reach the signal to noise ratio required for the scientific data to be relevant. It will be presented in the following section.

## 4.5 Photometric Budget

The aim of the photometric budget is to quantify the amount of photons reaching the detector for any given star. It will give information about the observing time needed to achieve the Signal to Noise Ratio (SNR) corresponding to the photometric requirement (*3U-5* in Table 4.1).

The temperature of the detector during the worst hot case, computed in the previous section, provides knowledge of the expected dark noise that will degrade the observations. The worst hot case also corresponds to the worst observation case because the temperature of the detector is the largest of the mission, leading to the largest dark noise. If we demonstrate that scientific observations can be carried out in this case, it validates the entire satellite design and its feasibility.

The optical/geometrical properties of the instrument, presented in Section 4.2, give information about the photon collecting area. We still have to analyse the surface coating of the mirrors to quantify their reflectance and compute the entire transmission of the telescope to the detector. This is presented in Section 4.5.4.1.

The first part of the photometric budget section is dedicated to the general characterization of the stars we want to observe with the photometer. The goal is to differentiate the stars according to their magnitude $V$ and their effective temperature $T_{eff}$. This characterization is presented in Sections 4.5.1 to 4.5.3.

### 4.5.1 Basic Equations

For any given star, the absolute magnitude in the V band[3] is given by $M_V = V - DM - A_V$ where $V$ is the apparent magnitude, $DM = 5 \log d - 5$ is the distance modulus ($d$ being expressed in parsecs) and $A_V$ is the interstellar absorption in the V band [88]. The bolometric magnitude[4] is then given by $M_{bol} = M_V + BC$ where $BC$ is the bolometric correction in the V band [88]. The bolometric luminosity $L_{bol}$, which is a measure of the total amount of energy emitted by a star, is then given

[3]The V band corresponds to the visual part of the spectrum in the UBV photometric system.

[4]The bolometric magnitude $M_{bol}$ takes into account electromagnetic radiation at all wavelengths contrary to the absolute magnitude in the V band $M_V$ which refers to the visual part of the spectrum only.

by [88]:

$$\begin{aligned} L_{bol} &= 3.03\ 10^{35}\ 10^{-0.4M_{bol}} \\ &= 3.03\ 10^{35}\ 10^{-0.4(V-DM-A_V+BC)} \\ &= 3.03\ 10^{35}\ 10^{-0.4(V-A_V+BC)}\ 10^{+0.4(5\log d-5)} \\ &= 3.03\ 10^{35}\ 10^{-0.4(V-A_V+BC)}\ 10^{\log d^2}\ 10^{-2} \\ &= 3.03\ 10^{33}\ d^2\ 10^{-0.4(V-A_V+BC)}\ [erg\ s^{-1}] \end{aligned} \tag{4.10}$$

As a first approximation, we assume that the spectrum of the star can be represented by a black-body[5] whose spectral emission follows the Planck function given by:

$$B_\lambda(T_{eff}) = \frac{2hc^2}{\lambda^5} \frac{1}{\exp\left(\frac{hc}{\lambda k T_{eff}}\right) - 1} \tag{4.11}$$

The power emitted over a narrow range of wavelengths $d\lambda$ hence is $d\epsilon = B_\lambda d\lambda$. The integral of this quantity over the full electromagnetic spectrum gives the Stefan-Boltzmann law $\frac{\sigma T_{eff}^4}{\pi}$. The energy flux emitted by a star of bolometric luminosity $L_{bol}$ and through a sphere of radius $d$ is $dF = \frac{L_{bol}}{4\pi d^2} \frac{B_\lambda d\lambda \pi}{\sigma T_{eff}^4}$ [90]. This latter formula yields the flux of a star over the narrow wavelength interval as one would see it from a distance $d$ and with zero interstellar absorption. The corresponding photon flux is $dN = \frac{dF\lambda}{hc}$. Therefore, using the expression of Equation 4.11, we get:

$$dN = \frac{2\ c\ L_{bol}\ d\lambda}{4\ d^2\ \sigma\ T_{eff}^4\ \lambda^4} \frac{1}{\exp\left(\frac{hc}{\lambda k T_{eff}}\right) - 1} \tag{4.12}$$

Expressing $\lambda$ and $d\lambda$ in Å, using the expression of $L_{bol}$ of Equation 4.10 and expressing the photon flux $dN$ in $cm^{-2}\ s^{-1}$, we get:

$$dN(V, T_{eff}) = \frac{8.402\ 10^{34}\ 10^{-0.4(V-A_V+BC)}\ d\lambda}{T_{eff}^4\ \lambda^4\ (\exp(\frac{1.439\ 10^8}{\lambda\ T_{eff}}) - 1)} \tag{4.13}$$

Equation 4.13 further needs to be corrected by the interstellar absorption $A_\lambda$ at the relevant wavelength [91]:

$$dN(V, T_{eff}) = \frac{8.402\ 10^{34}\ 10^{-0.4(V-A_V+BC+A_\lambda)}\ d\lambda}{T_{eff}^4\ \lambda^4\ (\exp(\frac{1.439\ 10^8}{\lambda\ T_{eff}}) - 1)} \tag{4.14}$$

[5]Whilst this might seem a poor approximation because of the numerous spectral lines in the UV domain, a comparison with synthetic spectra generated with genuine model atmosphere codes actually reveals differences in the number of photons received that amount to less than a factor two [89].

The interstellar absorption in the UV can be approximated as a function of wave-number $k = 10000/\lambda$ by [91]:

$$\begin{cases} \frac{A_\lambda}{E_{B-V}} = 1.56 + 1.048\ k + \frac{1.01}{((k-4.60)^2 + 0.280)} \text{ for } 2.70 \leq k \leq 3.65 \\ \frac{A_\lambda}{E_{B-V}} = 2.29 + 0.848\ k + \frac{1.01}{((k-4.60)^2 + 0.280)} \text{ for } 3.65 \leq k \leq 7.14 \\ \frac{A_\lambda}{E_{B-V}} = 16.17 - 3.20\ k + 0.2975\ k^2 \text{ for } 7.14 \leq k \leq 10 \end{cases} \quad (4.15)$$

In Equation 4.15, $E_{B-V}$ is the color excess expressed with the nomenclature of the UBV photometric system. The color excess is a description of the interstellar reddening and it is defined as the difference between an object's observed color index and its intrinsic color index.

### 4.5.2 Modelling

The remaining parameters of Equation 4.14 are listed below:

- $V$ is the apparent magnitude of the star. It will be kept as a free parameter for describing the targets as requirement *3U-4* specifies the maximum $V$ for the stars that should be observable with the photometer. For the analyses, we specify $V \in [0, 5]$.

- $T_{eff}$ is the effective temperature of the star. As for $V$, it will be a free parameter in the calculation of $dN$. Our prime interest focuses on massive stars of spectral type OB, down to B5. Such stars are the brightest in the UV domain and they influence not only their direct neighborhood but also material on the galactic scale, making them very interesting targets to observe [92]. It is shown in Table 4.11 that the spectral types of stars of the main sequence is related to their effective temperatures.

- $\lambda$ and $d\lambda$ are respectively the wavelength and the wavelength range on which the photon flux $dN$ is evaluated. As our photometer is working in the wavelength range between 2500 and 3500 Å, $dN$ should be integrated over this range to deduce the number of photons reaching the telescope per second:

$$N = \int_{\lambda_1=2500\text{Å}}^{\lambda_2=3500\text{Å}} dN \quad (4.16)$$

- $BC$ is the bolometric correction in the V band which allows to transform the absolute magnitude in the V band into the bolometric magnitude. The values of $BC$ as a function of the spectral types, hence also of the effective temperatures, are presented in Table 4.11.

- $A_V$ and $A_\lambda$ are the interstellar absorptions in the V band and at the considered wavelength respectively. $A_V$ is a correction which is only related to the V band while $A_\lambda$ depends on the wavelength of interest as it is demonstrated by Equation 4.15 where $k$ is directly linked to the wavelength.

| Spectral type | $T_{eff}$ [K] | $BC$ [mag] |
|---|---|---|
| O5 | 42 000 | -4.40 |
| O9 | 34 000 | -3.33 |
| B0 | 30 000 | -3.16 |
| B2 | 20 900 | -2.35 |
| B5 | 15 200 | -1.46 |

Table 4.11: Spectral type of stars on the main sequence, along with their associated effective temperatures and bolometric corrections [88].

At this stage, only $A_V$ and $A_\lambda$ are unknown for the integration of $dN$. However, we know from [93] that on average, $A_V$ and the color excess $E_{B-V}$ are linked through the relation $A_V = 3.1\ E_{B-V}$. Since $A_\lambda$ also directly depends of $E_{B-V}$, it means that if we determine the value of $E_{B-V}$, we can carry out the simulations for the computation of $N$. However, $E_{B-V}$ is specific to each source and depends on the environment between the star and us. Since we intend to establish a general photometric budget only depending on $V$ and $T_{eff}$, we rather consider some extreme values for the stars we are interested in. The next section will be dedicated to the determination of the most suitable values for the interstellar absorption $A_V$. Fixing, this parameter will allow to deduce the value of $E_{B-V}$, then $A_\lambda$ and finally $N$.

### 4.5.3 Interstellar Absorption $A_V$

We have based our analysis of $A_V$ on the *Yale Bright Star Catalogue* [94]. This is a catalogue referencing more than 9 000 stars with magnitudes up to $V = 7$, giving their spectral type and their color excess $E_{B-V}$. From this catalogue, we have investigated the distribution of $A_V = 3.1\ E_{B-V}$ for stars of spectral types O and B (down to B5) with magnitudes $V$ between 0 and 5. The distribution of more than 250 stars is presented in Figure 4.39. We found that $A_V$ falls in the range between 0 and 2.5 for all the stars in our sample. The mean value $A_{V,mean}$ is equal to 0.3 which corresponds to a low absorption.

Therefore, we considered two cases which have important implications on the photometric budget:

1. $A_V = A_{V,mean} = 0.3$: it is a realistic case where the interstellar absorption is relatively low. The flux of photons at the entrance of the telescope should be sufficiently high to acquire data quickly within the requirement or the goal of *3U-6*.

2. $A_V = A_{V,max} = 2.5$: it represents the worst case for observations because the interstellar absorption is the largest. It is considered as the most constraining situation for validating the telescope efficiency.

Figure 4.40 presents the integrated flux of photons $N(V, T_{eff})$ (Equation 4.16) calculated considering the two different values of $A_V$.

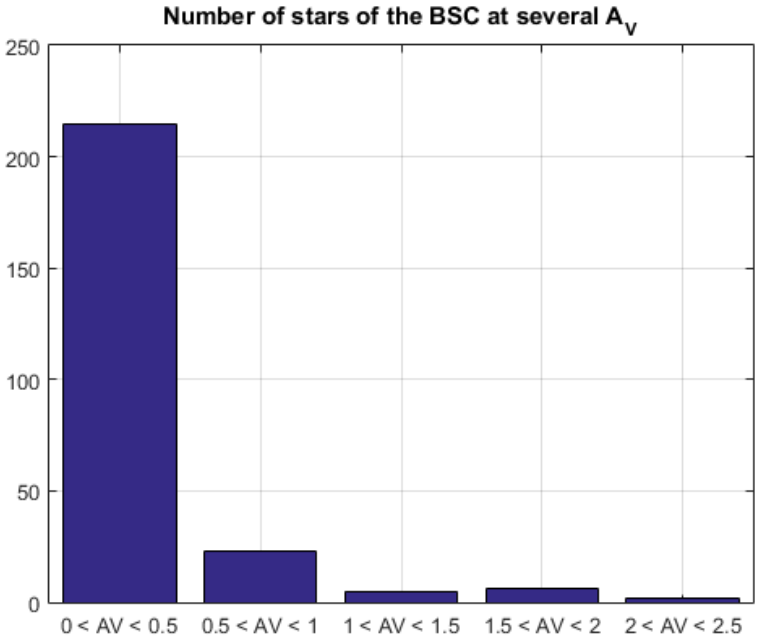


Figure 4.39: Distribution of stars from the Yale Bright Star Catalogue as a function of the interstellar absorption in the V band $A_V$[94].

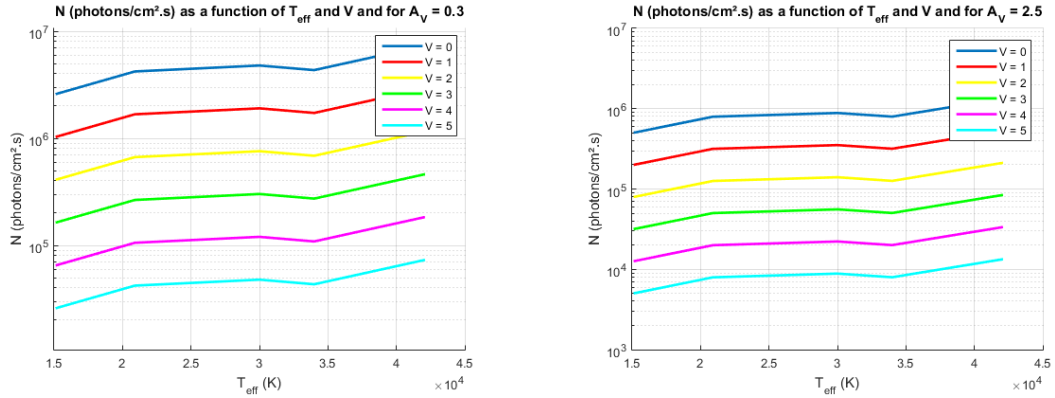


(a) $A_V = 0.3$ (b) $A_V = 2.5$

Figure 4.40: $N$ (expressed in $photons/cm^2\ s$) as a function of $T_{eff}$ (in K) and $V$ (in mag) for two different values of $A_V$, the interstellar absorption in the V band.

## 4.5.4 Observation Strategy

### 4.5.4.1 Total Efficiency of the Telescope

In order to compute the entire efficiency of the instrument on-board the Cubesat, we need to know the reflectance of the mirrors, the transmittance of the filter and the quantum efficiency of the detector. For the transmission of the filter, it has been presented in Figure 4.4. The mean transmittance at the interfaces of the filter

is equal to $\tau_{mean} = 54\%$ while the mean internal transmittance is $\tau_{i,mean} = 60\%$. Concerning the selected detector, its quantum efficiency over the wavelength range 2500-3500 Å is between $QE_{min} = 55\%$ and $QE_{max} = 75\%$.

For the mirrors, coatings have to be applied on them in order to improve their reflectance in the wavelength range 2500-3500 Å. Many coating manufacturers exist and we can cite, for example, Melles Griot who is able to provide UV improved coatings with a reflectance between $R_{min} = 82\%$ and $R_{max} = 92\%$ over the wavelength range of the instrument [95]. These values are considered as references for our application.

Therefore, it is possible to define two extreme values for the telescope's efficiency. The minimum value $\eta_{min}$ would be adequate for the definition of the worst observational case while the maximum value $\eta_{max}$ would be interesting to analyse the worst saturation situation of the detector (Section 4.5.4.3). In the two cases, the transmittance of the filter is equal to its average value because the differences between the minimum and maximum transmittance over the wavelength range is way too high and considering the extreme values would not be representative. We obtain:

$$\eta_{min} = R_{min}^2 * \tau_{mean}^2 * \tau_{i,mean} * QE_{min} = 0.0647 = 6.47\% \tag{4.17}$$

$$\eta_{max} = R_{max}^2 * \tau_{mean}^2 * \tau_{i,mean} * QE_{max} = 0.1111 = 11.11\% \tag{4.18}$$

To simplify the calculation of the SNR, the efficiencies $\eta_{min}$ and $\eta_{max}$ are assumed to be constant over the spectral domain.

#### 4.5.4.2 Signal to Noise Ratio (SNR)

One of the most important requirement for describing the quality of scientific observation is the signal to noise ratio (SNR). The SNR requirement is obtained from the photometric requirement *3U-5* expressed in magnitude in Table 4.1. The apparent magnitude $V$ could be defined as [88]:

$$V = -2.5 \ \log \frac{flux}{flux_{ref}} \tag{4.19}$$

Applying the errors propagation formula on Equation 4.19, we find:

$$\Delta V = \frac{2.5}{\ln 10} \frac{\Delta flux}{flux} = 1.086 \ \frac{\Delta flux}{flux} \tag{4.20}$$

Therefore, considering the requirement *3U-5* and Equation 4.20, we finally obtain:

$$SNR = \frac{1.086}{\Delta V} = \frac{1.086}{0.001} = 1086 \tag{4.21}$$

The required SNR is therefore equal to 1 086 while the goal specified for *3U-5* corresponds to a SNR of 2 172.

We know the value of the SNR that should be achieved but we still have to determine the signal $S$ and the noise $\sigma_{noise}$ such as $SNR = \frac{S}{\sigma_{noise}}$. The signal $S$ detected within an integration time of $t_{in}$ seconds is defined as:

$$S = N\ t_{int}\ A_{eff}\ \eta \tag{4.22}$$

In Equation 4.22, $N$ stands for the photon flux calculated in the previous sections, $A_{eff}$ is the effective area collecting the photons and $\eta$ is the total efficiency of the instrument. The effective area can be expressed as $A_{eff} = \frac{\pi \phi_{eff}^2}{4}$ in $mm^2$. The effective diameter $\phi_{eff} = 81.5\ mm$ has been quantified in Section 4.2.2.4. It corresponds to the equivalent diameter of the entrance pupil area minus the obscuration of the secondary mirror and its associated baffle. Fixing the characteristics of the observed star also fixes $N$ and it is then possible to calculate $S$ as a function of $t_{int}$.

The noise $\sigma_{noise}$ that we consider is composed of three main contributions: the photon or shot noise, the detector noise and the background noise. The shot noise is due to statistical fluctuations in the number of recorded photons from the effective signal [96]. The detector noise is mainly composed of the dark noise which is the signal generated by the detector in absence of input light signal and the readout noise which is encountered when measuring the signal of a CCD after the transfer of the charges to the amplifier [96]. The background noise is associated to the stray light and corresponds to the photons of unwanted off-axis angles that reach the same pixels as the observed stars [96]. The level of background noise has been quantified in Section 4.2.2.4 when the performance of stray light rejection of the baffling system was presented. The mathematical expression of the noise is given by [96]:

$$\begin{aligned}\sigma_{noise} &= \sqrt{n_s + n_d + n_b} \\ &= \sqrt{N\ t_{int}\ A_{eff}\ \eta + \#Pix\ D\ t_{int} + \#Pix\ R^2 + f_{SL}\ N_{SL}\ t_{int}\ A_{eff}\ \eta}\end{aligned} \tag{4.23}$$

The detailed contributions of noises in Equation 4.23 are:

- $n_s = N\ t_{int}\ A_{eff}\ \eta$ for the shot noise. It corresponds to the effective signal to which a square root is applied in the total noise count.
- $n_d = \#Pix\ D\ t_{int} + \#Pix\ R^2$ for the detector noise. $\#Pix$ is the number of pixels illuminated by the PSF of a star and was fixed to 4 in Section 4.2.1.3. $D$ is the quantification of the dark noise of the detector and it is expressed in $e^-/pixel\ s$. The curves of $D$ as a function of the temperature of the detector are presented in [77]. $R$ is the RMS value of the readout noise and it is expressed in $e^-/pixel$.
- $n_b = f_{SL}\ N_{SL}\ t_{int}\ A_{eff}\ \eta$ for the background noise. $f_{SL}$ corresponds to the fraction of stray light reaching a certain set of pixels. It was estimated at 0.7% in Section 4.2.2.4 for the central pixels of the detector. $N_{SL}$ was also estimated in Section 4.2.2.4 and it corresponds to the amount of photons from an entire hemisphere background reaching the instrument. It is expressed in $photons/cm^2\ s$.

Now that the SNR is defined, it is possible to calculate it for the worst observation case. This case corresponds to the hotter temperature of the detector (+10°C) leading to the higher value of $D$, the pessimistic prediction of having $\eta = \eta_{min}$, the observation of the colder star of Table 4.11 and eventually the highest interstellar absorption $A_V = 2.5$. The combination of all these effects minimizes $N$ and $\eta$, hence $S$, and maximizes the noise $\sigma_{noise}$. Figure 4.41 shows the results of this worst case. To fulfill the requirement for $V = 3$, the integration time must be approximately equal to 210 seconds, well below the limit of 300 seconds. However, for higher magnitudes V (4 and 5), it is not possible to achieve the required SNR in the maximum specified integration time. The main noise contribution comes from the background. In the mean time, the other magnitudes from 0 to 2 are meeting the requirement and even the goal for the SNR. For example, for $V = 2$, the goal of $SNR = 2\ 172$ is achieved in exactly 152 seconds.

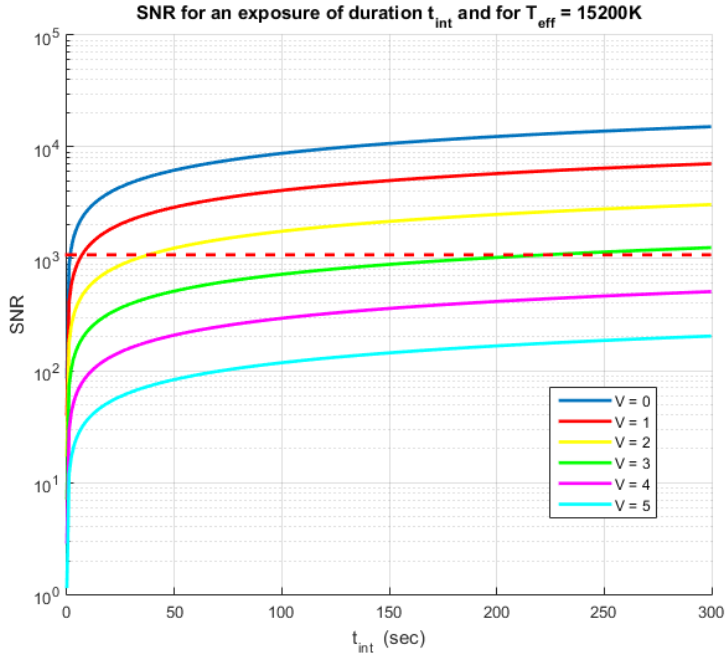


Figure 4.41: SNR for a star with $A_V = 2.5$ and $T_{eff} = 15\ 200K$. The detector is at a temperature of 10°C and the efficiency of the entire instrument is equal to 6.47%. The horizontal red dashed line corresponds to the SNR requirement of 1086.

The previous results are showing the limits of such a small telescope for the observation of the faintest stars among the possible targets. However, the previous case is very rare considering the distribution of $A_V$ of the bright stars illustrated in Figure 4.39. Figure 4.42 presents the results for a more realistic case where the interstellar absorption is equal to its average value $A_{V,mean} = 0.3$. It can be seen that the requirement on the SNR is achieved for all the magnitudes. For $V = 5$, it takes a few seconds less than the 300 seconds limit while for brighter stars less than 50 seconds are needed. It demonstrates that the scientific requirements *3U-5*, and

even its goal value, will be honored for the vast majority of the targets. We also have to keep in mind that the presented results are very pessimistic, considering a warm detector, the worst efficiency of the optical elements and the colder type of stars that could be observed with the system. We are thus confident that the SNR will be much better in most cases.

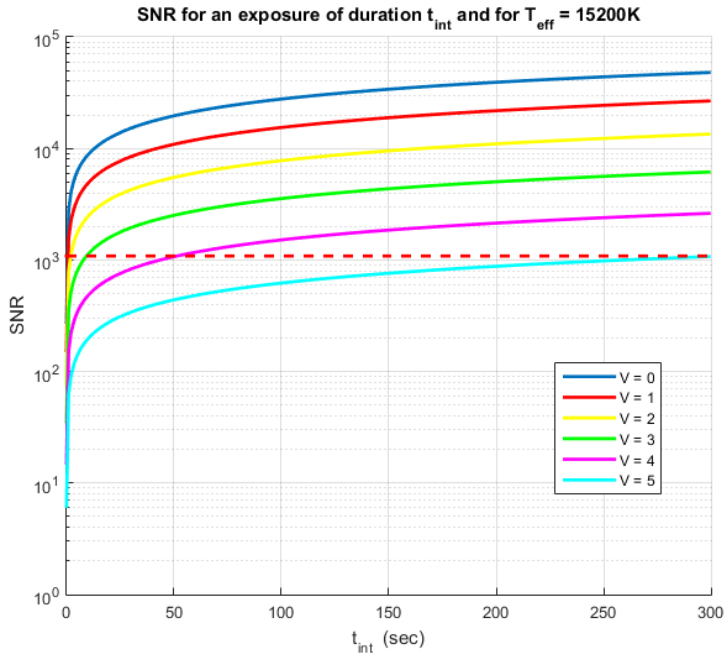


Figure 4.42: SNR for a star with $A_V = 0.3$ and $T_{eff} = 15\ 200K$. The detector is at a temperature of 10°C and the efficiency of the entire instrument is equal to 6.47%. The horizontal red dashed line corresponds to the SNR requirement of 1086.

To conclude on the SNR, it is interesting to mention that external effects can affect the SNR during the mission. The ageing of the CCD sensor is one of these effects. The ageing is due to the fact that the sensor is vulnerable to radiation-induced performance changes. The changes of the CCD characteristics can be of two types [97]: changes due to the ionizing dose of energetic charged particles and displacement damage arising from heavy particles (protons and neutrons). The main drawback due to both effects is an increase of the dark signal, coupled to a decrease of the charge transfer efficiency. These effects can be evaluated during pre-flight tests by performing accelerated ageing experiments and by calibrating the sensor in-flight. An in-flight solution could be to implement a chopping mode similar to what is done for the BRITE satellites, as already explained [35].

#### 4.5.4.3 Saturation Issues

The photometric budgets have shown that we benefit from a high quantity of photons at the entrance of the telescope in many cases. Therefore, even for the worst case scenario presented in the previous section, it will not be necessary, and

actually not possible to integrate the signal of the same star with only one exposure of duration $t_{int}$ because of the full well capacity $C$ of the detector. The peak value of $C$ is expressed in Table 4.4 as 100 000 $e^-/pixel$. It quantifies the number of electrons that can be generated on one pixel. The saturation limit of a pixel can be expressed as:

$$\frac{N\ t_{int}\ A_{eff}\ \eta}{\#Pix} + D\ t_{int} + R^2 + \frac{f_{SL}\ N_{SL}\ t_{int}\ A_{eff}\ \eta}{\#Pix} \leq C \tag{4.24}$$

It is assumed that all the energy of the PSF is uniformly spread over the four pixels illuminated by the star. This assumption is checked when looking at the spots of Figure 4.8 for low-axis angles.

Two extreme cases are considered to demonstrate the feasibility of the observations:

1. The first case is the best situation regarding scientific observations because we maximize $N$. However, it is the worst case regarding the saturation of the detector pixels. The maximization of $N$ is obtained considering the hottest star of Table 4.11 ($T_{eff} = 42\ 000K$), a magnitude $V = 0$ and the mean absorption $A_V = 0.3$. Such an object does not exist in reality but it allows us to probe the limitations of the instrument. Moreover, we also maximize the instrument efficiency $\eta = \eta_{max}$ to increase the number of generated electrons per second. Figure 4.43a presents the number of generated electrons on a pixel illuminated by the hypothetic hot star as a function of the integration time. The saturation occurs very quickly, in less than 0.03 s. The strategy would be to take two exposures of 0.02 s duration to reach (and slightly exceed) the requirement on the SNR. The SNR goal can be achieved by taking seven exposures of 0.02 s duration.

2. The second case is the worst case for the SNR calculation that can reach the requirement within 300 seconds. It was presented in the previous section: $T_{eff} = 15\ 200K$, $V = 3$, $A_V = 2.5$ and $\eta = \eta_{min}$. Figure 4.41 showed that it takes 210 seconds to reach the SNR for stars with $V = 3$. Now, Figure 4.43b presents the results for this second case: saturation occurs for integration times around 0.55 s. Therefore, several exposures need to be combined to reach the required SNR. A solution to reach the SNR would be 447 exposures of 0.5 s duration. These numerous observations are still compliant with the maximum observation time of 5 min/300 s per target. Assuming that the readout of each exposure takes 0.1 s, the total observation time would be $447 * (0.1 + 0.5) = 268.2\ s$, still within the allowed limits. Since the readout of the images could be done much faster considering the possible readout frequency of the detector (5 MHz, Table 4.4), there is no issue with this case.

The two presented cases have shown that the solution to remove saturation is to do several exposures of short duration of the same target and to combine the results of all the exposures to improve the SNR since $SNR_{tot} = \sqrt{n_{exp}}\ SNR_1$ ($SNR_{tot}$ is the SNR of the combination of the exposures, $n_{exp}$ is the number of exposures and $SNR_1$ is the SNR of only one exposure). This solution is relatively simple and is already

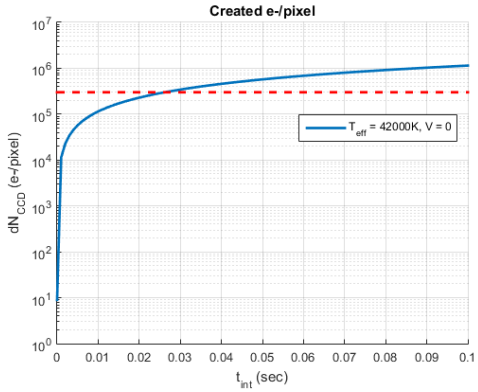


(a) Hot bright star with $V = 0$ and $T_{eff} = 42\ 000K$, mean absorption $A_V = 0.3$.

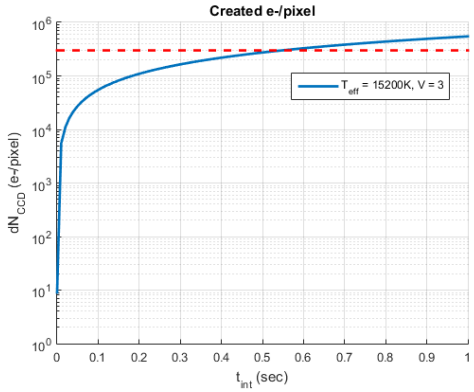


(b) Cold star with $V = 3$ and $T_{eff} = 15\ 200K$, high absorption $A_V = 2.5$.

Figure 4.43: Number of generated $e^-$ on a pixel illuminated by a very hot star considering a mean interstellar absorption (left) and a cooler star considering a high interstellar absorption (right). The horizontal red dashed line corresponds to the full well capacity of the detector.

used in many space missions. However, we know that limitations exist regarding the storage of data on-board and the transfer of data to the ground station. The images related to the same observing block will have to be processed by the OBC using dedicated software.

# Chapter 5

# Feasibility Study of a Low-Resolution UV Spectropolarimeter on-board a Cubesat

## 5.1 Proposed Instrument and Mission

The previous chapter demonstrated that it was feasible to design a small UV telescope, to integrate it into a Cubesat and achieve high level science with it while orbiting in LEO. In the present chapter, we are introducing a new concept of space instrumentation with another main purpose: technology demonstration. The Cubesat standard is still the baseline for the satellite platform because we want to propose a cheap space mission that could be developed relatively quickly.

The proposed instrument is a low-resolution UV spectropolarimeter that, similarly to the project presented in the previous chapter, will observe bright massive stars. It is composed, at the entrance of the instrument, of a telescope that will capture the light from the observed stars. The telescope is highly influenced by the design of the previous chapter. Behind the telescope, a polarimeter, which is the main interest of the project, is placed to modulate the light from the telescope as a function of its polarimetric state. A low-resolution spectrometer is placed behind the polarimeter to disperse the light according to its wavelength and eventually a light sensor ends the instrument.

The spectrometer is planned to work in a low-resolution mode because of the volume constraints inherent to the Cubesat platform. It is not possible to design a telescope with a very large aperture. Thus, the amount of photons captured by the instrument is relatively low and if we want to work with a high resolution spectrometer, we will reduce drastically the SNR per wavelength bin because the dispersion increases. This implies that a compromise between the resolution and the SNR has to be found. Since the instrument is mainly designed as a technology

demonstrator, the science is a secondary objective. Indeed, the spectral resolving power of 100 (*POLA-11*, requirement) or 200 (*POLA-11*, goal) is more typical of spectro-photometers and is clearly not sufficient to search for the signatures of stellar magnetic fields. A possible science application would be the determination of the orbital inclination of short-period massive binaries via the measurement of the variations of the polarization as a function of orbital phase [98]. The spectral information would be very helpful to distinguish among the possible origins of polarization in such systems.

The polarimeter part is a relatively new concept of instrument that contains no moving elements and that is able to measure the entire range of polarimetric states of the light passing through it at once. The concept was proposed by Sparks et al., 2012 [99] and is presented in Section 5.2.1.

Table 5.1 shows the scientific requirements established by the GAPHE working group for this new mission concept. They are heavily inspired by the requirements of Table 4.1 to benefit as much as possible from the work done for the photometer's feasibility study. In order to obtain scientific data sufficiently precise to extract information, the required photometric accuracy *POLA-5* is ten times better than *3U-5*. Indeed, the amplitude of the variations of polarization in massive binaries systems is of the order of 0.1% [98]. Therefore, the accuracy that has to be reached must be better than the information to be measured. *POLA-9* and *POLA-10* add requirements on the measurement of the polarization. Especially, *POLA-9* requires to measure all the Stokes parameters (Q, U and V) which are described in Appendix A. Eventually, *POLA-11* adds a requirement concerning the spectral resolution $R$ that should be achieved thanks to the spectrometer. The resolving power is defined as $R = \frac{\lambda}{\Delta\lambda}$ where $\Delta\lambda$ can be described as the smallest difference in wavelengths that can be distinguished at a wavelength $\lambda$.

| Reference | Parameter | Requirement | Goal |
|---|---|---|---|
| POLA-1 | Spectral range | 2500-3500 Å | 2500-3500 Å |
| POLA-2 | Angular resolution | 15 arcsec | 10 arcsec |
| POLA-3 | Field of view (diameter) | 1° | 2° |
| POLA-4 | Target magnitudes | V≤4 | V≤5 |
| POLA-5 | Photometric accuracy | 0.0001 mag | 0.00005 mag |
| POLA-6 | Typical exposure time | 5 min | 1 min |
| POLA-7 | Mission duration | 2 years | 4 years |
| POLA-8 | Duty cycle | 60% | 75% |
| POLA-9 | Polarization | Stokes QUV | Stokes QUV |
| POLA-10 | Polarization accuracy | 0.1% | 0.05% |
| POLA-11 | Resolving power | 100 | 200 |

Table 5.1: Scientific requirements for the proposed near-UV low-resolution spectropolarimeter.

## 5.2 Optical Design

### 5.2.1 Polarimeter

#### 5.2.1.1 Fundamentals

As it is explained in Appendix A, four values are sufficient to describe the polarimetric state of the light: they are called the Stokes parameters. The first parameter, $I$, is the total intensity of the light beam and can be directly measured via image sensors such as CCDs for example. Parameters $Q$ and $U$ characterize the linear polarization states while $V$ is associated to the circular polarization. While $I$ is a strictly positive parameter, $Q$, $U$ and $V \in [-1, 1]$ by definition (see Appendix A for details).

The Mueller formalism is also introduced in Appendix A for describing how to link the input Stokes parameters of a light beam to the output ones that are actually measured. The Stokes parameters can be put into a Stokes vector $\mathbf{S} = [I\ Q\ U\ V]^T$ and the relation between the measured output vector and the input we want to know is:

$$\mathbf{S}_{out} = \mathbf{M}\ \mathbf{S}_{in} \tag{5.1}$$

In Equation 5.1, the Mueller matrix $\mathbf{M}$ is a $4 \times 4$ matrix that can be calculated as a function of the optical elements composing the instrument. It will be detailed in Section 5.2.1.3. The vector $\mathbf{S}_{out}$, or a part of this vector, can be measured using an imaging sensor. Imaging sensors such as CCDs or CMOS, for example, are only sensitive to the first element of the Stokes vector: the intensity $I$. The goal is then to obtain an expression of the output intensity which depends on the four input Stokes parameters. This goal is achieved thanks to the polarimeter part of the instrument that modulates the state of the input light in order to obtain an output signal containing all the information. In the end, the Mueller matrix in Equation 5.1 must be inverted in order to find the input signal.

There are two main methods for modulating the polarimetric state of the light: temporal modulation and spatial modulation. A modulator using temporal modulation determines the entire polarization state by measuring the light sequentially, generally after moving a part of the polarimeter to modify the modulation scheme [23]. Therefore, several measurements are needed to obtain all Stokes parameters. The spatial modulation of the light generally uses a set of optical elements that produces several beams corresponding to different polarization states, and it measures all the information at once [23]. Systematically, temporal modulators contain moving parts and therefore mechanisms that are to be avoided for space applications. The polarimeter concept we propose to study is thus based on spatial modulation [99].

#### 5.2.1.2 Polarimeter Design

An overview of the polarimeter is presented in Figure 5.1. It consists of a parallelepiped birefringent[1] crystal composed of three wedges glued together and placed in front of a simple linear polarizer. The incoming light from the telescope enters the polarimeter from the left, passing through the birefringent elements before going through the linear polarizer. The modulated light exits the polarimeter on the right and subsequently enters the spectrometer.

Each birefringent wedge in Figure 5.1 is different from the others regarding their fast axes[2] orientation $\beta$ and their apex angles $\theta$. The thickness of the wedges varies along the x-axis direction (vertical direction in Figure 5.1) while the optical axis (black discontinuous line) lies in the z-axis direction. It is demonstrated in [99] and also in [101] that at least two birefringent wedges are needed to measure all the Stokes parameters. These two wedges are in red in Figure 5.1. The central wedge has its fast axis (red discontinuous line) oriented along the optical axis, hence it has no modulation effect on the light coming out of the first wedge. This central wedge could be removed but the point here is to reduce the number of interfaces crystal/air (or vacuum) where losses of photons occur [101].

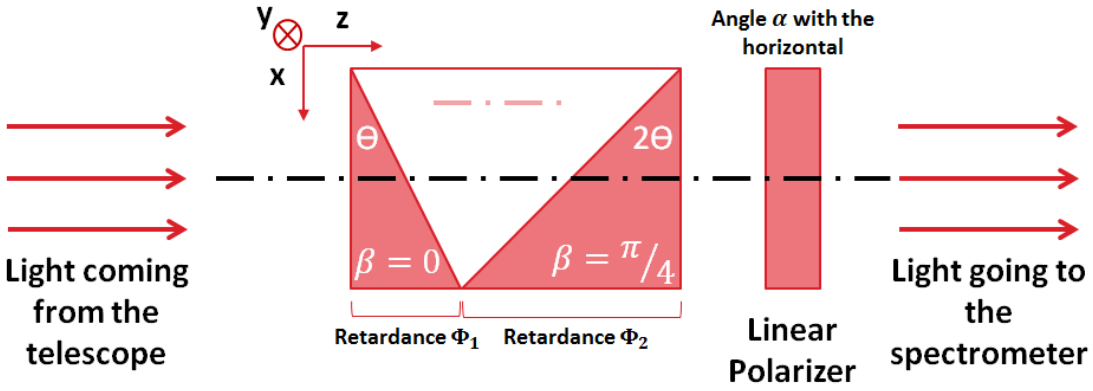


Figure 5.1: Overview of the compact geometry of the polarimeter proposed in [99] and [101].

The red birefringent wedges of Figure 5.1 allow to achieve a spatial modulation of the polarization of the incoming light because they act as retardance plates [99][101].

[1]Birefringence is a characteristics of certain materials that have anisotropic optical properties. In these materials, the refractive index depends on the polarization and the propagation direction of the light. It is well-known that birefringence is responsible for the classical double refraction phenomenon: a light beam entering a birefringent material is split into two distinct beams following different paths (because of a variable retardance of the light for different directions) and having orthogonal polarization states [100].

[2]In a birefringent material, the axis along which the refractive index is the lower is called the fast axis.

The retardance $\Phi$ of a plate of thickness $d$ is given by [101]:

$$\Phi = \frac{2\pi\ \Delta n}{\lambda}\ d \tag{5.2}$$

In Equation 5.2, $\Delta n = n_e - n_o$ is the quantification of the wedges' birefringence and is the maximum difference between refractive indices of the material composing the wedges and $\lambda$ is the wavelength of the light. Note that $\Delta n$ is a function of wavelength [101]. As the thickness $d$ is variable, we have for the two red wedges:

$$\begin{cases} \Phi_1(x,\lambda) = 2\pi\ \tan\theta\ \dfrac{\Delta n(\lambda)\ x}{\lambda} \\ \Phi_2(x,\lambda) = 2\pi\ \tan 2\theta\ \dfrac{\Delta n(\lambda)\ x}{\lambda} \approx 2\Phi_1(x,\lambda) \end{cases} \tag{5.3}$$

The approximation for $\Phi_2$ is valid if $\theta$ is small. This condition is adopted hereafter and is discussed in Section 5.2.1.5. It can be seen from Equation 5.3 that the retardances induced by the two red wedges depend on the wavelength $\lambda$ and the coordinate $x$ referring to the position where the light passes through the system. The calculation of the modulation of the entire polarimeter will be detailed in the next section.

#### 5.2.1.3 Mueller Matrix Calculation

In order to determine the modulation of the light behind the polarimeter, we have to use the Mueller formalism where each optical element is described by a $4 \times 4$ matrix. The two red wedges of Figure 5.1 are considered as spatially variable retarders. The general Mueller matrix for such elements with a retardance $\Phi$ is given by [102]:

$$\mathbf{M}_{retarder} = \begin{pmatrix} 1 & 0 & 0 & 0 \\ 0 & \cos\Phi \sin^2 2\beta + \cos^2 2\beta & (1-\cos\Phi)\cos 2\beta \sin 2\beta & -\sin\Phi \sin 2\beta \\ 0 & (1-\cos\Phi)\cos 2\beta \sin 2\beta & \cos\Phi \cos^2 2\beta + \sin^2 2\beta & \sin\Phi \cos 2\beta \\ 0 & \sin\Phi \sin 2\beta & -\sin\Phi \cos 2\beta & \cos\Phi \end{pmatrix} \tag{5.4}$$

In [101], the fast axis angle of the first wedge is fixed to $\beta = 0°$ (it is aligned with the y-axis direction) while the third wedge has $\beta = \dfrac{\pi}{4}$. These values allow to drastically simplify the general matrix of Equation 5.4 and simultaneously they also allow to obtain a final modulation of the intensity containing all the Stokes parameters as it will be demonstrated in this section. As a reminder, the second wedge, the white one, has its fast axis oriented along the optical axis and acts like a non-birefringent part, i.e. its Mueller matrix is the identity: $\mathbf{M}_2 = \mathbf{I}$. For the other wedges, we can replace the value of $\beta$ in Equation 5.4 and also define $\Phi = \Phi_1$ to simplify the notation. We obtain:

$$\mathbf{M}_1 = \begin{pmatrix} 1 & 0 & 0 & 0 \\ 0 & 1 & 0 & 0 \\ 0 & 0 & \cos\Phi & \sin\Phi \\ 0 & 0 & -\sin\Phi & \cos\Phi \end{pmatrix} \tag{5.5}$$

$$\mathbf{M}_3 = \begin{pmatrix} 1 & 0 & 0 & 0 \\ 0 & \cos 2\Phi & 0 & -\sin 2\Phi \\ 0 & 0 & 1 & 0 \\ 0 & \sin 2\Phi & 0 & \cos 2\Phi \end{pmatrix} \tag{5.6}$$

The last element of the polarimeter is the linear polarizer. The axis of the polarizer, $\alpha$, is defined in the xy plane with the zero along the y-axis represented in Figure 5.1. The Mueller matrix of this kind of ideal element is given by [102]:

$$\mathbf{M}_{polarizer} = \mathbf{M}_4 = \frac{1}{2} \begin{pmatrix} 1 & \cos 2\alpha & \sin 2\alpha & 0 \\ \cos 2\alpha & \cos^2 2\alpha & \cos 2\alpha \sin 2\alpha & 0 \\ \sin 2\alpha & \cos 2\alpha \sin 2\alpha & \sin^2 2\alpha & 0 \\ 0 & 0 & 0 & 0 \end{pmatrix} \tag{5.7}$$

Knowing all the Mueller matrices of the polarimeter, it is possible to calculate the entire matrix $\mathbf{M} = \mathbf{M}_4 * \mathbf{M}_3 * \mathbf{M}_2 * \mathbf{M}_1$ and to obtain the expression of the output Stokes vector $\mathbf{S}_{out}$. As it was specified earlier in this chapter, imaging sensors are only sensitive to the first element of the Stokes vector: the intensity. Therefore, our only interest is relative to the first line of $\mathbf{M}$ which multiplies the input Stokes vector $\mathbf{S}_{in}$. The final result is:

$$\boxed{\begin{aligned} I_{out}(x,\lambda) = \frac{1}{2}(I + [\cos 2\Phi \cos 2\alpha]\ Q + [\sin \Phi \sin 2\Phi \cos 2\alpha + \cos \Phi \sin 2\alpha]\ U \\ + [\sin \Phi \sin 2\alpha - \cos \Phi \sin 2\Phi \cos 2\alpha]\ V) \end{aligned}} \tag{5.8}$$

Equation 5.8 shows that the output intensity that we can measure is a relatively complex combination of the four input Stokes parameters and it depends on $x$ and $\lambda$ thanks to the retardance $\Phi$ of the birefringent wedges. Some parameters of the polarimeter still have to be fixed in order to present simulations of the $I_{out}$ modulation: the angles $\alpha$ and $\theta$ have to be fixed and $\Delta n$ is unknown and is a property of the material composing the birefringent wedges.

#### 5.2.1.4 Material Selection

It is important to take into account two properties in order to select the best material for the wedges:

- The **birefringence** $\Delta n$: the material should have a $\Delta n$ sufficiently high to induce a retardance when a light beam passes through the wedge. The variations of $\Delta n$ should be small in the range 2500-3500 Å of the *POLA-1* requirement. Small variations will result in a smooth dependence on the wavelength which is easier to correct afterwards.

- The **transmittance** $T$ is defined as the efficiency of a material to transmit a light beam. The material should have a transmittance as high as possible in the wavelength range to be covered by the instrument (*POLA-1*).

Two different materials were identified as candidates for the birefringent wedges: Magnesium Fluoride $MgF_2$ and Quartz Crystal $SiO_2$. These two materials are birefringent in the UV domain and especially between 2500 and 3500 Å and they are also transparent at these wavelengths. They have to be compared in order to select the most suitable one for our application.

The first criterion of comparison is relative to $\Delta n$. According to data from *Crystran* [103][104], both materials have nearly constant values of $\Delta n$ over the range of wavelengths considered here. The value for $MgF_2$ is between 0.013 and 0.012, whilst that of $SiO_2$ is somewhat lower, between 0.011 abd 0.010. The marginaly larger value for $MgF_2$ makes this material a slightly better candidate.

In addition, concerning the transmittance, *Crystran* also proposes transmittance curves for samples with different thickness. It can be seen from [103] that the transmittance of $MgF_2$ is over 90% considering a sample thickness of 5 mm. [104], on the other hand, shows a transmittance of $SiO_2$ slightly under 90% but for a sample thickness of 3 mm. This means that for an equal thickness, $MgF_2$ has a slightly higher transmittance than $SiO_2$ in the UV domain.

It appears that $MgF_2$ has two advantages compared to $SiO_2$: its $\Delta n$ is larger and its transmittance is also larger. Anticipating an issue regarding the SNR achievable (Section 5.3.2), $MgF_2$ is selected as baseline material for the wedges design and for the simulations presented in the following section. Indeed, the main advantage of $MgF_2$ is its larger transmittance allowing to maximize the flux passing through the wedges.

#### 5.2.1.5 Simulations

In order to use Equation 5.8 for numerical simulations, two remaining parameters have to be fixed: the apex angle $\theta$ and the orientation of the linear polarizer with respect to the horizontal plane, i.e. $\alpha$.

First, if we analyse Equation 5.8 with respect to $\alpha$, we can see that the angle always appears in $\cos 2\alpha$ and $\sin 2\alpha$ terms. Let's get into the first quadrant just to simplify the reasoning. If $\alpha = 45°$, then $\cos 2\alpha = 0$ and there is no contribution of Q in the equation. If $\alpha = 0°$, then $\sin 2\alpha = 0$ and the modulation of U and V is identical in the expression of $I_{out}$ and are just shifted in the x direction. This solution is not very practical because it makes the discrimination between U and V more difficult. A good choice would be to take $\alpha \approx 30°$ or $\alpha \approx 60°$ in order to differentiate the cosine and sine terms and let the modulation of the Stokes parameters be ruled by the $\Phi$ terms. The final value of $\alpha$ has been fixed to 30° for the simulations.

Second, in [101], the reference apex angle is $\theta = 1.5°$. Figure 5.2 presents $I_{out}$ as calculated in Equation 5.8 and for three different sets of incident Stokes parameters. It can be seen from these results that, for a given wavelength, the output intensity is indeed modulated along the x direction thanks to the variable retardance of the

wedges assembly. The modulation pattern appears really different for each cases. Other values of $\theta$ have been tested with the simulation algorithm providing the results of Figure 5.2. If $\theta$ increases, the modulation pattern is denser because the thickness of the wedges and therefore the retardance $\Phi$ increase. It means that, if we want to catch the modulation of $I_{out}$ with larger $\theta$, the resolving power of the system should be larger, rendering the instrument more complex to design. A smaller value of $\theta$ is therefore preferable. Moreover, if the value of $\theta$ increases, the small angle approximation used for Equations 5.3, 5.6 and 5.8 is not valid anymore, and the full expressions of $\Phi_1$ and $\Phi_2$ must be used instead. In [101], an instrumental breadboard has been designed with manufactured wedges with $\theta = 1.5°$, showing that such a configuration is feasible. We will keep the value of $\theta = 1.5°$ for the design.

With only one integration and without any moving part in the instrument, it is thus possible to register $I_{out}(x, \lambda)$ on a 2D focal plane. For each wavelength $\lambda$, the information relative to the four Stokes parameters is contained along the x direction.

Since we want to precisely register the modulation of the signal along x, the focal plane must contain more than four pixels along this direction. Therefore, while we have four unknowns we will obtain more than four values constraining them: this mathematical problem is overdetermined hence the determination of the Stokes parameters should be done through a classical least-squares solving method.

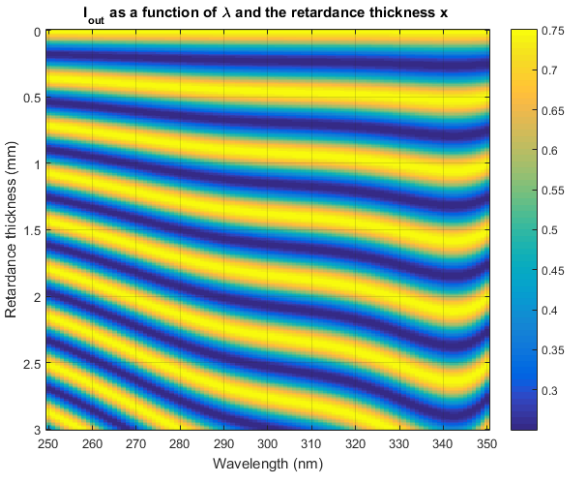


(a) Results for I = 1, Q = 1, U = 0 and V = 0.

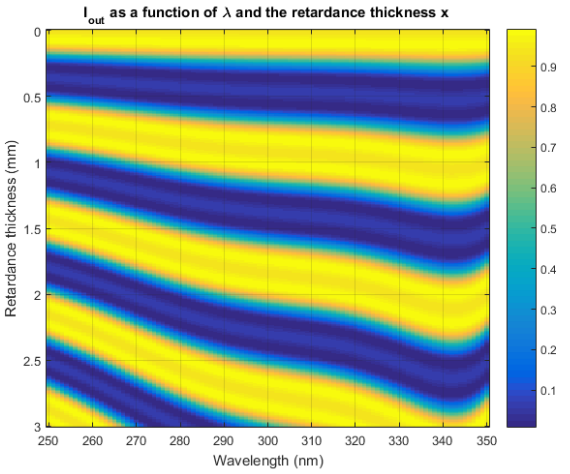


(b) Results for I = 1, Q = 0, U = 1 and V = 0.

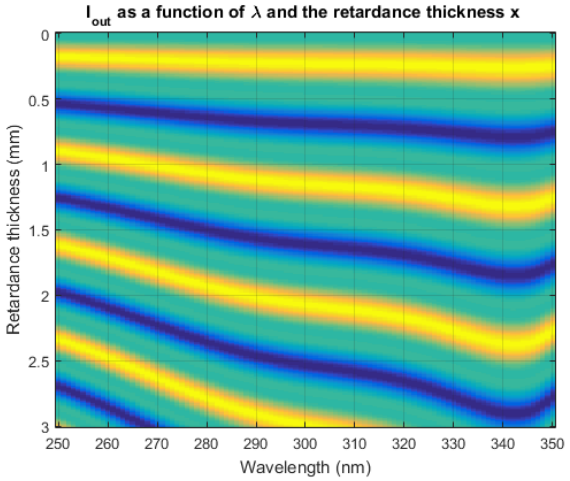


(c) Results for I = 1, Q = 0, U = 0 and V = 1.

Figure 5.2: $I_{out}(x, \lambda)$ for different incident polarimetric cases. The material for the birefringent wedges is $MgF_2$, the apex angle $\theta = 1.5°$, the polarizer angle $\alpha = 30°$ and $x$ varies from 0 (at the top of the wedges) to 3 mm.

### 5.2.2 Telescope

The baseline for the telescope design is the same as the one presented in the previous Chapter 4. As a large amount of work has been done to study the integration of a Ritchey-Chrétien telescope inside a 3U Cubesat, the heritage of this work is used to design a more complex instrument inside a probably larger Cubesat. The baffling system that has been presented in Chapter 4 is also considered as the baseline for the stray light reduction.

### 5.2.3 Spectrometer

For the design of the spectrometer, we minimized as much as possible the number of optical elements in order to increase the SNR as much as possible and to simplify the integration to the Cubesat platform. Figure 5.3 shows the entire optical design of the spectropolarimeter. The telescope images the observed star. After that, the stellar image is collimated with an off-axis spherical mirror which illuminates the polarimeter. The light from the star has to be collimated before entering the polarimeter so that it can cross the same thickness of birefringent material regardless of the coordinate x along the polarimeter height. At this stage, it has to be noted that the off-axis mirror is a source of instrumental polarization that must be considered in the final characterization of the instrument. The simulations described in the previous section have been performed for the polarimeter module alone. For future considerations, the Mueller matrices of the mirrors, and especially of the off-axis mirror, must be integrated to the calculations.

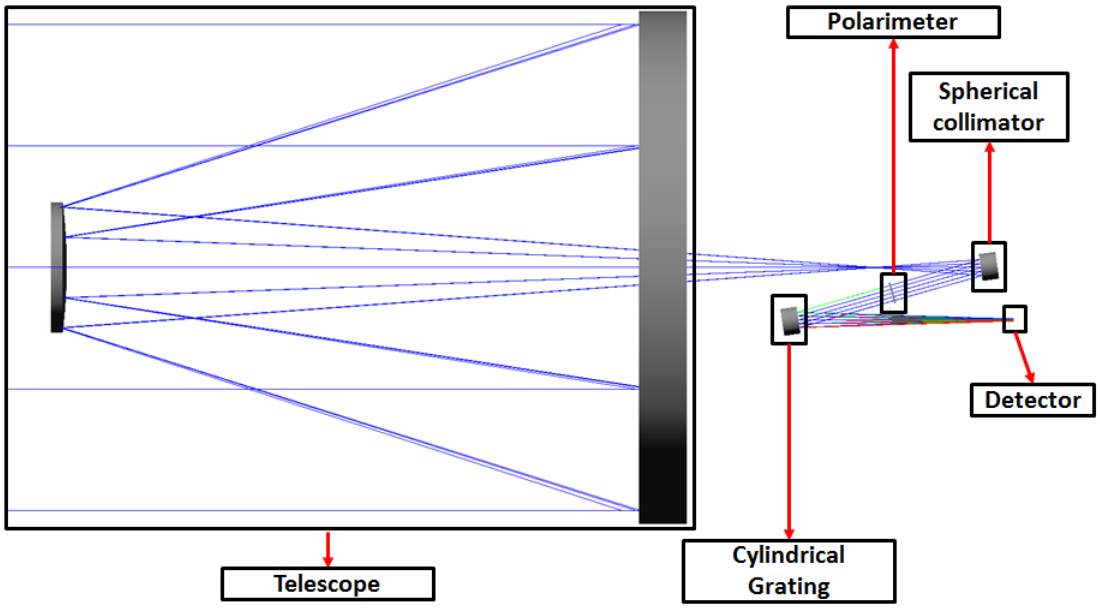


Figure 5.3: Overview of the entire spectropolarimeter composed of a Ritchey-Chrétien telescope at the entrance, a low-resolution spectrometer and a polarimeter.

The polarimeter part is then followed by a diffraction grating to disperse the light with respect to its wavelength and produce a spectrum. It might be noticed that no focusing element follows the diffraction grating because it exhibits a cylindrical shape and is therefore also in charge of focusing the spectrum.

In order to derive the instrumental specifications of the spectrometer part of the instrument, Bingham's methodology is employed [105]. The technique consists in maximizing the instrument figure of merit which incorporates both resolving power and throughput aspects. Scientific requirements are the inputs variables as well as the telescope parameters and the potential mechanical constraints. For example, the angle between the collimator and the camera was forced to adopt the suitable value to align the detector with the telescope axis. The obtained resolving power through the focal plane varies from 105 to 155, which is between the requirement and the goal of *POLA-11*.

## 5.3 Achievable Performances

### 5.3.1 Field of View

It has been briefly discussed in the previous section that the collimated light entering the polarimeter should cross the same thickness of birefringent material in order to correctly modulate the expression of $I_{out}$ in Equation 5.8. Indeed, the modulation along the x-axis is due to the retardance which is known for a given x. If x varies for a given incident beam from the entrance to the exit of the polarimeter, it renders the problem even more complex. The ideal situation is to have a collimated beam which is aligned with the optical axis.

The situation described above poses a fundamental problem to the design of the instrument and of the mission: we are constrained to observe on-axis targets or slightly off-axis ones with the spectropolarimeter. It implies that the requirement *POLA-3* cannot be achieved with such an instrument. Since the requirement proposed in Table 5.1 is mainly an heritage of the requirement *3U-3* presented in Chapter 4, the problem is not considered as critical. However, this has several consequences:

- Since the FoV has to be reconsidered, the optimization constraints that were set in CODE V and that depend on the FoV can be relaxed, and could maybe provide a different solution for the mirrors.
- A mechanical pinhole should be installed at the focal plane of the telescope to select the on-axis light and its close surroundings. The size of the pinhole has to be defined but it cannot be too small. We have to allow small off-axis angles to go through the pinhole and therefore through the polarimeter and spectrometer parts because of the satellite pointing accuracy uncertainty. It has been discussed in the previous chapter that the actual ADCS have limitations. The FleXcore unit is able to achieve a pointing accuracy of $\pm 21.6$

arcsec [64]. The pinhole should be sufficiently wide to cover the pointing uncertainty. A probably better solution is to use piezoelectric actuators that re-position the detector in a way similar to what was implemented on the PicSat experiment described in Chapter 3.

### 5.3.2 Signal to Noise Ratio

The requirement *POLA-5* specifies that the photometric accuracy $\Delta V$ should be at least 0.0001. Using Equation 4.21, we deduce that the SNR should be equal to 10 860 for the requirement and 21 720 for the goal. These values also correspond to observation durations lower or equal to 5 minutes (1 minute for the goal).

In this case, the SNR calculation is more complex than the one presented in Chapter 4. Equations 4.22 and 4.23 are still usable but some parameters have to be redefined because of the dispersion of the instrument with respect to the wavelengths and also to the x direction of the polarimeter. The main changes are listed below:

- The total number of incident photons is still the same at the entrance of the telescope but now the instrument analyses the light according to its wavelength. The number of photons $N$ to be considered corresponds to the integral of $dN$ over a small range $d\lambda$ which is a function of the spectral resolution $R = \frac{\lambda}{d\lambda}$. It is specified in Section 5.2.3 that the resolution $R$ varies from 105 to 155 in the focal plane. The variation is due to the wavelength dependence of $R$. $N$ also varies as a function of the wavelength through the focal plane and its value is much less important than it was in Chapter 4 and it is the main challenge to achieve the requirement *POLA-5* concerning the SNR. It has to be noted that the spectrometer that we proposed works in low resolution because of this constraint. As the aperture of the instrument is small because of the Cubesat platform, we cannot collect a large amount of light of the stars per wavelength bin. A high resolution instrument would decrease $N$ for each considered wavelength $\lambda$ because $d\lambda$ would be smaller.

- The total efficiency of the instrument has to be reassessed because the number of optical elements has increased. There are four mirrors, the polarimeter and the detector. Though this is not represented in Figure 5.3, we also need a filter in front of the detector, as for the instrument of the 3U Cubesat. Therefore the total efficiencies of Equations 4.17 and 4.18 will be lower in this case. Considering the polarimeter composed of $MgF_2$ wedges and a linear polariser with a transmittance efficiency evaluated at 90% and the two additional mirrors with the same characteristics as presented in Section 4.5.4.1, we obtain $\eta_{min,pola} = 4\%$ and $\eta_{max,pola} = 8.5\%$.

- The number of pixels $\#Pix$ has also to be reassessed. First, in the focal plane and along the direction of the wavelength dispersion, the light of a specific wavelength range $\lambda \pm \frac{d\lambda}{2}$ must illuminate at least two pixels because of the

Nyquist frequency constraint [55]. It is represented in Figure 5.4. Then, along the other axis we have the modulation of the light according to the polarisation part. The modulation terms of Equation 5.8 are $\cos 2\Phi$, $[\sin\Phi \sin 2\Phi + \cos\Phi]$ and $[\cos\Phi \sin 2\Phi - \sin\Phi]$. The detector should be large enough to measure the signal over $\Delta\Phi = 2\pi$ and the pixels should be small enough to get two points in the interval $\Phi = [0, \frac{\pi}{2}]$. These considerations lead to the definition of the maximum pixel size corresponding to 180 $\mu$m and the minimum length of the detector along the x-axis corresponding to 1.44 mm. The maximum pixel size is very large compared to off-the-shelf detectors. From e2v [52], the maximum pixel size of their off-the-shelf CCD is 26 $\mu$m hence there is no risk to exceed the limit of 180 $\mu$m. Moreover, the entire x-axis is covered with $\frac{1.44\ mm}{26\ \mu m} = 56\ pixels$. It can be concluded that the light of a given wavelength illuminates $2 * 56 = 112\ pixels$ in the focal plane.

- The number of photons from the sky background $N_{SL}$ is the last parameter to be reassessed. As for $N$, $N_{SL}$ has to be decomposed into small parts corresponding to specific wavelengths.

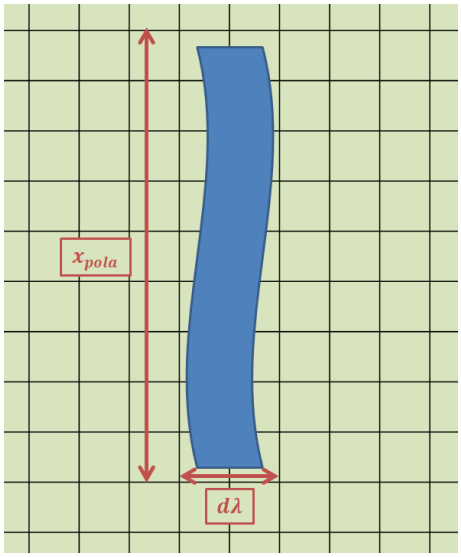


Figure 5.4: Schematic representation of the light of a specific wavelength range illuminating the pixels of the focal plane. The wavelength range of width $d\lambda$ falls onto two pixels along the wavelength axis of the detector. Along the other axis, we have the modulation of the intensity signal due to the polarimeter.

As it is explained above, the SNR calculation is more complex because of the dispersion of the light along two axes in the focal plane. This dispersion leads to a strongly constraining problem. Basically, the signal that we obtain at a given wavelength is strongly reduced compared to the calculations of Chapter 4 because of the double dispersion. In the mean time, the total efficiency of the instrument is also reduced while the noises remain relatively similar except for the background noise

that decreases in the same way as the signal. Therefore, we are in a situation where it is quasi impossible to achieve the SNR required by *POLA-5* while respecting the duration of the observations required by *POLA-6*. In many cases, even considering a mean interstellar absorption $A_V$, several tens of minutes and even several hours are needed to obtain a SNR of 10 860. At this point, it is not conceivable to perform scientific observation of such long duration. An entire orbit or even several orbits in certain cases would be needed for a single observation.

Table 5.2 presents, for several spectral types and magnitudes of stars, the SNR we would achieve within the 5 minutes required by *POLA-6*. As it can be seen, the only case which is compliant with requirement *POLA-5* is the first one with an O5 star with a magnitude $V = 0$. However, as it is specified in Section 4.5.4.3, there is no such star in reality.

| Spectral type | Magnitude $V$ | SNR within 5 min |
|---|---|---|
| O5 | 0 | 11 530 |
| | 1 | 7 040 |
| | 2 | 4 060 |
| | 3 | 2 200 |
| | 4 | 1 060 |
| | 5 | 470 |
| B0 | 0 | 8 920 |
| | 1 | 5 350 |
| | 2 | 3 000 |
| | 3 | 1 520 |
| | 4 | 700 |
| | 5 | 306 |
| B5 | 0 | 5 580 |
| | 1 | 3 160 |
| | 2 | 1 610 |
| | 3 | 750 |
| | 4 | 310 |
| | 5 | 130 |

Table 5.2: SNR for several spectral types and magnitudes of stars. The SNR corresponds to what is achievable within 5 minutes as required in *POLA-6*. For each case, the wavelength $\lambda$ is selected to have the minimum value of $N$ and the intensity $I_{out}$ is assumed to be constant along the polarisation modulation direction for simplifying the analysis (it corresponds to a non-polarized scenario).

The instrument as adapted from the design of the previous chapter cannot meet the requirements defined in Table 5.1. However, there are several ways to improve the instrument, especially if we accommodate it to a larger Cubesat platform (larger than the 3U). A larger platform would allow the following modifications:

- It would be possible to increase the entrance pupil of the telescope to collect more photons.

- It would be possible to accommodate the thermal design of the satellite to decrease the temperature of the detector, hence reducing the dark noise. A larger platform would allow to increase the radiator area, maximizing the heat flux transferred to cold space. It is also possible to imagine working with an active cooling system because with a larger platform we have more room, more mass and also more power available.

## 5.4 Proposed Cubesat Platform

The analysis of the spectropolarimeter shows that the instrument design in the current state is not robust enough for the initially proposed scientific requirements. It was demonstrated that the achievable SNR is too low and cannot achieve the requirement *POLA-5* within decent integration times (*POLA-6*). Further calculations for the SNR showed that even a telescope with an effective diameter of 30 cm, comparable to the OM on-board XMM-Newton, was not able to meet the specifications. Moreover, the problem of the restriction of the FoV cannot be ignored since it drastically reduces the information that could be captured by the satellite. Several pinholes could also be placed at the telescope focal plane to select different off-axis angles. The sizes of the collimating mirror should then be increased to catch these off-axis angles and several polarimeter parts should be assembled with specific angles for each incoming collimated beam. It would also increase the size of the grating, the detector and the space between each optical elements to avoid any vignetting. Therefore, the modifications to be made to reach the specifications finally lead us to consider a massive and voluminous instrument which is outside of the Cubesat standard. However, the main objective that was discussed at the beginning of this chapter is the technology demonstration. It is possible to redefine much lower requirements in order to focus the design only on the demonstration aspect, leaving the scientific objectives for another future mission that could benefit from the qualification of the instrument. Therefore, it could be possible to accommodate the current design to place it inside a 3U Cubesat similar to the one presented in Chapter 4.

An alternative, if technology demonstration is not enough to justify an entire mission, would be to define another kind of scientific mission. The previous chapter demonstrated the feasibility of a 3U Cubesat embarking a photometer and responding to its requirements. Moreover, the SNR calculations for the photometer also demonstrated that we have, in many observation cases, some margins with respect to the requirements. It is therefore conceivable to imagine adapting this 3U Cubesat to a larger platform and add a secondary payload which would be the current version of the spectropolarimeter or a more mature and more efficient version of it. Figure 5.5 proposes a block diagram structure of a 6U Cubesat containing the two payloads. The telescope is followed by a beam splitter plate that divides the light from the telescope into two separate beams, one transmitted to the spectropolarimeter part on the right and the other reflected to the CCD below (photometer part). It must be stressed though that adding a beam splitter in the design would introduce another source of instrumental polarization that needs to be accounted

for. Off-the-shelf beam splitter are usually proposed with specific ratios of transmittance and reflectance that depend on the wavelength (Figure 5.6). The sub-units are inherited from the design of the 3U Cubesat for the photometer and it is evaluated that approximately one unit is free to accommodate redundant systems such as an additional OBC or additional batteries to improve the power storage and the power available at every moment.

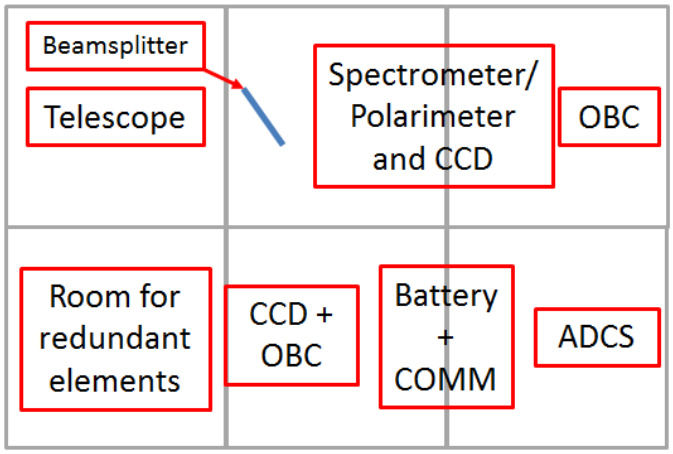


Figure 5.5: Block diagram of the proposed 6U Cubesat embarking a near-UV photometer as primary payload and a near-UV low-resolution spectropolarimeter as secondary payload.

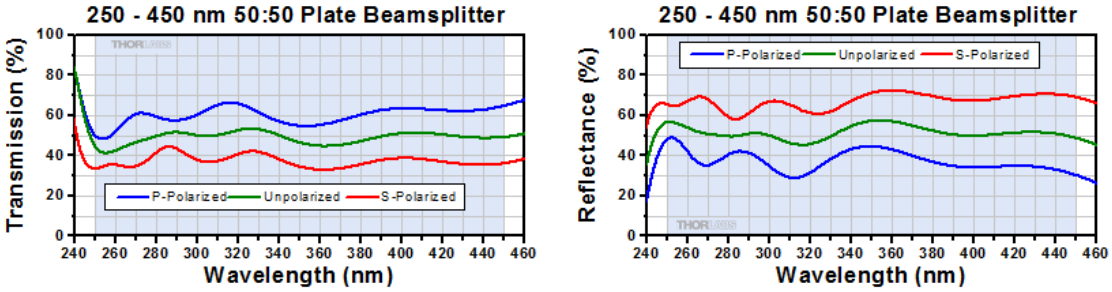


Figure 5.6: Transmittance (left) and reflectance (right) of a 50:50 beam splitter plate from Thorlabs [106].

Of course, considering the problems discussed in Section 5.3, it seems obvious that the spectropolarimeter proposed as secondary payload will still not be able to reach relatively high level scientific requirements as presented in Table 5.1. However, its usefulness would be to demonstrate its performance in the most favourable cases where the observed stars are the brightest and hottest. This configuration allows to combine the technology demonstration aspect of the polarimeter module with the scientific aspect presented in Chapter 4.

# Part III

# Conclusions and Perspectives

# Chapter 6

# Conclusions and Perspectives

## 6.1 PART I: Preparation of an On-board Calibration Unit Concept for a Major Space Mission

### 6.1.1 On-board Calibration Principles

As it was mentioned at the beginning of Chapter 1, there is no unique method for the calibration of an instrument. It always depends on the type of instrument that needs calibration, its required performances, its lifetime and so on.

Based on research relative to previous successful missions, heritage of calibration modules designed at CSL and on literature dedicated to the calibration of space instruments, it was possible to draw up a short list of essential elements of an in-flight calibration unit in Chapter 1. The elements and solutions that were presented were used afterwards in Chapter 2.

### 6.1.2 Application to the Arago Mission for the M4 and M5 Calls from ESA

In Chapter 2, the elements of Chapter 1 were assembled in order to build a calibration assembly that can meet the needs of a very complex instrument such as that of the Arago mission. As a reminder, Arago proposed a telescope feeding a polarimeter and two high-resolution spectrographs that cover a very wide range of wavelengths. The mission was proposed at the end of 2016 for the ESA call M5 after more than two years of preparation in pre-phase A. During this pre-phase A, I worked, in collaboration with colleagues from the KUL, on the design of the proposed calibration unit presented in this second chapter. However, other missions were preferred for the short-list selection of the ESA call. This was mainly because the mission was evaluated too expensive for the M5 budget. Whether or not Arago will be proposed in response to ESA's call for a sixth medium class mission (M6) will depend on the budget available for M6.

Despite this context, the work performed in this thesis during the pre-phase A study of Arago is not wasted. Indeed, other future space missions where the

GAPHE/CSL and/or the KUL would be involved could benefit from the preliminary design proposed in Chapter 2 and thus save time in the early stages of design. Currently, there are two possibilities. The first one is to propose Arago for M6 if the available budget is sufficient. The second possibility is to contribute to the Large UV/Optical/Infrared Surveyor (LUVOIR) mission proposed to NASA [4]. LUVOIR is a mission concept for a highly capable multi-wavelength space observatory with several science goals from the study of galaxy formation and evolution to solar system remote sensing while also characterizing a wide range of exoplanets. LUVOIR is one of four Decadal Survey Mission Concept Studies initiated in January 2016 and it will be prepared for the 2020 Decadal Survey by the Goddard Space Flight Center. Since the termination of this thesis, CSL has been involved in the preliminary design of the calibration unit of the POLLUX instrument, a UV spectropolarimeter proposed for LUVOIR. The design of the in-flight calibration unit is heavily inspired by the design presented in Chapter 2 and there is no doubt that it will be optimized in a relatively short future. The next steps regarding the calibration unit design are the following:

- The output of the instrument, at the detector level, while in calibration mode, has to be quantified to validate the use of only three different lamps.
- The problem of the aging of the lamps has to be studied in details to determine if a single redundant lamp is sufficient or not.
- The mechanisms should be fully defined and their qualification plan should be established as early as possible in the next phase of the project.

## 6.2 PART II: Very Small Missions Feasibility Studies

### 6.2.1 Cubesats Missions

Chapter 3 presented and summarized the Cubesat standard. This is still a very young concept in the space industry but it has already proven its worth thanks to the projects of universities all over the world which see it as an educative mean. That chapter also presented several Cubesat missions which are dedicated to astrophysics research. Unfortunately, there are only a few such projects to present because the discipline of astrophysics is not yet very popular in the field of Cubesats. However, the success of ongoing missions is very important to encourage funding for future innovative missions.

### 6.2.2 Feasibility Study of a UV Photometer On-board a 3U Cubesat

In Chapter 4, the design of a UV photometer on-board a 3U Cubesat was performed and it was demonstrated that it fulfils the scientific requirements.

The optical layout of the photometer was designed, with an optimization driven by the volume limitations that the Cubesat platform imposes. Moreover, in order to increase the performances of the imager, a baffling system has been designed and a stray light analysis was performed to quantify its effect. The system overview presented the choice of the solar panels configuration. The table configuration was preferred over the cross one for the mission because it offers more opportunities for observation. The choice of the detector of the payload was also presented, comparing the current technologies for the detection of UV light. A CCD detector was chosen because of its high efficiency and the maturity of the technology. Discussions relative to the storage and the transfer of the scientific data and to the attitude control concluded the system overview.

A mission analysis was also presented in this chapter. Depending on the orbit, a thermal analysis was performed based on the environmental constraints. The results of the thermal analysis showed that there are no critical points that cannot be solved. During the worst cold case, the structure of the satellite reaches too cold temperature. Two solutions have been mentioned to counter this problem. One of them was to use one or more heaters to heat up the too cold parts of the structure, using the power available thanks to the margins. During the worst hot case, the ADCS exceeds its maximum temperature by 1°C. Knowing that we do not have a detailed model of the ADCS, we expect that its temperature map could be improved and that we could decrease the security margins. One of the important results of the thermal analysis is the definition of the detector temperature, hence defining the dark noise for the photometric budget. The thermal considerations also led to the establishment of a power budget directly associated to the performances of the solar panels. The budget proved that the power consumption is not a critical point for the mission considering current COTS.

The photometric budget allowed to verify that the optimized design is able to observe, most of the time, the stars we are interested in. Due to noise, mostly associated with the sky background, it is not possible to observe the fainter stars in the most pessimistic configuration. However, it was demonstrated that in more realistic situations, we meet the requirements for all the selected targets. A perspective, mentioned in the stray light analysis section, for achieving a better budget would be to design a deployable baffle in front of the current telescope aperture to block the light coming from high off-axis angles. It has also been presented that in realistic observation cases, the pixels of the detector saturated very quickly and therefore we have to cut the data acquisition in several small integrations that have to be combined afterwards. This problem could be partially resolved by defocusing the telescope to increase the size of the spots on the focal plane. This way, more pixels would be illuminated by the starlight and the saturation issue would appear less quickly. The defocusing of the telescope could also be a solution to compensate the attitude determination uncertainty discussed in the system overview, simplifying the observation versus pointing problem.

At this stage of the conception, it can be concluded that a very large part of the

payload and system studies have been made. However, several points still have to be addressed:

- A mechanical analysis of the system must be done in order to validate the current design for launch. A detailed mass budget has also to be defined for this analysis. At this stage, the overall mass budget is estimated at 3.6 kg but it has to be consolidated.
- It has to be assessed if a deployable stray light baffle sufficiently reduces the sky background noise to justify the study and the implementation of this solution to the current design.
- The impact of the defocusing of the telescope has to be evaluated.
- The ground segment requirements need to be evaluated.

Eventually, a rough estimation of the cost of the satellite components (payload and sub-systems) is 175 000 €. It does not take into account other important aspects such as qualification tests, commissioning, launch, ground operation during the mission. Even if this budget seems very low regarding small/medium/large missions of space agencies (ESA, NASA), it is already a big budget for a single university institute. The concrete realization of such a project requires a sponsor or an association with different partners. In this context, first contacts with Polish colleagues have recently been established.

### 6.2.3 Feasibility Study of a Low-Resolution UV Spectropolarimeter on-board a Cubesat

Chapter 5 presented the concept of a spatially modulated polarimeter able to measure the entire polarimetric state of the light, i.e. all the Stokes parameters. The advantage of this polarimeter is that it could easily be associated to a spectrometer to analyse the light with respect to its wavelength.

The mission which was proposed in this chapter was built on the heritage of Chapter 4. However, it was demonstrated that the limitations of the Cubesat platforms strongly restrict the achievable performances of the instrument which is not able to meet the scientific requirements defined and discussed at the beginning of the chapter. Some solutions were proposed in Chapter 5 to improve the performances of the instrument. Technically, these solutions can be summarized as follows: use a larger platform (possibly larger than a Cubesat), to downgrade the scientific specifications, or to propose a 6U Cubesat with two payloads, based on the design and analyses developed in Chapter 4.

It has to be assessed which solution is the best. Regardless of the selected solution, there remains a lot of work to do regarding the understanding and the simulation of the entire instrument (from the telescope to the detector). Especially, the instrumental polarization is not an easy problem to solve and current optical engineering software are not designed to handle it correctly. It is also expected that

the spectropolarimeter is more sensitive to external disturbances. Therefore, the impact of noises such as the jitter noise should be studied.

## 6.3 General Conclusion

The current thesis has proposed to study very different aspects of space instrumentation, from the design of a single instrument unit for a large mission to the optical and system engineering of an entire small satellite. The subject that binds all this is the observation from space in the UV domain. At our level, the scientists involved in the definition of this thesis are mainly interested by the study of the properties of massive stars. However, as demonstrated by the large international scientific consortium supporting the Arago or LUVOIR projects, there is a broad interest in UV astrophysics that goes well beyond the topic of massive stars. There is clearly a strong scientific motivation for a large, dedicated UV astrophysical observatory.

Meanwhile, as demonstrated in this thesis, Cubesats can pave the way towards the next generation of large UV observatories, both scientifically and to raise the technology readiness level of critical components. Indeed, UV photometry of relatively bright sources could be obtained easily with a 3U Cubesat. A small satellite could also be used in preparation of the UV spectropolarimeter foreseen for Arago or LUVOIR. As pointed out above, the accommodation of a Sparks polarimeter aboard a small satellite requires further optimization, though our preliminary study revealed no fundamental show stopper. Regarding the small satellites, it remains to be seen what is the most promising strategy (a science-driven project funded by governmental agencies or a technology-driven project partially funded by industrial sponsors, or a combination of both) to raise the funds needed for the hardware developments that would be required to implement either or both of the Cubesats projects discussed in this thesis work. Yet, although this work has demonstrated the limitations of Cubesats for more sophisticated missions, it has also highlighted the tremendous possibilities that are offered by such small satellites to perform innovative scientific measurements.

# Bibliography


[1] NASA Goddard Space Flight Center. James Webb Space Telescope. https://www.jwst.nasa.gov/. Accessed: 04/04/2018.

[2] ESA. SPICA: a SPace Infrared telescope for Cosmology and Astrophysics. http://sci.esa.int/cosmic-vision/53635-spica/. Accessed: 04/04/2018.

[3] Huber M., Pauluhn A., Timothy J., and Zehnder A. *Calibration*, pages 629–638. 2013.

[4] Goddard Space Flight Center. Large UV/OpticalInfrared Surveyor. https://asd.gsfc.nasa.gov/luvoir/. Accessed : 28/09/2017.

[5] California Polytechnic State University. The CubeSat Program. http://www.cubesat.org/. Accessed: 10/05/2017.

[6] Munakata R. *CubeSat Design Specification*. California Polytechnic State University, 2009.

[7] Long M., Lorenz A., and Rodgers G. et al. A Cubesat derived design for a unique academic research mission in earthquale signature detection. In *16th Annual/USU Conference on Small Satellites*, Logan, Utah, 2002. Reference: SSC02-IX-6.

[8] Noca M. and Ivanov A. SwissCube Status. Document available at: http://swisscube.epfl.ch/, 2010.

[9] Weiss W. W., Rucinski S. M., and Moffat A. F. J. et al. BRITE-Constellation: Nanosatellites for Precision Photometry of Bright Stars. *Publications of the Astronomical Society of the Pacific*, 126:573–585, 2014.

[10] Norton C. D., Pellegrino S., and Johnson M. et al. Small satellites: a revolution in space science. Technical report, Keck Insitute for Space Studies, July 2014.

[11] ESA. Sentinel-3. http://www.esa.int/Our_Activities/Observing_the_Earth/Copernicus/Sentinel-3. Accessed: 12/07/2017.

[12] Plesseria J. Y. Olci Test. http://www.csl.ulg.ac.be/jcms/c_7333/en/olci-test. Accessed: 12/07/2017.

[13] ESA. Sentinel-4. https://earth.esa.int/web/guest/missions/esa-future-missions/sentinel-4. Accessed: 13/07/2017.

[14] Davidson M. Tungsten-Halogen Incandescent Lamps. http://zeiss-campus.magnet.fsu.edu/articles/lightsources/tungstenhalogen.html. Accessed: 20/07/2017.

[15] Wikipedia. Deuterium arc lamp. https://en.wikipedia.org/wiki/Deuterium_arc_lamp. Accessed: 26/07/2017.

[16] Wikipedia. Hollow-Cathode Lamp. https://simple.wikipedia.org/wiki/Hollow-cathode_lamp. Accessed: 20/07/2017.

[17] Kerber F., Bristow P., and Rosa M. et al. Characterization of Pt-Cr-Ne Hollow-CathodeLamps for Wavelength Standards in Space Astronomy. In *The 2005 HST Calibration Workshop*, pages 318–323, 2005.

[18] Pascucci I., Proffitt C., and Ghavamian P. et al. Monitoring of the Wavelength Calibration Lamps for the Hubble Space Telescope. In *The 2010 STScI Calibration Workshop*, pages 439–448, 2010.

[19] Nariai K. Mass Loss from Coronae and its effect upon Stellar Rotation. *Astrophysics and Space Science*, 3:150–159, 1969.

[20] François P., Matteucci F., and Cayrel R. et al. The evolution of the Milky Way from its earliest phases: Constraints on stellar nucleosynthesis. *Astronomy and Astrophysics*, 421:613–621, 2004.

[21] Rusomarov N., Kochukhov O., Ryabchikova T., and Piskunov N. Three-dimensional magnetic and abundance mapping of the cool Ap star HD24712. *Astronomy and Astrophysics*, 573:A123, 2015.

[22] Baudrand J. and Bohm T. MUSICOS: a fiber-fed spectrograph for multi-site observations. *Astronomy and Astrophysics*, 259:711–719, 1992.

[23] Keller C. U. Instrumentation for Astrophysical Spectropolarimetry. In *Astrophysical Spectropolarimetry*, pages 303–354. Cambridge University Press, 2001.

[24] Thorlabs. Quartz Tungsten Halogen Lamp. https://www.thorlabs.de/newgrouppage9.cfm?objectgroup_ID=7541. Accessed: 02/08/2017.

[25] ESA. SCIAMACHY Product Handbook. https://earth.esa.int/web/guest/missions/esa-operational-eo-missions/envisat/instruments/sciamachy-handbook/wiki/-/wiki/SCIAMACHY%20Handbook/FrontPage. Accessed: 02/08/2017.

[26] Dever J., Pietromica A., and Stueber T. et al. Simulated Space Vacuum Ultraviolet (VUV) Exposure Testing for Polymer Films. *39th Aerospace Sciences Meeting and Exhibit*, 2001.

[27] Fox A. Cosmic Origins Spectrograph Instrument Handbook for Cycle 25. Technical report, Space Telescope Science Institute, 2017.

[28] Kerber F., Bristow P., and Rosa M. STIS Calibration Enhancement (STIS-CE): Dispersion Solutions Based on a Physical Instrument Model. In *The 2005 HST Calibration Workshop*, pages 309–317, 2005.

[29] Argyriou I. Personal communication.

[30] Bever R., Ruitberg A., Kellenbenz C., and Irish S. High Voltage Power Supply Design Guide for Space. Technical report, NASA, 2006.

[31] Wikipedia. Transformer. `https://en.wikipedia.org/wiki/Transformer`. Accessed: 26/09/2017.

[32] Swartwout M. The First One Hundred CubeSats: A Statistical Look. *Journal of Small Satellites*, 2:213–233, 2013.

[33] Cahoy K. CubeSats in Astronomy and Astrophysics. In *SSB CubeSat Symposium - Irvine, CA*, 2015.

[34] Ardila D., Shkolnik E., and Gorjian V. CubeSats for Astrophysics: The Current Perspective. *American Astronomical Society Meeting*, 229, 2017.

[35] Pablo H., Whittaker G.N., and Popowicz A. et al. The BRITE Constellation Nanosatellite Mission: Testing, Commissioning and Operations. *Publications of the Astronomical Society of the Pacific*, 128:125001, 2016.

[36] Canadian Space Agency. The BRITE Constellation. `http://www.asc-csa.gc.ca/eng/satellites/brite/`. Accessed: 31/10/2017.

[37] eoPortal. CXBN-2 (Cosmic X-ray Background Nanosatellite-2). `https://directory.eoportal.org/web/eoportal/satellite-missions/c-missions/cxbn-2`. Accessed: 31/10/2017.

[38] Byeloborodov Y. 2U Cubesat structural design and integration, 2017. Master Thesis presented to the Faculty of the College of Science, Morehead State University.

[39] Jet Propulsion Laboratory. Arcsecond Space Telescope Enabling Research in Astrophysics ASTERIA. `https://www.jpl.nasa.gov/cubesat/missions/asteria.php`. Accessed: 01/11/2017.

[40] Smith M., Seager S., and Pong C. et al. ExoplanetSat: detecting transiting exoplanets using a low-cost cubeSat platform. 2010.

[41] Nowak M., Lacour S., and Lapeyrère V. et al. A Compact and Lightweight Fibered Photometer for the PicSat Mission. In *31st Annual/USU Conference on Small Satellites*, Logan, Utah, 2017. Reference: SSC17-VI-01.

[42] PicSat Team. PicSat mission website. `https://picsat.obspm.fr`. Accessed: 10/04/2018.

[43] Kaaret P. HaloSat Overview, 2016.

[44] Gomez de Castro A. I., Appourchaux T., and Barstow M. A. et al. Building galaxies, srars, planets and the ingredients for life between the stars: the science behind the European Ultraviolet-Visible Observatory. *Astrophysics and Space Science*, 354:229–246, 2014.

[45] Mason K. O., Breeveld A., and Much R. et al. The XMM-Newston optical/UV monitor telescope. *Astronomy and Astrophysics*, 365:L36–L44, 2001.

[46] Handler G. Asteroseismology. In T. Oswalt and M. Barstow, editors, *Planets, Stars and Stellar Systems Volume 4: Stellar Structure and Evolution*, pages pp. 207–241. Springer Netherlands, 2013.

[47] Blomme R., Briquet M., and Degroote P. et al. CoRoT Observations of O Stars: Diverse Origins of Variability. *Astronomical Society of the Pacific Conference Series*, 465:13–18, 2012.

[48] Davenport J. R. A. The Kepler catalog of stellar flares. *The Astrophysical Journal*, 829:23–34, 2016.

[49] NSF-NASA. CubeSat-Based Science Missions for Geospace and Atmospheric Research. Technical report, NASA, 2013. National Science Foundation (NSF) Annual Report.

[50] Kitchin C. R. *Telescopes and Techniques*. Springer Verlag (New-York), third edition, 2013.

[51] Wilson R. N. *Reflecting Telescope Optics I*. Springer Verlag (Berlin), second edition, 2004.

[52] e2v. CCD Image Sensors for Space and Ground-based Astronomy. `http://www.e2v.com/products/imaging/ccd-image-sensors-for-space-and-ground-based-astronomy/`. Accessed: 19/05/2017.

[53] Schott. Schott, glass made of ideas. `http://www.schott.com/france/french/index.html`. Accessed: 23/05/2017.

[54] UQG Optics. Schott UG11. `http://www.uqgoptics.com/materials_filters_schott_uvTransmitting_UG11.aspx`. Accessed: 23/05/2017.

[55] Fischer R., Tadic-Galeb B., and Yoder P. *Optical System Design*. Spie Press, second edition, 2008.

[56] Terebizh V. Yu. Optimal Baffle Design in a Cassegrain Telescope. *Experimental Astronomy*, 11:171–191, 2001.

[57] Persky M. J. Review of black surfaces for space-borne infrared systems. *Review of Scientific Instruments*, 70:2193–2217, 1999.

[58] Roach F. E. The light of the night sky: Astronomical, Interplanetary and Geophysical. *Space Science Reviews*, 3:512–540, 1964.

[59] Leinert Ch., Bowyer S., and Haikala L. K. et al. The 1997 reference of diffuse night sky brightness. *Astronomy and Astrophysics Supplement*, 127:1–99, 1998.

[60] Gondhalekar P. M., Phillips A. P., and Wilson R. Observations of the Interstellar Ultraviolet Radiation Field from S2/68 Sky-survey Telescope. *Astronomy and Astrophysics*, 85:272–280, 1980.

[61] ISIS Space. Products. `https://www.isispace.nl/products/`. Accessed: 13/06/2017.

[62] Clyde Space. 3U Double-Deployed Solar Array. `https://www.clyde.space/products/26-3u-doubledeployed-solar-array`. Accessed: 13/06/2017.

[63] GOMSpace. Products. `http://www.gomspace.com/index.php?p=products`. Accessed: 13/06/2017.

[64] Blue Canyon Technologies. Attitude control systems. `http://bluecanyontech.com/xact/`. Accessed: 13/06/2017.

[65] Rauw G. Beta angle and sky visibility computation. Internal document.

[66] Romanishin W. *An Introduction to Astronomical Photometry Using CCDs*. University of Oklahoma, 2006.

[67] Hamamatsu Photonics. *Image Sensors Selection Guide*, 2017.

[68] Nikzad S., Hoenk M., and Grunthaner P. et al. Delta-doped CCDs for enhanced UV performance. *Proc. SPIE*, 2278, 1994.

[69] Defise J.M. *Analyse des performances instrumentales du télescope spatial EIT*. PhD thesis, Université de Liège, 1999.

[70] Nota A., Jedrzejewski R., Voit M., and Hack W. Faint Object Camera Instrument Handbook. Technical report, Space Telescope Science Institute, 1996.

[71] Avila R. et al. Advanced Camera for Surveys Instrument Handbook for Cycle 25. Technical report, Space Telescope Science Institute, 2017.

[72] Quach A. Complementary Metal-Oxide Semiconductor Sensors. Technical report, University of California Santa Barbara, 2010.

[73] Berghmans D., Hochedez J.F., and Defise J.M. et al. SWAP onboard PROBA 2, a new EUV imager for solar monitoring. *Advances in Space Research*, 38:1807–1811, 2006.

[74] Barnstedt J. Microchannel plate detectors. Technical report, University of Tübingen, 2016.

[75] Michael J. and Karovska M. Chandra's Ultimate Angular Resolution: Studies of the HRC-I Point Spread Function. *American Astronomical Society*, 41:722, 2010.

[76] Holland S.T. et al. Cosmic Origins Spectrograph Instrument Handbook. Technical report, Space Telescope Science Institute, 2014.

[77] e2v Technologies. CCD47-20 NIMO Back Illuminated. `https://www.e2v.com/resources/account/download-datasheet/3713`. Accessed: 19/10/2017.

[78] ISIS Space. ISIS On Board Computer. `https://www.isispace.nl/product/on-board-computer/`. Accessed: 19/10/2017.

[79] GOMSpace. NanoCom AX100. `https://gomspace.com/Shop/subsystems/communication/nanocom-ax100.aspx`. Accessed: 19/10/2017.

[80] GOMSpace. NanoCom ANT430. `https://gomspace.com/Shop/subsystems/communication/nanocom-ant430.aspx`. Accessed: 19/10/2017.

[81] Blue Canyon Technologies. FleXcore Datasheet. `http://bluecanyontech.com/wp-content/uploads/2017/03/DataSheet_Flexcore_05.pdf`. Accessed: 20/10/2017.

[82] Watson E. Sun-synchronous orbit slot architecture analysis and developement. Master's thesis, California Polytechnic State University, 2012.

[83] Berckmans N. Preliminary Thermal Design of a CubeSat, 2017. Master Thesis presented to the Faculty of Applied Sciences, University of Liège.

[84] Rochus P. and Salvador L. Spacecraft payload design: Thermal Control, October 2012.

[85] Gilmore D. *Spacecraft Thermal Control Handbook. Volume I: Fundamental Technologies*. The Aerospace Press, 2002.

[86] GOMSpace. NanoPower P31u. `https://gomspace.com/Shop/subsystems/power-supplies/nanopower-p31u.aspx`. Accessed: 15/11/2017.

[87] Clark C. and Kirk S. Off-the-Shelf, Deployable Solar Panels for CubeSats. `http://mstl.atl.calpoly.edu/~workshop/archive/2012/Spring/33-Clark-Solar_Panels.pdf`. Accessed: 17/11/2017.

[88] Drilling J. and Landolt A. Normal Stars. In *Allen's astrophysical quantities*, page 381. New York: AIP Press, 2000.

[89] Rauw G. Assessment of the performances of optical blocking filters for X-IFU observations of massive stars. Technical report, University of Liège, 2016.

[90] Rauw G. Atmosphères stellaires, 2013-2014.

[91] Teays T. Ultraviolet Astronomy. In *Allen's astrophysical quantities*, page 169. New Yorl: AIP Press, 2000.

[92] Puls J., Vink J.S., and Najarro F. Mass loss from hot massive stars. *The Astronomy and Astrophysics Review*, 16:209–325, 2008.

[93] Ryter Ch. Interstellar Extinction from Infrared to X-Rays: an Overview. *Astrophysics and Space Science*, 236:285–291, 1996.

[94] Yale University Observatory. Yale Bright Star Catalog. `http://tdc-www.harvard.edu/catalogs/bsc5.html`. Accessed: 21/11/2017.

[95] Melles Griot. Optical Coatings. In *Material Properties*. Melles Griot, 2009.

[96] Schroeder J. *Astronomical Optics*. Academic Press, 1987.

[97] Burt D., Endicott J., and Jerram P. et al. Improving radiation tolerance in e2v CCD sensors. In *Proc. SPIE Astronomical and Space Optical Systems*, volume 7439, 2009.

[98] Berdyugin A., Piirola V., and Sadegi S. et al. High-precision broad-band linear polarimetry of early type binaries. *Astronomy and Astrophysics*, 591:A92, 2016.

[99] Sparks W., Germer T., MacKenty J., and Snik F. Compact and robust method for full Stokes spectropolarimetry. *Applied Optics*, 51:5495–5511, 2012.

[100] Wikipedia. Birefringence. `https://en.wikipedia.org/wiki/Birefringence`. Accessed: 07/11/2017.

[101] Pertenais M., Neiner C., and Bernardi P. et al. Static spectropolarimeter concept adapted to space conditions and wide spectrum constraints. *Applied Optics*, 54:7377–7386, 2015.

[102] Chipman R. Polarimetry. In Bass M., editor, *Handbook of Optics II*, pages 22.1–22.37. 1995.

[103] Crystran. Magnesium Fluoride (MgF2). `https://www.crystran.co.uk/optical-materials/magnesium-fluoride-mgf2`. Accessed: 08/11/2017.

[104] Crystran. Quartz Crystal (SiO2). `https://www.crystran.co.uk/optical-materials/quartz-crystal-sio2`. Accessed: 08/11/2017.

[105] Bingham R. Grating spectrometers and spectrographs re-examined. *Quaterly Journal of the Royal Astronomical Society*, 20:395–421, 1979.

[106] Thorlabs. UV Fused Silica Broadband Plate Beamsplitters (Coating: 250 - 450 nm). `https://www.thorlabs.com/newgrouppage9.cfm?objectgroup_id=4806`. Accessed: 29/11/2017.

[107] Snik F. *Astronomical Polarimetry: new concepts, new instruments, new measurements and observations*. PhD thesis, Universiteit Leiden, 2009.

[108] Wikipedia. Orbital elements. https://en.wikipedia.org/wiki/Orbital_elements. Accessed: 18/07/2017.

[109] Longo C. and Rickman S. Method for the Calculation of Spacecraft Umbra and Penumbra Shadow Terminator Points. Technical report, NASA, 1995.

[110] Rickman S. Introduction to On-Orbit Thermal Environments. Documents available at https://nescacademy.nasa.gov/search?searchCriteria=thermal+environment&page=0. Accessed: 18/07/2017.

[111] Martinez I. Spacecraft Thermal Control Systems, Missions and Needs. Technical report, Universidad Politecnica de Madrid, 2016.

# Appendices

# Appendix A

# Polarimetry Basic Principles

## A.1 Stokes Parameters

The polarization state of an electromagnetic (EM) wave is characterized by the nature of the geometric figure that describes the end of the electric field vector in the wave plane [23][107].

Consider a monochromatic EM wave propagating along the $\vec{z}$ direction. Transverse components of the electric field associated to this wave are given by Equation A.1 where $\xi$ is the amplitude, $\omega$ is the angular frequency, $k$ is the wave number and $\delta$ is the phase between the two components. The polarization state of the EM wave depends on $\xi$ and $\delta$.

$$\begin{cases} E_x = \xi_x \ \cos(\omega t - kz) \\ E_y = \xi_y \ \cos(\omega t - kz + \delta) \end{cases} \tag{A.1}$$

Two particular cases can be pointed out from Equation A.1:

- $\delta = 0$: $E_x/E_y$ is constant and depends on the amplitudes $\xi_x$ and $\xi_y$. The wave is then said to be linearly polarized and the electric field describes a segment in the wave plane.
- $\xi_x = \xi_y = \xi_0$ and $\delta = \pm\frac{\pi}{2}$: the end of the electric field will describe a circle in the wave plane with a radius equal to $\xi_0$. Following the sign of $\delta$, the polarization is right circular or left circular.

The Stokes parameters are defined as follows [23][107]:

$$\begin{cases} I = \xi_x^2 + \xi_y^2 \\ Q = \xi_x^2 - \xi_y^2 \\ U = 2\xi_x\xi_y \cos\delta \\ V = 2\xi_x\xi_y \sin\delta \end{cases} \tag{A.2}$$

At this point, the definitions are established for a monochromatic EM wave. This notion of monochromaticity could be overcome defining the Stokes parameters from the elements of the coherency matrix. The transverse components of the electric field are now under the form of Equation A.3 [107].

$$\begin{cases} E_x(t) = \varepsilon_x e^{-i\omega t} = A_x e^{i(\phi_x - \omega t)} \\ E_y(t) = \varepsilon_y e^{-i\omega t} = A_x e^{i(\phi_y - \omega t)} \end{cases} \tag{A.3}$$

The coherency matrix of the field is written as in Equation A.4 where $\langle ... \rangle$ indicates a mean value over time and frequencies on a statistical set of non-correlated photons [107].

$$\mathcal{J} = \begin{pmatrix} \langle E_x E_x^* \rangle & \langle E_x E_y^* \rangle \\ \langle E_y E_x^* \rangle & \langle E_y E_y^* \rangle \end{pmatrix} \tag{A.4}$$

Therefore, the Stokes parameters are defined in Equation A.5 where $k$ is used to scale the Stokes parameters in $erg\ cm^{-2}\ s^{-1}\ sterad^{-1}\ Hz^{-1}$ [107].

$$\begin{cases} I = k(\langle \varepsilon_x^* \varepsilon_x \rangle + \langle \varepsilon_y^* \varepsilon_y \rangle) \\ Q = k(\langle \varepsilon_x^* \varepsilon_x \rangle - \langle \varepsilon_y^* \varepsilon_y \rangle) \\ U = k(\langle \varepsilon_x^* \varepsilon_y \rangle + \langle \varepsilon_y^* \varepsilon_x \rangle) \\ V = ik(\langle \varepsilon_y^* \varepsilon_x \rangle - \langle \varepsilon_x^* \varepsilon_y \rangle) \end{cases} \tag{A.5}$$

In conclusion, the four Stokes parameters allow to fully characterize the nature of a light beam. $Q$ and $U$ characterize the linear polarization states and $V$ is associated to the circular polarization state of the EM wave.

## A.2 Mueller Matrices

Mueller matrices describe the linear transformation between Stokes vectors (formed by grouping the four Stokes parameters into a single vector) before and after passing an optical surface. The general expression is given in Equation A.6.

$$\underbrace{\mathbf{S}_{instru}}_{measured} = \mathbf{M}\ \mathbf{S} = \underbrace{\begin{pmatrix} M_{11} & M_{12} & M_{13} & M_{14} \\ M_{21} & M_{22} & M_{23} & M_{24} \\ M_{31} & M_{32} & M_{33} & M_{34} \\ M_{41} & M_{42} & M_{43} & M_{44} \end{pmatrix}}_{known} \begin{pmatrix} I \\ Q \\ U \\ V \end{pmatrix} \tag{A.6}$$

When a beam of light passes through $N$ optical elements, each described by a specific Mueller matrix $\mathbf{M_j}$, the combined Mueller matrix $\mathbf{M'}$ of the whole assembly is given by Equation A.7.

$$\mathbf{M'} = \mathbf{M}_N \mathbf{M}_{N-1} \ ... \ \mathbf{M}_2 \mathbf{M}_1 = \prod_{j=1}^{N} \mathbf{M_j} \tag{A.7}$$

The Mueller matrices are very powerful tools for describing the polarization transfer function of an optical instrument. Their knowledge eventually allows to retrieve the intensity on the focal plane of the instrument as a function modulated by the incoming Stokes parameters that are generally the measurement goal.

## A.3 Jones Matrices

This formalism is based on $2 \times 2$ matrices with complex coefficients that are used to describe the changes of the transverse components of the EM field while passing through one or a set of optical parts. It is expressed in a general way in Equation A.8.

$$\begin{pmatrix} E_x^{(out)} \\ E_y^{(out)} \end{pmatrix} = \begin{pmatrix} a & b \\ c & d \end{pmatrix} \begin{pmatrix} E_x^{(in)} \\ E_y^{(in)} \end{pmatrix} \tag{A.8}$$

It is rather useful to use the Jones matrices for dealing with cases involving the superposition of wave amplitudes, for example. The Jones calculus is an adequate way to describe the coherent superposition of polarized light because it operates on amplitudes rather than on intensities.

Because of internal problems in the Advanced Systems Analysis Program (ASAP) optical engineering software, used to analyse the optical instrumentation in this thesis, it is not possible to use the Stokes parameters and the Mueller matrices. Only the Jones formalism is available for analysing the polarization state of the light passing through an optical device. However, Jones vectors and matrices can only describe 100% polarized light. This greatly restricts the cases of analyses that can be carried out.

# Appendix B

# Orbital Considerations

## B.1 Orbital Parameters

For defining the orbital parameters that fully characterize an orbit around the Earth, first a reference plane and a reference direction have to be defined. The reference plane is the Earth's equatorial plane. The intersection between the reference plane and the orbital plane is called the *line of nodes*. Eventually, the reference direction, which is contained inside the reference plane, is pointing to the *Vernal Point* $\gamma$[1]. Figure B.1 presents the reference plane and direction as well as the orbit and its associated elements [108].

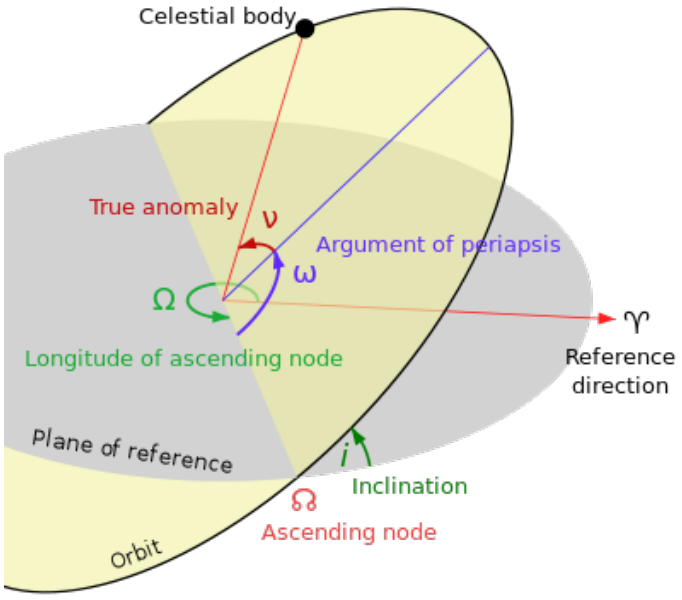


Figure B.1: Orbital elements representation [108].

[1]The Vernal Point indicates the apparent position of the Sun as seen from Earth at the vernal equinox occuring in March.

From these references and Figure B.1, the six Keplerian elements are defined as followed [108]:

- **Eccentricity** $e$: it defines the shape of the ellipse, i.e. how elongated it is compared to a circle;
- **Semi-major axis** $a$: it is the sum of the periapsis and apoapsis distances divided by two;
- **Inclination** $i$: it is the vertical tilt of the ellipse with respect to the reference plane, measured at the ascending node (where the orbit passes upward through the reference plane). This angle is measured perpendicular to the line of nodes;
- **Right Ascension of the Ascending Node** (RAAN) $\Omega$: it indicates the angle between the ascending node and the reference direction as measured horizontally in the reference plane;
- **Argument of periapsis** $\omega$: it defines the orientation of the ellipse in the orbital plane, as an angle measured from the ascending node to the periapsis;
- **Mean anomaly at epoch** $M_0$[2] it defines the position of the satellite along the ellipse at a specific time (epoch).

## B.2 $\beta$ Angle and Eclipse Duration

One of the most important parameters for characterizing the orbit of a satellite with respect to the Sun is the $\beta$ angle. This angle is defined as the angle between the solar vector **s** and its projection onto the orbit plane of the satellite [109] (see Figure B.2).

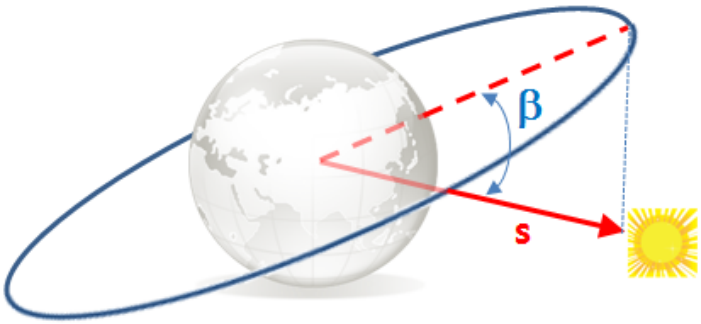


Figure B.2: $\beta$ angle definition. Figure from [110].

[2] $M_0$ is a mathematically convenient angle which varies linearly with time but which does not correspond to a real geometric angle. It can be converted into the **true anomaly** $\nu$ which does represent the real geometric angle in the plane of the orbit, between the periapsis and the position of the satellite at any given time via the resolution of the non-linear equation of Kepler [108]

This angle can be calculated from the geometrical definition of the solar vector and the orbit. First, consider an Earth-Centered Inertial (ECI) coordinate system as for the definition of the orbital elements in the previous section. The coordinate system is centered on the Earth center, the $x$-axis is pointing towards the Vernal Point and the $z$-axis is pointing in the direction of the North Pole (i.e. perpendicular to the Celestial Equator). In this reference frame, the Sun is moving around the Earth and its motion is constrained to the Ecliptic Plane oriented at an angle $\varepsilon$ with respect to the Celestial Equator (Figure B.3). In the Ecliptic Plane, the Ecliptic True Solar Longitude $\Gamma$ refers to the instantaneous position of the Sun and is equal to zero at the Vernal Equinox. The solar vector $\mathbf{s}$ can be evaluated via two transformations: a first rotation of the unit vector around the $x$-axis by an angle $\varepsilon$ and then a rotation of an angle $\Gamma$ around the new $z$-axis [109][110]. It is mathematically expressed by Equation B.1.

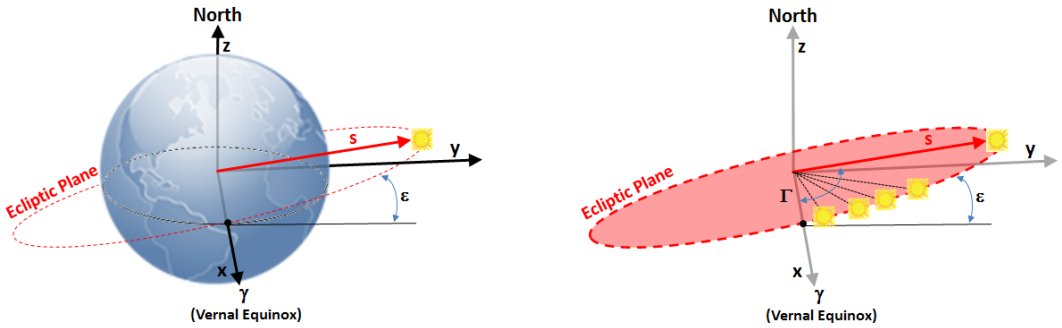


Figure B.3: Solar vector representation in ECI coordinate system. Figures from [110].

$$\mathbf{s} = \begin{pmatrix} 1 & 0 & 0 \\ 0 & \cos\varepsilon & -\sin\varepsilon \\ 0 & \sin\varepsilon & \cos\varepsilon \end{pmatrix} \begin{pmatrix} \cos\Gamma & -\sin\Gamma & 0 \\ \sin\Gamma & \cos\Gamma & 0 \\ 0 & 0 & 1 \end{pmatrix} \begin{pmatrix} 1 \\ 0 \\ 0 \end{pmatrix} = \begin{pmatrix} \cos\Gamma \\ \sin\Gamma\cos\varepsilon \\ \sin\Gamma\sin\varepsilon \end{pmatrix} \quad \text{(B.1)}$$

Now that $\mathbf{s}$ is defined, the unit vector $\mathbf{o}$, which is normal to the orbital plane, will characterize the orbit for the $\beta$ angle definition (Figure B.4). $\mathbf{o}$ can be expressed, as for the solar vector, as a combination of two transformations: first a rotation of $\Omega$ (RAAN) of the unit vector around the $z$-axis and then a rotation of $i$ (inclination) around the new $x$-axis. It is mathematically expressed by Equation B.2.

$$\mathbf{o} = \begin{pmatrix} \cos\Omega & -\sin\Omega & 0 \\ \sin\Omega & \cos\Omega & 0 \\ 0 & 0 & 1 \end{pmatrix} \begin{pmatrix} 1 & 0 & 0 \\ 0 & \cos i & -\sin i \\ 0 & \sin i & \cos i \end{pmatrix} \begin{pmatrix} 0 \\ 0 \\ 1 \end{pmatrix} = \begin{pmatrix} \sin\Omega\sin i \\ -\cos\Omega\sin i \\ \cos i \end{pmatrix} \quad \text{(B.2)}$$

Eventually, the angle between the solar vector and the vector normal to the orbital plane is $\phi$ such as $\cos\phi = \mathbf{o}.\mathbf{s}$. Knowing that, the $\beta$ angle is simply equal to $90° - \phi$, its final expression is given by Equation B.3.

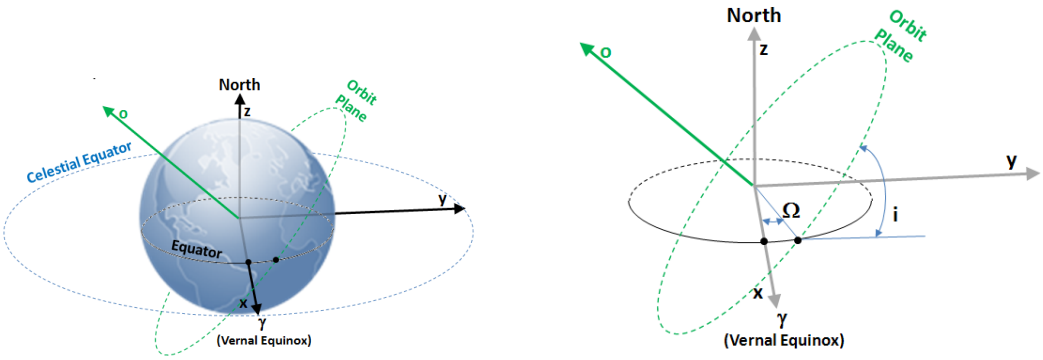


Figure B.4: Definition of the orbital plane normal vector **o**. Figures from [110].

$$\beta = \arcsin(\cos\Gamma \sin\Omega \sin i - \sin\Gamma \cos\varepsilon \cos\Omega \sin i + \sin\Gamma \sin\varepsilon \cos i) \tag{B.3}$$

Equation B.3 allows to evaluate $\beta$ of any given orbit as a function of time as the parameters on which it depends vary with time. It is then possible to evaluate the fraction of eclipse $f_{eclipse}$ of a period for a given orbit as a function of $\beta$ as expressed by Equation B.4 [111].

$$f_{eclipse} = \frac{1}{180^\circ} * \arccos\left(\frac{\sqrt{2 * R * H + H^2}}{(R + H) * \cos\beta}\right) \tag{B.4}$$

In equation B.4, $R$ is the Earth radius and $H$ is the orbit altitude (assuming a circular orbit). Figure B.5 shows the percent of orbital period in eclipse as a function of $\beta$ and for several altitudes $H$. From this result, it is clear that if the goal is to minimize the eclipse duration for any orbit, $\beta$ should be maximized.

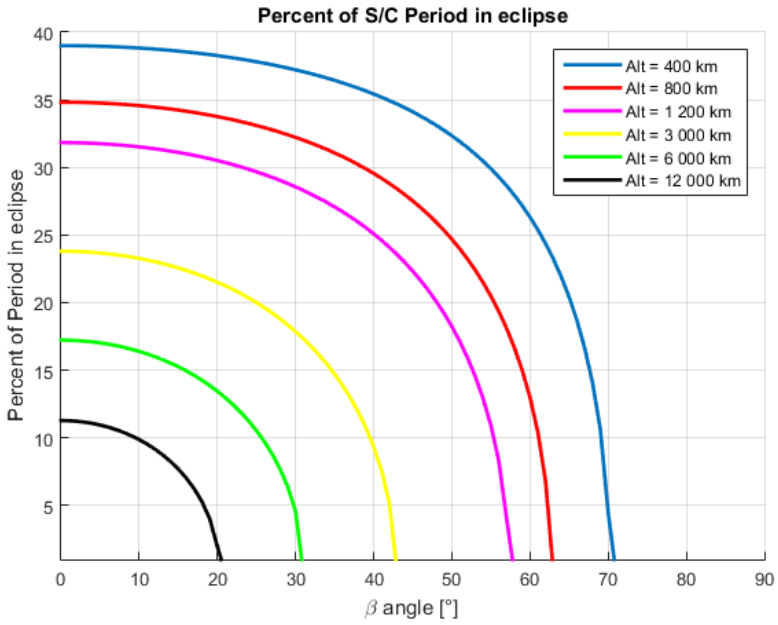


Figure B.5: Percent of orbital period in eclipse as a function of $\beta$ and altitude $H$.

## B.3 Sun-Synchronous Orbit

A Sun-Synchronous Orbit (SSO) is a geocentric orbit that combines inclination and altitude such that the rate of precession of the ascending node due to the $J_2$ term of the geopotential[3] closely matches the mean motion of the Sun as it moves about the celestial sphere. A SSO then should have a relatively flat profile of $\beta$ angle versus time. In other words, it is possible to achieve a nearly constant solar irradiation condition, with the benefit to drastically simplify the thermal environment of the satellite and thus the thermal design. The condition can be expressed mathematically by using the variation of the orbit's RAAN during one orbit (Equation B.5 [82]).

$$\Delta\Omega = -2\pi * \frac{J_2}{\mu p^2} * \frac{3}{2} * \cos i \tag{B.5}$$

In Equation B.5, the parameters are:

- $J_2$ is the coefficient for the second zonal term related to the oblateness of the Earth in the *Geopotential model*;
- $\mu$ is the *Standard gravitational parameter* of the Earth;
- $p$ is the semi-latus rectum of the orbit, defined as $p = a\ (1 - e^2)$;

[3]The $J_2 = 0.00108$ term measures the most important deviation of the Earth's potential from that of a sphere. It essentially reflects the equatorial flattening of the Earth and leads to a $1/r^3$ term in the expression of the potential.

- $i$ is the inclination of the orbit.

In order to have a SSO, we define the nodal precession rate $\rho$ which should be equal to the mean motion of the Earth about the Sun which is 360° per sideral year. The nodal precession rate is defined as $\rho = \frac{\Delta\Omega}{P}$ where $P$ is the orbital period. Considering a circular orbit, the period is $P = 2\pi\sqrt{\frac{a^3}{\mu}}$ ($a$ is the semi-major axis of the orbit) and $a = p$. Eventually from these expressions, the inclination of the orbit could be extracted in Equation B.6.

$$\rho = \frac{\Delta\Omega}{P} = \frac{-2\pi * \frac{J_2}{\mu a^2} * \frac{3}{2} * \cos i}{2\pi * \sqrt{\frac{a^3}{\mu}}} = -\frac{J_2}{\sqrt{\mu a^7}} * \frac{3}{2} * \cos i$$

$$\leftrightarrow \cos i = -\frac{2}{3} * \rho * \frac{\sqrt{\mu}}{J_2} * a^{7/2} \tag{B.6}$$

# Appendix C

# Published Article

The article *A 3U CubeSat to Collect UV Photometry of Bright Massive Stars* has been published in the *Journal of Small Satellites*, Volume 6, Number 3. The full published version is presented in the following pages.

www.DeepakPublishing.com

Desselle, R. et al. (2017): JoSS, Vol. 6, No. 3, pp. 635–650
*(Peer-reviewed article available at www.jossonline.com)*

www. JoSSonline.com

# A 3U CubeSat to Collect UV Photometry of Bright Massive Stars

Richard Desselle, Christian Kintziger, and Pierre Rochus

*Centre Spatial de Liège, University of Liège*
*Liège, Belgium*

Gregor Rauw and Yaël Nazé

*Groupe d'Astrophysique des Hautes Energies*
*University of Liège*
*Liège, Belgium*

**Abstract**

The last decade has witnessed exciting progress with the miniaturization of essential components of spacecraft, leading to the development of nano-and micro-satellites beyond their use as mere technological experiments. These small satellites are now considered to be important complements of much larger and more sophisticated probes to conduct scientific research. In this context, the current authors have conducted a feasibility study of a near-ultraviolet (UV) telescope onboard a three-unit (3U) CubeSat. The scientific purpose of this payload will be to collect time series of photometric measurements of bright, mainly massive, stars down to an optical magnitude of V=5. This paper presents the optimized optical design of the payload and its associated detector. It further discusses the system accommodation and integration, as well as a providing a preliminary mission analysis. A photometric budget taking into account the characteristics of the target stars and the payload performances is also presented. This feasibility study demonstrates that it is possible to conduct a robust science mission using a very small satellite at limited cost.

## 1. Introduction

### 1.1. Astrophysical Background

Since the termination of the International Ultraviolet Explorer (IUE) mission in 1996 and the end of the Far Ultraviolet Spectroscopic Explorer (FUSE) in 2007, the ultraviolet (UV) domain suffers from a lack of dedicated instrumentation. Indeed, the situation is very different from other wavelength domains. The optical and near-IR (infrared) wavelength ranges can be observed from the ground at many observatories. Moreover, several far-IR space observatories are under construction or in planning. However, there is currently no mid-to far-UV mission at a similar level of preparation, though the UV domain has great diagnostic potential, especially for the study of bright massive stars whose spectral energy distribution peaks in the UV. Spectroscopy clearly offers the highest scientific return, as many chemical elements have strong resonance lines in this wavelength domain. The analysis of such lines provides sensitive diagnostics of the stellar and wind parameters. However, high-resolution

Corresponding Author: Richard Desselle, rdesselle@ulg.ac.be

spectroscopic astronomical missions require large aperture telescopes. This can only be accommodated on medium or large space missions (e.g. Gómez de Castro et al., 2014). On the other hand, as demonstrated by the Optical Monitor (OM) instrument on-board XMM-Newton (Mason et al., 2001), sensitive UV photometry can be performed with much smaller telescopes. In particular, monitoring the photometric variations of stars has an important scientific return. Such data are of paramount importance for asteroseismology, where measuring the radial and non-radial pulsations of stars allows probing the physical conditions in their interiors (e.g. Handler, 2013). In asteroseismology, an important problem, especially for massive stars, is the identification of pulsation modes. Such an exercise requires multicolor photometric time series. The UV data are especially important here to complement optical data because the relative amplitudes of the photometric changes are larger at shorter wavelengths (Aerts et al., 2010). Space-borne platforms constitute an essential tool in this context, as they overcome the limitations due to variable atmospheric absorption as well as the long daily gaps measurements. However, the power of such data is not restricted to asteroseismology. Illustrations are the intriguing CoRoT light curves of early-type stars in NGC 2244 (Blomme et al., 2012, and references therein), or the detection of flaring activity and rotational modulation in magnetically active late-type stars with Kepler (Davenport, 2016). In addition, accurate space-borne UV photometry also allows studying the development of disks around Be stars, as well as many phenomena linked to binary interactions (i.e., tidal deformations, eclipses, etc.).

### 1.2. Proposed Instrument and Mission

Ambitious, sophisticated space observatories are complex and expensive (typically around 1 billion euros), usually restricting their construction and operation to major space agencies. FUSE, for example, was a NASA mission whose development was led by the Johns Hopkins University. Collaborators originated from other universities (Boulder and Berkeley) and international partners, such as the Canadian and the French Space Agencies (Conard et al., 2000). In the same vein, the IUE mission was an international collaboration between NASA, the European Space Agency and the United Kingdom's Science and Engineering Research Council (Bogges et al., 1978).

The situation is different for CubeSats, which are built from one or several $10 \times 10 \times 10$ cm$^3$ units. Over recent years, it has been demonstrated that such CubeSats can be developed by small teams and successfully used for scientific research for a typical cost of a few million euros (Woellert et al., 2011). In the same field of application as the current project, the BRITE constellation (Weiss et al., 2014) and the ExoplanetSat (now called ASTERIA) project (Smith et al., 2010) provide good illustrations of CubeSats being used or developed for the study of stars and their environment. CubeSats cannot compete with large, expensive space observatories, but they can complement them, and fill some niches that are not covered by the larger facilities.

In this context, the current paper presents a feasibility study of a new space-borne near-UV telescope that could be installed onboard a three-unit (3U) CubeSat. The aim of the telescope is to acquire photometric time series of bright, mainly massive, stars between 2500 and 3500 Å. Such a mission has never been performed before. Indeed, most scientific CubeSats are designed for Earth and atmosphere observations, cosmic rays detection, or stellar observations in the visible domain (Swartwout, 2013). Observing in the UV prevents the use of a refractive telescope composed of lenses such as used for BRITE. These configurations are generally more compact, and thus more suitable for such small platforms. This study's goal is to reach the scientific requirements summarized in Table 1. These

Table 1. Scientific Requirements for the Proposed Near-UV Telescope

| Parameter | Requirement | Goal |
|---|---|---|
| Spectral range | 2500–3500 Å | N/A |
| Angular resolution | 15 arcsec | 10 arcsec |
| Field of view (diameter) | 1° | 2° |
| Target magnitudes | $V \leq 4$ | $V \leq 5$ |
| Photometric accuracy | 0.001 mag | 0.0005 mag |
| Typical exposure time | 5 min | 1 min |
| Mission duration | 2 years | 4 years |
| Duty cycle | 60% | 75% |

requirements are inspired by the OM instrument onboard XMM-Newton (Mason et al., 2001), but scaled for a smaller telescope size. They also take into account security margins which anticipate the limitations of very small platforms. The current study aims to use the smallest possible spacecraft platform, which is the 3U CubeSat. Indeed, a smaller platform would not allow designing a telescope sufficiently sensitive to meet the specifications while carrying the elements necessary for the operation of the satellite. In view of numerous successful 3U CubeSat scientific missions, such as CINEMA or EXOCUBE (NSF-NASA, 2013), one can be confident that a 1.5U volume is sufficient to accommodate the service module. Nevertheless, achieving the photometric accuracy with a small telescope is a great challenge. Section 2 discusses the optical design, Sections 3 and 4 present the components and orbit to be used, and Section 5 examines the photometric budget. Concluding remarks are found in Section 6.

## 2. Optical Design

### 2.1. Basic Considerations and Constraints

Since the transmission of lenses is very poor in the UV, reflecting optics must be used. The baseline design in the current study is thus a Ritchey-Chrétien telescope composed of two reflective hyperbolic mirrors. This kind of telescope has advantages such as a high optical performance with only two reflective surfaces, as well as a large aperture. Preliminary research on off-the-shelf components for CubeSat revealed that at least 1.5U is needed for vital sub-units such as electronics, communication, attitude controller, etc. The payload is thus constrained to fit into the remaining 1.5 CubeSat units, with the optical axis oriented along the CubeSat length to benefit from the largest focal length possible. The mirrors are coated with a specific UV aluminum coating (Melles Griot, 2016), offering an average reflectance of 87% over the spectral domain of the instrument. To reject unwanted light that could reach the telescope's focal plane, two devices will be implemented. First, a UV filter (Schott, 2016) will be placed directly in front of the focal plane to reject the light of wavelengths outside the [2500, 3500] Å range (surface #4 in Figure 1). In addition, a baffling system will be installed on the two mirrors to reject the light from outside of the scientific field of view (FoV).

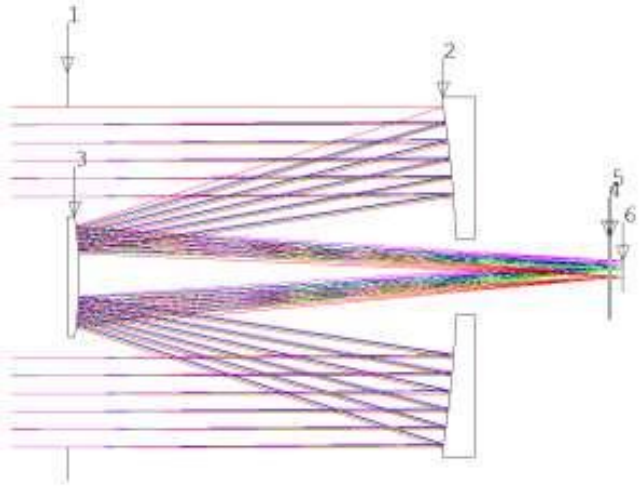


Figure 1. A 2D view of the near-UV telescope optical design and the representation of several off-axis rays passing through the entrance pupil and reaching the focal plane. Surfaces: #1 = entrance pupil of the telescope, #2 = primary mirror, #3 = secondary mirror, #4 = front face of the UV-filter, #5 = back side of the UV-filter and #6 = focal plane.

### 2.2. Design Characteristics

#### 2.2.1. Optimization Workflow

The optimization process consists in obtaining an optical design that fulfills both the scientific requirements and the inherent constraints of a CubeSat payload. A first constraint is the diameter of the entrance aperture of the telescope (surface #1 in Figure 1). This latter is set to 90 mm to maximize the amount of light collected by the telescope while simultaneously respecting the volume constraints given by an off-the-shelf 3U CubeSat structure (ISIS Space, 2017). Then, the allocated room for the optical design is fixed to 1.5U for the reasons previously explained.

Typical near-UV optimized detectors exhibit pixel sizes of 13 or 26 µm (e.g. Teledyne e2v, 2017). It was decided to use 13 µm pixels as a baseline, to reduce the dimensions of the entire focal plane. The smaller pixel dimension also enables the use of shorter focal lengths for a given angular resolution and eases the coupling of the optical design to its CubeSat architecture.

Anticipating saturation issues (addressed in Section 5.3), the study fixed the number of pixels illuminated by the PSF at four. Therefore, the light of an observed star will spread onto a square of 26 µm side to relax the photometric budget of the instrument. Knowing the pixel size and the required angular resolution of 15 arcsec (Table 1), the minimum required effective focal length $f_{eff}$ is evaluated to 357.5 mm.

The above constraints and requirements were then set in Code V to obtain an optimized telescope that fits within 1.5 units of a CubeSat. Another critical parameter is the obstruction by the secondary mirror (surface #3 in Figure 1). The goal during the design process was thus to minimize the size of this element to maximize the incoming photon flux. For that purpose, several mechanical layouts of the telescope within the range of the strict CubeSat volume constraints were studies, and the one that fit the above considerations was selected.

The final value of $f_{eff}$ after optimization amounts to 487.5 mm, yielding an angular resolution of 11 arcsec. The study was therefore able to take advantage of the available platform room and surpass the requirement in Table 1. It also achieved a reduction in light transmission due to the obstruction of only 13% (without the baffling system presented in Section 2.2.3), which is completely acceptable for the current application, as will be demonstrated with the photometric budget described in Section 5. The 2D layout of the telescope and the associated characteristics are presented in Figure 1 and Table 2, respectively.

Table 2. Geometrical Characteristics of the Near-UV Telescope Presented in Figure 1

| Parameter | Requirement |
|---|---|
| Entrance aperture diameter (surface #1) | 90 mm |
| Primary mirror diameter (surface #2) | 92 mm |
| Secondary mirror diameter (surface #3) | 32 mm |
| Effective focal plane diameter (surface #6) | 12 mm |
| Distance between surface #1 and surface #2 | 100 mm |
| Distance between surface #1 and surface #4 | 143 mm |
| Distance between surface #1 and surface #6 | 147 mm |

Attempts to increase the size of the FoV beyond the required diameter of 1° revealed a very fast degradation of the PSF for large off-axis angles. This degradation of the PSF was due to astigmatism, the main aberration suffered by the Ritchey-Chrétien telescopes (Figure 2). Optimizing the telescope efficiency up to

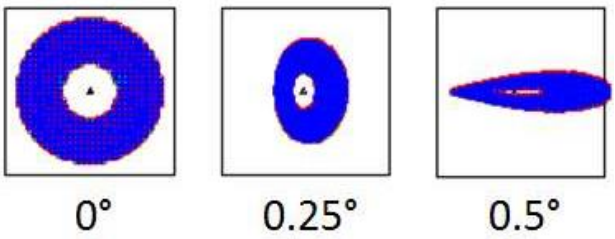


Figure 2. Spot diagrams of the designed photometer for squared areas of 26 µm side considering 3 off-axis angles (0, 0.25 and 0.5° from left to right).

2° led to the use of complex optical surfaces and large central obstructions. It was decided to favor simplicity and the light transmission of the selected design for our CubeSat baseline. On the other hand, photometric measurements may still be carried out slightly beyond 1° with the somewhat degraded angular resolution.

### 2.2.2. Spot diagrams

The spot diagrams for several off-axis positions are shown in Figure 2 where the squares are 26 × 26 µm since the system is optimized to fit the spot onto four pixels of 13 µm size. As can be seen for small off-axis angles (0° and 0.25°), the light is uniformly (or quasi-uniformly) spread over the bundle of pixels illuminated at the focal plane. For larger angles (near 0.5°), the spot is elongated along the radial direction. The flattening of the spot is typical of astigmatism optical aberration. This degradation of the PSF uniformity has implications on the data reduction, although observations of fields with several bright stars ($V \leq 5$) falling into the FoV of the instrument will be the exception rather than the rule. Thus, the degradation of the spot uniformity for large off-axis angles is not considered to be an issue. It was also noted that the central holes that appear in all the spots are simply due to the central obscuration at the entrance pupil of the telescope.

### 2.2.3. Baffling System and Stray Light Analysis

As all telescopes do, Ritchey-Chrétien telescopes suffer from stray light when not protected by an optical

baffle. A baffling system was designed in this study, based on procedures described by Terebizh (2001) to prevent stray light from directions outside the FoV from reaching the focal plane. This enables a geometrical optimization of the baffles to block unwanted light from the sky while simultaneously minimizing the obscuration of the system by the baffle placed on the secondary mirror M2. This concept is based on two conic baffles located in front of the two mirrors. A main baffle surrounding the overall instrument and some vanes on each baffle were also added, to block internally-reflected, second-order stray light. The final configuration of the baffling system installed on the telescope is presented in Figure 3. Considering this final layout, the study was able to reassess the value of the effective diameter of the telescope. The secondary mirror and its baffle produce an obscuration equivalent to a diameter of 38 mm that must be compared to the 90 mm diameter of the entrance pupil, leading to a telescope effective diameter equal to 81.5 mm, and corresponding to a reduction in light transmission of 17% compared to the 13% without the baffling system. The new effective diameter will be used in our photometric budget computation in Section 5.

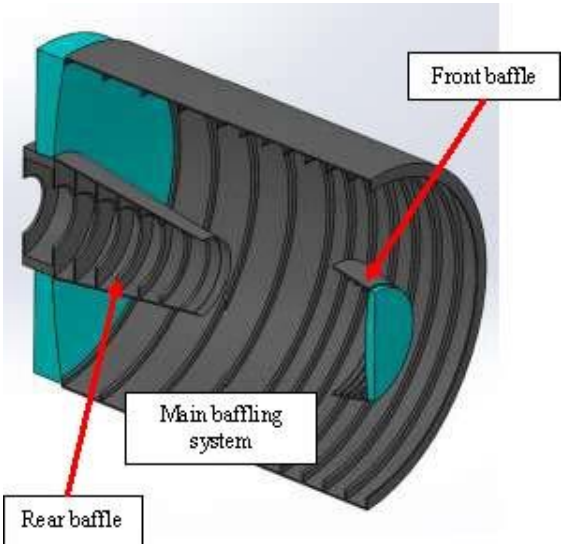


Figure 3. Cross-sectional view of the baffling system integrated around the optical design.

Using the ASAP software, this study quantified the relative amount of photons coming from off-axis angles of an entire sky hemisphere, entering the telescope, and reaching the focal plane. This quantity was determined by defining a light source covering a part or the entire focal plane, and then assuming that this source emits light in one hemisphere in the direction of the secondary mirror. The light is then back-propagated through the telescope until it reaches the entrance pupil. Those photons are then sorted according to their incidence angle on the pupil to identify the off-axis fields reaching the detector since their propagation path is reversible. This method is commonly used, since any simulation using the direct path cannot simulate an infinite set of FoVs. For modeling, the inner walls of the baffles are coated with Chemglaze (black coating with very low reflectance) (Persky, 1999), but they still induce some scattered reflections. The study also used the Harvey model (Harvey, 1975) for characterizing the reflections on the mirrors, more specifically their scattering behavior with respect to roughness.

Figure 4 presents the relative quantity of photons that pass through the telescope and reach the central position on the focal plane as a function of their off-axis angles (measured from the center of the FoV (0°,0°)). From this figure, it can be seen that the maximum is naturally reached on-axis at (0°,0°). However, scattered light enables some other fields of view to reach these pixels too. Nevertheless, the levels of those directions are below 0.0001% of the on-axis maximum level. When the entire noise over the hemisphere is integrated, assuming a uniform emission, it was found that for one effective photon from (0°,0°), 0.007 photon is also obtained from the rest of the field.

To assess the effective level of stray light, the brightness of a sky hemisphere must be evaluated as it will be seen from space. According to Roach (1964), there are two main contributions: stellar and zodiacal light. Using the results of Leinert et al. (1998) and Gonhalekar et al. (1980), it was estimated that the combined amount of light from these contributions at the entrance of our instrument is $N_{SL} = 8.73 * 10^7$ photons/cm².s over the 2500–3500 Å range for an entire hemisphere. This value will be associated to a noise parameter in the photometric budget.

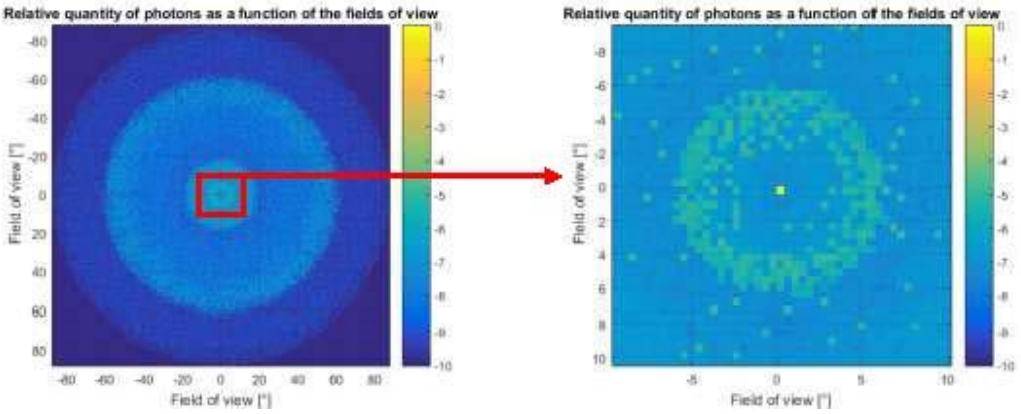


Figure 4. Relative quantity of photons, passing through the instrument and reaching the central position of the focal plane, as a function of the fields of view/off-axis angles over an entire hemisphere of the sky. The quantity of photons is given in a logarithmic scale.

## 3. System Overview

### 3.1. Solar Panels Configuration

Figure 5 shows the design of the 3U CubeSat with its solar panels in a table configuration. It can be seen that the payload fits into 1.5U as it was chosen. The other half of the S/C is dedicated to the sub-units needed to obtain a fully operational satellite. The volumes of these units (top and bottom parts of Figure 5) are simulated using computer-aided designs (CAD) of

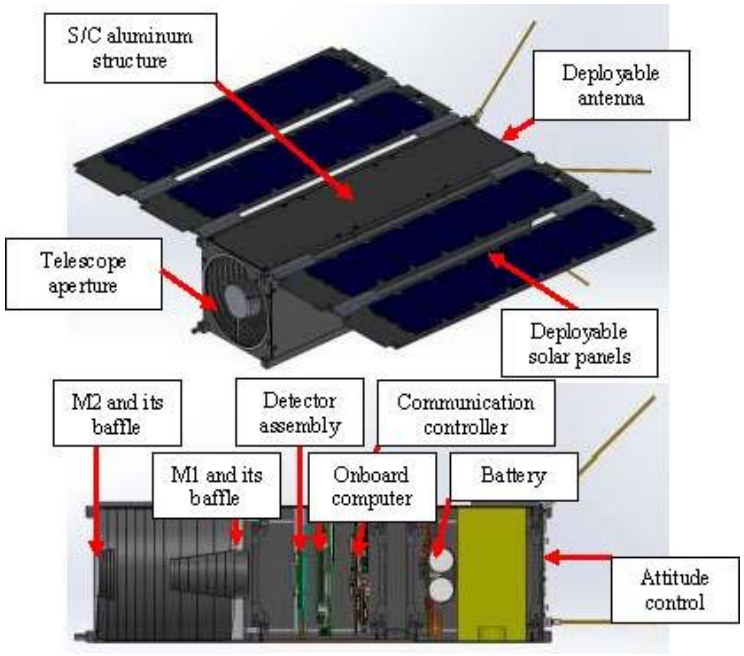


Figure 5. Overview and cross-sectional side-view of the table configuration of the 3U CubeSat. Bottom figure from left to right: the secondary mirror and its baffle which are mounted on a support linked to the S/C structure by three thin feet; the primary mirror and its baffle which are mounted on a support directly fixed to the spacecraft structure; the detector assembly composed of the detector, an electronic card, a thermal insulation made of Permaglas, an aluminum structure and a radiator; the onboard computer (CAD from ISIS Space, 2017); the communication controller (CAD from GOMSpace, 2017); the battery (CAD from GOMSpace, 2017); the attitude determination and control system (ADCS) (volume from Blue Canyon Technologies, 2017); and the deployable antenna (CAD from GOMSpace, 2017).

some components off-the-shelf (COTS) from several manufacturers. The sub-units will be briefly discussed in Section 4.3. Four deployable solar panels are represented.

During the design process, the table configuration was compared to a cross one where the solar panels are attached to the opposite side of the telescope aperture. The comparison was made with respect to the constraints on the sky visibility of the two configurations, assuming the satellites in the same orbit presented in Section 4.1. The cross configuration solution suffered from a lack of pointing flexibility because it is highly constrained by its Sun aspect angle for the power generation and also avoidance zones where the Earth or the Moon could be in the field of view. The table configuration is able to point in almost any direction in the sky for scientific observation during the mission while the sky visibility of the cross configuration is restricted to a narrow band of the sky around the ecliptic, explaining our preference for the table configuration.

### 3.2. Detector Characteristics

To reach a high efficiency in the near-UV, it is best to use a back-illuminated, thinned CCD detector. As an example, an off-the-shelf detector from e2v (e2v Technologies, 2017) that is suitable for the current application was identified. The main characteristics of the detector are shown in Table 3. The UV-coated

Table 3. Characteristics of the CCD47-20 from e2v (e2v Technologies, 2017)

| Parameters | Value |
|---|---|
| Pixel size | 13X13 μm |
| Number of pixels | 1024X1024 |
| Full well capacity (peak) | 100 k$e^-$/pixel |
| Dark signal at 0°C (at −40°C) | 25 $e^-$/pixel s (0.05 $e^-$/pixel s) |
| Charge transfer efficiency | 99.9 % |
| Readout noise at 20 kHz | 2 rms $e^-$/pixel |
| Maximum readout frequency | 5 MHz |

CCD has a non-constant quantum efficiency ranging between 55% and 75% in the spectral domain under consideration.

### 3.3. Data storage and transfer

Current printed circuit boards proposed for CubeSat applications are designed with several ports for memory cards up to 8 GB. It is reasonable to assume that onboard data storage capacity will be at least 16 GB. A scientific image size can be quantified using the number of pixels (Table 3). Assuming that each pixel contains 32 bits of information, the size of each image is evaluated at 4.19 MB. If memory cards are only used for storing scientific data, they are able to receive more than 3800 images before saturating.

Table 1 indicates a duty cycle goal of 75%. In other words, it assumes that 75% of the mission is dedicated to scientific observation. Anticipating the orbit definition (Section 4.1), the duty cycle could be translated into approximately 75 min per orbit, considering the period of Table 4. If the observation time goal of 1 min

Table 4. Orbital Parameters of a Dusk-dawn SSO for a Launch on January 1, 2020, at midnight. The Parameters have been Defined Using the J2 Propagator of the Satellite Tool Kit (STK) Software

| Parameters | Value |
|---|---|
| $a$, semi-major axis | 7178.14 km |
| $e$, eccentricity | 5.70681e-16 |
| $i$, inclination | 98.5880° |
| $\Omega$, RAAN | 190.128° |
| $\omega$, argument of periapsis | 0° |
| $\nu_0$, true anomaly at launch 0.1089° | 0.1089° |
| T, period | 100.8735 min |

(Table 1) is reached, 75 images will be acquired per orbit, which corresponds to 314.25 MB stored in memory cards. It will then take a little bit more than 50 revolutions to fill up the entire memory.

Off-the-shelf antenna and communication controllers are numerous for CubeSats. From research on manufacturers' websites, a data transfer rate up to 100 kbps is considered for a preliminary data transfer evaluation. In terms of image transfer, it would take 5 minutes and 35 seconds to download a full image from the spacecraft to the ground station – i.e., more than five times longer than the time of data acquisition.

Hence, it is not possible to download full images while respecting the duty cycle requirement. Restricting the data to a window of 100 × 100 pixels will reduce the image size by a factor of approximately 100, which will be easier to handle with a COTS antenna. Such a window of 100 × 100 pixels is sufficient to collect the signal of a target star and also the background for data reduction. Since the mission is designed to observe bright stars, which are relatively isolated, such a windowing will not reduce the scientific return. However, if several targets were to be observed simultaneously, the windowing algorithm associated to the CCD electronics would need to be adapted to enlarge the window or to select several windows corresponding to each star of interest. It could be anticipated by establishing a very precise and complete observation plan for the entire mission.

## 4. Thermal Environment and Analysis

### 4.1. Orbit Definition

The strategy for orbit definition was to maximize the duration of sunlight exposition to benefit from a maximal power supply. It was also a goal to minimize the Sun exposure variation over the lifetime of the mission. Considering these constraints, a dusk-dawn Sun-synchronous orbit (SSO) was chosen that provides a relatively constant and maximal solar exposure during the mission. It was also assumed that the orbit would be a low Earth orbit with an altitude not higher than 800 km. A hypothetical launch date of January 1, 2020, at midnight, was used. The associated orbital parameters are presented in Table 4.

The propagation of the orbit of Table 4 with the STK software allows analyzing, for a two-year mission, the percentage of eclipse over a full orbit as a function of time (Figure 6). From Figure 6, it is known that 148 days of the entire mission (±20%) are subject to an eclipse with a maximum duration reaching 17% of the orbit (i.e., 17 min per orbit). Since there are eclipses, even though not all the time, an on-board battery is required. The knowledge of the illumination also provides direct constraints for the thermal design of the spacecraft (see further details in the next Section).

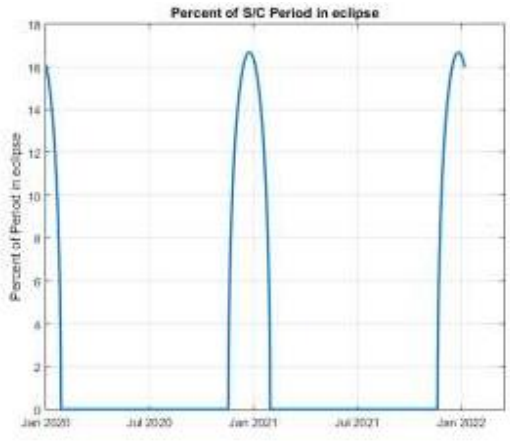


Figure 6. Percentage of a full orbit spent in eclipse as a function of time and for a two-year mission starting January 1, 2020.

### 4.2. Thermal Considerations

A preliminary thermal analysis was conducted to quantify the temperatures of the elements onboard the CubeSat, especially to check whether the temperature of the detector and the solar panels fall in their operational windows. Figure 6 shows that the CubeSat will spend very long periods exposed to the Sun. Therefore, a worst case hot stationary scenario was analyzed, where the solar panels are exposed to sunlight and where other sides of the CubeSat are exposed to the Earth's thermal radiation and albedo. It was also assumed that the payload was working, because this makes the detector electronics dissipate some heat and warms it up.

Since the detector is a CCD, its dark noise increases as it gets hotter and therefore, the colder it is, the better. Heat from the detector will be evacuated via a dedicated radiator made of copper that is mechanically connected to the detector assembly (Figure 7). This radiator is thermally decoupled from the rest of the CubeSat and faces deep space to radiate heat to its environment. The mechanical connection between the radiator and the detector, as well as the radiator surface itself, have been optimized to achieve a sufficiently low temperature of the detector allowing observing stars, even in the worst case.

The geometrical and thermal mathematical models (GMM and TMM) of the CubeSat, the payload, and the sub-units are built in ESATAN software. The main

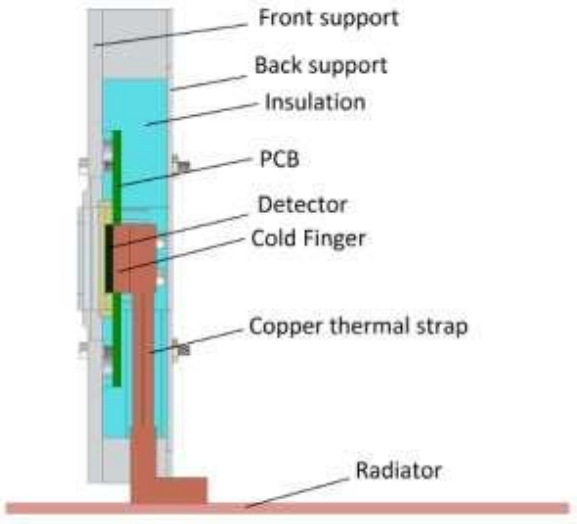


Figure 7. Cross-sectional side-view of the detector assembly and its radiator. The radiator is connected to the back of the detector thanks to a copper cold finger and a copper thermal strap. The blue part surrounding the detector and the copper parts is composed of Permaglas, to minimize the conductive heat transfers between the detector and its mechanical support connected to the satellite structure.

purposes of the GMM are the computation of the radiative exchange factors of each surface and the definition of interfaces and their associated conductance. The TMM defines the thermal and thermo-optical properties of the materials and surfaces. Special attention has been paid to external surfaces that receive heat from the main sources (Sun and Earth) and radiate heat to the cold space. Their surfaces are covered by white paint, to reduce absorbed flux from external sources and increase the power radiated to cold space.

The worst case hot thermal analysis provides the following results for the temperatures of the solar panels (SP) and of the detector, respectively: $T_{SP} \approx 60°C$ and $T_{CCD} \approx 0°C$ 0°C. According to Clyde Space (2017), the solar panels are working up to temperatures of 125°C. The current analysis thus confirms that the panels' temperature is in their operational range. Concerning the detector, $T_{CCD}$ is close to 0°C, where the detector has a level of dark noise approximately equal to 25 $e^-$/pixel s (e2v Technologies, 2017) – i.e., 500 times higher than the level at −40°C (Table 3). This value of dark signal is quite high, compared to more classical configurations where the sensor is cooled down, but the signal-to-noise ratio calculation in Section 5 demonstrates that it remains acceptable for the current application.

### 4.3. Power Budget

Several COTS have been considered to quantify the current general characteristics of main CubeSat units, and are described here to reference their power consumption:

- For the onboard computer (OBC), it is proposed to use an ISIS On Board Computer (ISIS Space, 2017). This space-qualified processing unit has a flight heritage since 2014. Its power consumption amount to 400mW on average, with a peak at 550mW.
- The communication system proposed is composed of the NanoMind A3200 and the NanoCom AX100 (GOMSpace, 2017). The first is an additional OBC that could add some data storage volume and redundancy for the subunits in charge of the control software and the second is a software configurable narrow-band transceiver for ultra-high frequency (UHF) and very high frequency (VHF) transmission that is able to reach the data rate transfer presented in section 3.3. The total peak power consumption is 4W.
- The deployable antenna is the NanoCom ANT430 (GOMSpace, 2017) and is a quasi-omnidirectional canted turnstile antenna. A high power consumption of 10W is associated to this component.
- The ADCS is the FleXcore (Blue Canyon Technologies, 2017) which is a fully integrated ADCS composed of micro reaction-wheels, two star trackers, and a micro-controller. Its maximum power consumption peaks to approximately 4W. Regarding the pointing accuracy of the FleXcore, it is able to achieve ±21.6 arcsec ($3\sigma$) for three axes, with a fine attitude determination of the order of 1 arcsec. The accuracy of ±21.6 arcsec is worse than the instrument resolution leading to some uncertainty on the actual positioning of the target on the focal plane. However, the fine determination of the

pointing of the order of the arcsec (Hegel, 2016) will reduce the uncertainty, allowing derivation of the target photometry. Moreover, achieving the best accuracy on the photometry will probably require implementation of a chopping mode similar to that used for the BRITE satellites. Indeed, chopping coupled with an appropriate data processing significantly improved the data quality and specifically the robustness against CCD radiation damage defects for the BRITE satellites (Pablo et al., 2016; Popowicz et al., 2017).

- The solar panels are deployable panels from Clyde Space (2017). Their power generation at 60°C (the temperature derived from the thermal analysis) and at beginning of life (BOL) amounts to 6.91W per panel. At end of life (EOL), a loss of a few percent in the panel efficiency is expected and the final power generation is estimated at 6.01W per panel. The EOL total power generation is then evaluated to 24.04W with a deployable four-panel configuration and 30.05W if a fifth body-mounted panel is added.
- The NanoPower P31U (GOMSpace, 2017), which can store power up to 20Whr and manage an amount of 30W coming from the solar panels, is chosen as a battery and power supply. Its power consumption for the supply management peaks to 0.2W.

Table 5 presents the power budget, summarizing all the units of the CubeSat. The maximal power consumption of each unit is considered and 20% margins are applied for uncertainties. Within those margins, a total power of 30.9W is obtained considering the specific worst case where all the units are working simultaneously at their peak power. This budget complies with the power supply system because, with the fifth solar panel added, 30.05W are generated at EOL at normal Sun incidence. On the other hand, the battery is able to store 20Whr which is sufficient for the eclipses which last 17 min at maximum. However, this consumption of 30.9W is very pessimistic, since this situation will probably not occur. This is why Table 6 considers several more realistic operational phases. It can be concluded from these cases that there is benefit from some margins with respect to the power budget during the mission, even at EOL where the solar panels are less efficient. Indeed, in the most energy-demanding case, "observation + data transfer," a little more than 80% of the available power is engaged. This flexibility on the power consumption can also be used to enhance the sky visibility by relaxing the request of a normal Sun incidence on the solar arrays, thereby allowing tolerance of incidence angles up to 30° from normal.

Table 5. Power Budget

| Component | Maximum power consumption (W) | Maximum power consumption with 20% margin (W) |
|---|---|---|
| Detector assembly | 2.00 | 2.40 |
| On-board computer | 0.55 | 0.66 |
| Communication system | 4.00 | 4.80 |
| Deployable antenna | 10.00 | 12.00 |
| ADCS | 4.00 | 4.80 |
| Solar panels (mechanism) | 5.00 | 6.00 |
| Battery | 0.20 | 0.24 |
| TOTAL | 25.75 | 30.90 |

## 5. Photometric Budget

### 5.1. Modeling

The aim of the photometric budget is to quantify the amount of photons reaching our detector for any given target star. It will inform about the observing time needed to achieve the requirements (especially the signal to noise ratio (SNR)). Stars are differentiated according to their magnitude V and their effective temperature $T_{eff}$. Appendix A provides the detailed calculation of the photon flux $dN$ emitted by a star for a small range of wavelength $d\lambda$, the final result being:

$$dN = \frac{8.402 * 10^{34} 10^{-0.4(V-A_V+BC+A_\lambda)} d\lambda}{T_{eff}^4 \lambda^4 \left(\exp\left(\frac{1.439\ 10^8}{\lambda T_{eff}}\right) - 1\right)}. \quad (1)$$

All the parameters of $dN$ are known for stars of the main sequence except for the color excess $E_{B-V}$ that are encountered in the expression of the interstellar extinction $A_V$ and $A_\lambda$. The latter is specific to each source, and

Table 6. Expected Operational Phases During the Mission

| Phase | Detector assembly | OBC | Communication system | Antenna | ADCS | Solar panels mechanism | Battery | Total power (20% margin) |
|---|---|---|---|---|---|---|---|---|
| Deployment | NO | YES | NO | NO | YES | YES | YES | 11.7W |
| Observation | YES | YES | NO | NO | YES | NO | YES | 8.1W |
| Data transfer | NO | YES | YES | YES | YES | NO | YES | 22.5W |
| Observation + data transfer | YES | YES | YES | YES | YES | NO | YES | 24.9W |

depends on the environment between the star and the observer. Since it is intended to establish a general photometric budget that is a function of V and $T_{eff}$, the study considered some extreme values for the stars of interest.

The primary interest focuses on massive stars of spectral type OB down to fifth magnitude. Such stars are the brightest in the UV domain and their influence on their direct neighborhood and on the galactic scale is very important making them very interesting targets to observe (Puls et al., 2008). It was thus expected that most of the targets would be nearby objects with a relatively modest interstellar reddening. Using the Yale Bright Star Catalog, the distribution of $A_V$ was investigated as a function of spectral type and magnitude for over 250 stars, including all bright O-type stars and B-type stars down to spectral type B5. It was found that $A_V$ falls in the range between 0 and 2.5 for all the stars in this sample, with a mean at 0.3. Therefore, it was possible to define two extreme cases for the photometric budget: the first one being the worst case, corresponding to the highest extinction for which $A_V = 2.5$ was adopted, and the second being more realistic, where the absorption is at the sample mean of $A_V = 0.3$. Fixing the value of $A_V$ then sets the values of $E_{B-V}$ and also $A_\lambda$ (see Appendix A). Knowing all the parameters of the photon flux, it was calculated by integrating $dN$ over the spectral domain – i.e., between 2500 and 3500 Å: $N = \int_{\lambda_1=2500\text{ Å}}^{\lambda_2=3500\text{ Å}} dN$. Figure 8 presents the curves of $N$ for several magnitudes V and as a function of $T_{eff}$.

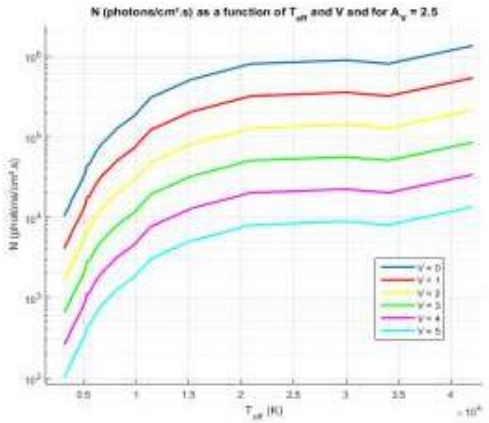


Figure 8. N (expressed in photons/cm².s) as a function of $T_{eff}$ (in K) and V in the highest absorption case ($A_V = 2.5$).

## 5.2. Signal to Noise Ratio

The required photometric accuracy (Table 1) can be translated into an SNR. It is necessary to reach an accuracy of 0.001 mag, which corresponds to a SNR of 1086. As a first step, the signal is computed as $S = N * T_{exp} * A_{eff} * \eta$ where $T_{exp}$ is the exposure time, $A_{eff}$ is the effective area of the telescope and $\eta$ is the overall efficiency of the instrument. The $\eta$ parameter accounts for the reflectivity of the mirrors (between 82% and 92% with an average of 87%) (Melles Griot, 2016), the transmission of the UV filter (50%, per Schott, 2016), and the quantum efficiency of the detector, which is assumed constant over the spectral domain. Considering 10% margins and the lowest efficiencies for all the elements of the telescope, the study found a minimal efficiency of $\eta_{min} = 12\%$, which is used in this Section. Concerning the noise, the photon noise, the dark signal of the detector, the readout noise, and the sky background presented in the stray light section were considered. The expression of the SNR is therefore:

$$SNR = \frac{S}{\sigma_{CCD}} = \frac{N\,A_{eff}\,t_{exp}\,\eta}{\sqrt{N\,A_{eff}\,t_{exp}\,\eta + nDt_{exp} + nR^2 + 0.007 * N_{SL} A_{eff}\,t_{exp}\,\eta}}. \quad (2)$$

In this equation, D is the dark signal, R is the RMS value of the readout noise and $n$ represents the number of pixels illuminated by the PSF (i.e., $n = 4$). The worst case for the SNR computation corresponds to one of

the cooler stars with V = 5 and suffering from the highest extinction, i.e., $A_V$ = 2.5. Figure 9 presents the results of this worst case on the left: to fulfill the requirement for V = 3, the integration time must be approximately equal to 70 seconds. For the other magnitudes V = 4 and 5, it is not possible to achieve the required SNR in the specified integration time of 5 min because of the noise contributed by the stray light. These results are showing the limits of such a small telescope for the observation of the faintest stars among our possible targets. Nevertheless, the right side of Figure 9 corresponds to the same results but for a mean extinction, and in this more realistic case, the requirements of Table 1 are met: an SNR of 1086 is achieved in 105 seconds for a fifth magnitude B5 star, showing that the scientific requirements, and even the goals of Table 1, will be honored for the vast majority of the targets.

Some other effects can affect the SNR of the instrument, such as the aging of the CCD sensor, which is vulnerable to radiation-induced performance changes. The changes are categorized into two types (Burt et al., 2009): changes due to the ionizing dose of energetic charged particles and displacement damage arising from heavy particles (protons and neutrons). The main drawbacks due to these radiations are an increase of the dark signal and a decrease of the charge transfer efficiency. These effects need to be evaluated during pre-flight tests by performing accelerated aging experiment and by calibrating the sensor in-flight. Furthermore, their effect can be mitigated by implementing a chopping mode similar to what is done for the BRITE satellites (Pablo et al., 2016; Popowicz et al., 2017). Another effect is the jitter noise introduced by the reaction wheels of the ADCS. The wheels imbalance induces micro-vibrations that could disturb the spacecraft and make it lose its pointing position, hence moving the target in the focal plane. Knowing the wheels imbalance of the FleXcore allowed computation of the amplitude of the jitter peak, assuming that the satellite is a rigid body, which is equal to 1.15 arcsec. The dynamical behavior of the satellite should be taken into account to refine the jitter peak determination. However, the study considered large safety margins in the assessment of jitter noise, and it can be concluded with confidence that the 1.15 arcsec peak is a realistic value that moves the image of the target within the illuminated pixels, hence not disturbing the signal to noise ratio in a significant way.

### 5.3. Saturation Issues

The photometric budget has shown benefit from a high quantity of photons at the entrance of the telescope in many cases. Therefore, even for the worst case presented in the previous section, it will not be necessary, and actually not possible, to integrate over five minutes on the same star, because of the limit of the full well capacity $C$ of the detector. The saturation limit can be expressed as:

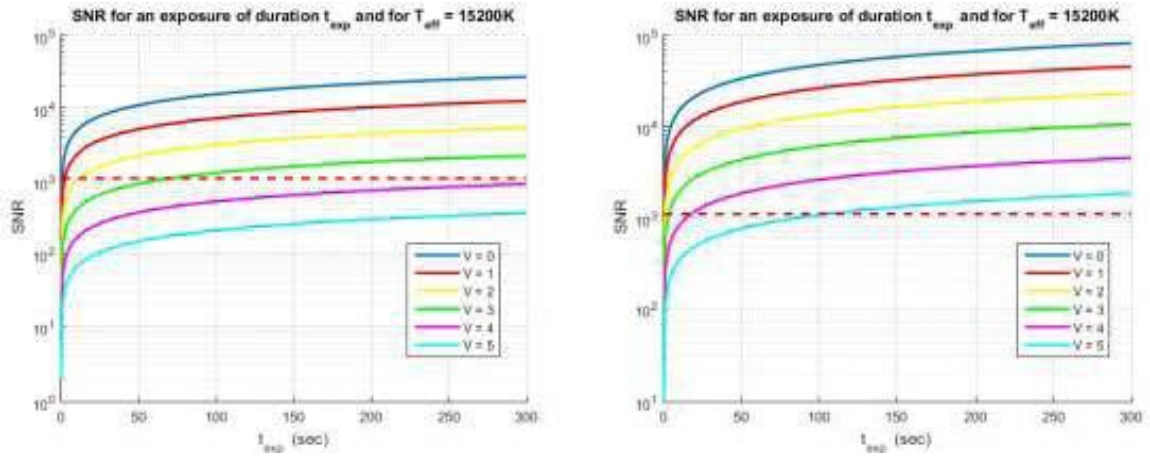


Figure 9. SNR for a star with $A_V$ = 2.5 (left) and $A_V$ = 0.3 (right), $T_{eff}$ = 15 200K and a single exposure of duration $t_{exp}$. The horizontal red dashed line corresponds to the requirement.

$$\frac{N\,A_{eff}\,\eta\,t_{exp}}{n} + D\,t_{exp} + R^2 + \frac{0.007 * N_{SL}\,A_{eff}\,\eta\,t_{exp}}{n} \leq C. \qquad (3)$$

It was assumed that all the energy of the PSF is uniformly spread over the pixels illuminated by the star. This assumption is checked when looking at the spots of Figure 2 for low off-axis angles.

Two extreme cases were considered to demonstrate the feasibility of the observations with our designed telescope. The first case is the worst in terms of saturation where the photon flux is the highest. Consider a putative hot star with an effective temperature of 42 000K, a magnitude V = 0 and $A_V$ = 0. Such an object does not exist in reality, but it allows us to probe the limitations of the instrument. Moreover, consider a situation where the efficiencies of all the optical elements are maximum yielding: $\eta_{max}$ = 21%. Figure 10 (left) presents the number of generated $e^-$ on a pixel illuminated by the hypothetic hot star as a function of the exposure time. The saturation occurs very quickly (< 0.012s). For this observation case, a more complex strategy must be considered, consisting of several very short exposures that will be combined at the end to recreate the signal. Two exposures of 0.01s are sufficient to reach and even exceed the SNR requirement.

The second case is the worst one for the SNR calculations that was presented in the previous text (i.e., $T_{eff}$ = 15 200 K, V = 3, $A_V$ = 2.5, $\eta = \eta_{min}$). Figure 10 (right) presents the results for this case: saturation now occurs for integration times around 0.18 seconds. It has been shown in Figure 9 (left) that an exposure time of approximately 70 seconds is required to achieve the required SNR. Therefore, it is necessary to combine a number of exposures, to have some margins on the full well capacity. In this case, 472 exposures of 0.1s duration are needed to reach the requirement. Note that to limit the volume of data in the on-board memory, the images related to the same observation have to be processed by the OBC using dedicated software. These numerous observations are still compliant with the maximum observation time of 5 min per target. Imagining that the readout of each exposure also takes 0.1s, the total observation time would be 94.4s, still within the allowed limits. However, the readout of the images will be done much faster considering the possible readout frequency of the detector up to 5 MHz (Table 3).

## 6. Conclusion

This paper demonstrates that the proposed UV photometer fulfills the scientific requirements. The design is optimized and accommodated to the 3U structure to obtain a fully functional model. The optical layout of the photometer is analyzed regarding optical parameters. The optimization is driven by the volume

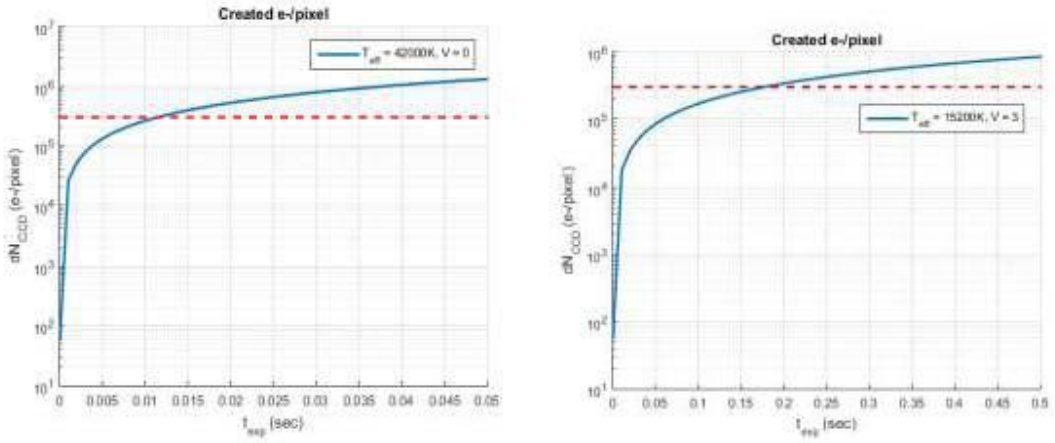


Figure 10. Number of generated on a pixel illuminated by a very hot star considering a low interstellar extinction (left) and a cooler star considering a high interstellar extinction (right). The horizontal red dashed line corresponds to the full well capacity of the detector.

limitations that the CubeSat platform imposes. Moreover, to increase the performance of the imager, a baffling system has been designed and a stray light analysis was performed to quantify the effect of the system.

The system integration led to the 3D model of the spacecraft configuration with its solar panels and subunits. The characteristics of an UV optimized and suitable detector are presented, as well as a discussion on the data storage and transfer relative to the observations made with it. It emerges from this discussion that transfer rates are very constraining, implying that a detector windowing strategy will have to be implemented.

A brief mission analysis was conducted, composed of an orbit definition and a preliminary thermal analysis based on the environment that derives from the orbit. This led to a power budget, associated to the performances of the solar panels for power generation, which proves that the power consumption is not a critical point for the mission considering current COTS.

The photometric budget allowed verification that the optimized design is able to observe the stars of interest, most of the time. Due to noise, mostly induced by the stray light component, it is not possible to observe the fainter stars in the most pessimistic observation configuration. However, it was demonstrated that in more realistic situations, the requirements for all the selected targets are met. A perspective for achieving a better photometric budget would be to design a deployable baffle in front of the current telescope aperture to block the light coming from high off-axis angles. However, such an improvement has significant technical and budgetary impacts.

## Acknowledgments

This research was funded through an ARC grant for Concerted Research Actions, financed by the French Community of Belgium (Wallonia-Brussels Federation). The authors also thank Nicolas Berckmans, who assisted with the thermal model and the related analyses in ESATAN in the framework of his master's thesis, entitled Preliminary Thermal Design of a CubeSat, at the University of Liège.

## Appendix A: Photometric Budget

For any given star, the absolute magnitude in the V band is given by $M_V = V - DM - A_V$, where $V$ is the apparent magnitude, $DM = 5 \log d - 5$ is the distance modulus (d being expressed in parsecs), and $A_V$ is the interstellar absorption in the V band. The bolometric magnitude is then given by $M_{bol} = M_V + BC$ where $BC$ is the bolometric correction in the V band. The bolometric luminosity (in erg/s) is given by:

$$L_{bol} = 3.03 * 10^{35} * 10^{-0.4 M_{bol}} = 3.03 * 10^{33} * d^2 * 10^{-0.4(V - A_V + BC)} \quad \text{(A1)}$$

It was assumed that the spectrum of the star can be represented by a black-body, whose emission follows the

$$B_\lambda(T_{eff}) = \frac{2\,h\,c^2}{\lambda^5} \frac{1}{\exp(\frac{hc}{\lambda k T_{eff}}) - 1}. \quad \text{(A2)}$$

The power emitted over a narrow range of wavelengths $d\lambda$ hence becomes $d\epsilon = B_\lambda d\lambda$. The integral of this quantity over the full electromagnetic spectrum is $\frac{\sigma T_{eff}^4}{\pi}$. Applying this to a star of bolometric luminosity $L_{bol}$, one finds: $dF = \frac{L_{bol}\, B_\lambda\, d\lambda\, \pi}{4\,\pi\, d^2\, \sigma\, T_{eff}^4}$. This formula yields the flux of the star over the narrow wavelength interval as one would see it from a distance $d$ with zero interstellar absorption. The corresponding photon flux is $dN = \frac{dF\,\lambda}{hc}$. Therefore:

$$dN = \frac{2\,c\,L_{bol}\,d\lambda}{4\,d^2 \sigma\, T_{eff}^4\, \lambda^4} \frac{1}{\exp\left(\frac{h\,c}{\lambda\, k\, T_{eff}}\right) - 1}. \quad \text{(A3)}$$

Expressing $\lambda$ and $d\lambda$ in Å and the photon flux $dN$ in photons cm$^{-2}$ s$^{-1}$, one obtains:

$$dN = \frac{8.402 * 10^{34}\, 10^{-0.4(V - A_V + BC)} d\lambda}{T_{eff}^4 \lambda^4 \left(\exp\left(\frac{1.439\, 10^8}{\lambda T_{eff}}\right) - 1\right)}. \quad \text{(A4)}$$

This number further needs to be corrected for the interstellar absorption at the relevant wavelength:

$$dN = \frac{8.402 * 10^{34}\, 10^{-0.4(V-A_V+A_\lambda)} d\lambda}{T_{eff}^4 \lambda^4 \left(\exp\left(\frac{1.439\ 10^8}{\lambda T_{eff}}\right) - 1\right)}. \qquad \text{(A5)}$$

The interstellar extinction in the UV can be approximated as a function of wave-number $\sigma = 10000/\lambda$ by (Teays, 2002):

$$\begin{cases} \dfrac{A_\lambda}{E_{B-V}} = 1.56 = 1.048\,\sigma + \dfrac{1.01}{((\sigma - 4.60)^2 + 0.280} \\ \qquad for\ 2.70 \le \sigma \le 3.65 \\ \dfrac{A_\lambda}{E_{B-V}} = 2.29 = 1.848\,\sigma + \\ \dfrac{1.01}{((\sigma - 4.60)^2 + 0.280}\ for\ 3.65 \le \sigma \le 7.14\,. \quad (A6) \\ \dfrac{A_\lambda}{E_{B-V}} = 16.17 = 3.20\,\sigma + 0.2975\,\sigma^2 \\ \qquad for\ 7.14 \le \sigma \le 10, \end{cases}$$

where $E_{B-V} = (B-V) - (B-V)_0$ is the color excess expressed as a function of the observed and the intrinsic color index with $A_V \cong 3.1 E_{B-V}$.

## References


Aerts, C., Christensen-Dalsgaard, J., and Kurtz, D. W. (2010): *Asteroseismology*, Springer Science + Business Media.

Blomme, R. et al. (2012): CoRoT Observations of O Stars : Diverse Origins of Variability. *Astronomical J. of the Pacific*, Vol. 465, pp. 13–18.

Blue Canyon Technologies. FleXcore. Available at: http://bluecanyontech.com/flexcore/ (accessed October 24, 2017).

Bogges, A. et al. (1978): The IUE Spacecraft and Instrumentation. *Nature*, Vol. 275, pp. 372–377.

Burt, D. et al. (2009): Improving Radiation Tolerance in e2v CCD Sensors, in *Proc. SPIE* 7439, Astronomical and Space Optical Systems, 743902.

Clyde Space. 3U Double-Deployed Solar Array. Available at: https://www.clyde.space/products/26-3u-doubledeployed-solar-array (accessed March 9, 2017).

Conard, S. J. et al. (2000): Far Ultraviolet Spectroscopic Explorer Optical System: Lessons Learned, in *Proc. SPIE* 4139, Instrumentation for UV/EUV Astronomy and Solar Missions, 10.1117/12.410522.

Davenport, J. R. A. (2016): The Kepler Catalog of Stellar Flares. *The Astrophysical J.*, Vol. 829, pp. 23–34.

e2v Technologies. CCD47-20 NIMO Back Illuminated. Available at: https://www.e2v.com/resources/account/download-datasheet/3713 (accessed October 3, 2017).

Fischer, R., Tadic-Galeb, B., and Yoder, P. (2008): *Optical System Design*, 2nd ed. McGraw-Hill.

Gómez de Castro, A. I. et al. (2014): Building Galaxies, Stars, Planets and the Ingredients for Life Between the Stars: The Science Behind the European Ultraviolet-Visible Observatory. *Astrophysics and Space Sci.*, Vol. 354, pp. 229–246.

GOMSpace. Products. Available at: http://www.gomspace.com/index.php?p=products (accessed January 2, 2017).

Gondhalekar, P., Phillips, A., and Wilson, R. (1980): Observations of the Interstellar Ultraviolet Radiation Field from the S2/68 Sky-survey Telescope. *Astronomy and Astrophysics*, Vol. 85, No. 3, pp. 272–280.

Handler, G. (2013): Asteroseismology, in *Planets, Stars and Stellar Systems Volume 4: Stellar Structure and Evolution*, T. Oswalt and M. Barstow (eds.), pp. 207–241.

Harvey, J. and Shack, R. (1975): Light-scattering Characteristics of Optical Surfaces, Optical Sciences Center, University of Arizona, Tucson, Arizona.

Hegel, D. (2016): FlexCore: Low-Cost Attitude Determination and Control Enabling High-Performance Small Spacecraft, in *Proc. of the AIAA/USU Conf. on Small Satellites*, Technical Sessions X: Advanced Technologies II, SSC16-X-7.

ISIS Space. Products. Available at: https://www.isispace.nl/products/ (accessed March 9, 2017).

Leinert, Ch. et al. (1998): The 1997 Reference of Diffuse Night Sky Brightness. *Astronomy and Astrophysics Supp.*, Vol. 127, pp. 1–99.

Mason, K. O. et al. (2001): The XMM-Newton Optical/UV Monitor Telescope. *Astronomy and Astrophysics*, Vol. 365, pp. L36–L44.

Melles Griot. Optical Coatings. Available at: http://mellesgriot.com/ (accessed December 30, 2016).

NSF-NASA (2013): CubeSat-Based Science Missions for Geospace and Atmospheric Research. *National Science Foundation (NSF) Ann. Rep.*

Pablo, H. et al. (2016): The BRITE Constellation Nanosatellite Mission: Testing, Commissioning and Operations. *Pub. of the Astronomical Soc. of the Pacific*, Vol. 128, pp. 125,001.

Persky, M. (1999): Review of Black Surfaces for Space-borne Infrared Systems. *Rev. of Scientific Instruments*, Vol. 70, Issue 5.

Popowicz, A. et al. (2017): BRITE Constellation: Data Processing and Photometry. *Astronomy and Astrophysics*, Vol. 605, id. A26.

Puls, J., Vink, J. S., and Najarro, F. (2008): Mass Loss from Hot Massive Stars. *The Astronomy and Astrophysics Rev.*, Vol. 16, pp. 209–325.

Roach, F. (1964): The Light of the Night Sky: Astronomical, Interplanetary and Geophysical. *Space Science Revs.*, Vol. 3, Issue 4, pp. 512–540.

Schott. Schott UG11 transmission data. Available at: http://www.uqgoptics.com/materials_filters_schott_uvTransmitting_UG11.aspx (accessed December 30, 2016).

Smith, M. et al. (2010): ExoplanetSat: Detecting Transiting Exoplanets Using a Low-cost CubeSat Platform, in *Proc. SPIE* 7731, Space Telescopes and Instrumentation 2010: Optical, Infrared, and Millimeter Wave, 773127-14.

Swartwout, M. (2013): The First One Hundred CubeSats: A Statistical Look. *J. of Small Satellites*, Vol. 2, No. 2, pp. 213–233.

Teledyne e2v. CCD Image Sensors for Space and Ground-based Astronomy. Available at: https://www.e2v.com/products/imaging/ccd-image-sensors-for-space-and-ground-based-astronomy/ (accessed March 9, 2017).

Teays, T. (2000): Ultraviolet Astronomy, in *Allen's Astrophysical Quantities*, A. Cox (ed.), pp. 169–182.

Terebizh, V. (2001): Optimal Baffle Design in a Cassegrain Telescope. *Experimental Astronomy*, Vol. 11, Issue 1, pp. 171–191.

Weiss, W. et al. (2014): BRITE-Constellation: Nanosatellites for Precision Photometry of Bright Stars. *Astronomical Soc. of the Pacific*, Vol. 126, pp. 573–585.

Woellert, K. et al. (2011): CubeSats: Cost-effective Science and Technology Platforms for Emerging and Developing Nations. *Advances in Space Research*, Vol. 47, pp. 663–684.

 